Technische Universität München
Physik Department
Lehrstuhl für Biomedizinische Physik, Prof. Franz Pfeiffer

Image Processing for X-ray and Neutron Radiographies and Tomographies

Jonathan Schock

Vollständiger Abdruck der von der Fakultät für Physik der Technischen Universität München zur Erlangung des akademischen Grades eines

Doktors der Naturwissenschaften (Dr. rer. nat.)

genehmigten Dissertation.

Vorsitzender:	Prof. Dr. Ulrich Gerland
Prüfer der Dissertation:	1. Prof. Dr. Franz Pfeiffer
	2. Prof. Dr. Peter Böni

Die Dissertation wurde am 17.6.2019 bei der Technischen Universität München eingereicht und durch die Fakultät für Physik am 5.11.2019 angenommen.

Abstract

Since several years, non-destructive testing of different samples and materials has become a de-facto standard in many fields of research from medicine and mechanical engineering to cultural heritage and physics. A multitude of samples and materials with sizes in different magnitudes in this fields requires different probing techniques, amongst them being X-ray and neutron absorption based imaging methods. As the state-of-the-art evolves over time, more and more measuring procedures are developed and therefore the field of applications gets wider. At the same time these new applications and new samples offer challenges regarding their processing, especially in regard to imaging speed and image quality. This work presents the theoretical background of neutron and X-ray imaging as well as basic concepts of optics and image processing. An additional chapter is dedicated to the implementation of image processing techniques in massive parallel programming environments. In the second part of this work, three current applications are examined in more detail. The first chapter examines the applicability of super resolution to neutron and X-ray imaging. The second chapter describes several algorithms and results gained in the context of neutron radiographies. The third chapter describes the construction of a dual-energy computed tomography setup with a single source and a layered scintillator to acquire dual-energy data in a single shot. First results of this setup are also presented.

Zusammenfassung

Seit einigen Jahren sind nicht-destruktive Testverfahren von verschiedenen Proben und Materialien der Stand der Technik in vielen Forschungsfeldern von Medizin und Maschinenbau bis hin zur Erforschung von Kulturerbe und Grundlagenforschung in der Physik. Die verschiedenen Proben und Materialien mit Strukturen in verschiedenen Längenskalen erfordern verschiedene Messmethoden, darunter absorptionsbasierte Bildgebung mit Neutronen- und Röntgenstrahlen. Da sich der Stand der Technik fortlaufend weiterentwickelt, eröffnen sich neue Anwendungsfelder und neue Messtechniken werden entwickelt. Gleichzeitig stellen diese Messtechniken und Proben neue Herausforderungen an die Bildverarbeitung, vor allem im Hinblick auf Verarbeitungsgeschwindigkeit und Bildqualität. Diese Arbeit präsentiert den theoretischen Hintergrund von Neutronen- und Röntgenbildgebung sowie grundlegende Konzepte der Optik und Bildverarbeitung. Ein zusätzliches Kapitel widmet sich der Implementierung von Bildverarbeitungsmethoden in massiv parallelen Programmierumgebungen. Im zweiten Teil der Arbeit werden drei aktuelle Anwendungsbeispiele näher betrachtet. Das erste Kapitel behandelt die Anwendbarkeit von superresolution Methoden in der Neutronen- und Röntgenbildgebung. Das zweite Kapitel beschreibt verschiedene Algorithmen und Ergebnisse aus dem Bereich der Neutronenradiographien. Im dritten Kapitel wird der Aufbau eines Dual-Energy Tomographiegeräts mit einer einzelnen Quelle und einem geschichteten Szintillator beschrieben, mit welchem Dual-Energy Aufnahmen innerhalb einer Belichtung gemacht werden können. Erste Ergebnisse dieses Aufbaus werden dort vorgestellt.

Contents

Part I

Imaging Theory

Chapter 1

X-ray Imaging

This chapter will give an introduction to the theory behind X-ray imaging, starting with a short overview over X-ray production and X-ray sources, continuing with X-ray absorption and detection and closing with an introduction to scintillation.

1.1 Introduction

X-rays are electromagnetic waves with energies E between 5 keV and several hundreds of keV. According to the formulas

$$\begin{aligned} E &= h \cdot f \\ f &= \frac{c_0}{\lambda} \\ \lambda &= \frac{h \cdot c_0}{E}, \end{aligned} \tag{1.1}$$

where f is the frequency and λ the wavelength of the wave, c_0 the speed of light in vacuum and h Planck's constant, this energies are linked to wavelengths of about 250 – 5 pm in vacuum. Besides that, the wavelength interval of X-rays is not clearly defined and overlaps with that of ultraviolet radiation on the low energy side, and γ-radiation on the high energy side [Buzug, 2008, p. 16]. X-rays were discovered in 1895 by Wilhelm Conrad Röntgen, and named after his original description. X-rays are usually called soft X-rays when the wavelength λ is larger than the inter-atomic distance in solid matter ($\approx 0.1 - 0.5$ nm) and hard X-rays below that limit. Comparable to visible light, X-rays have an index of refraction, which is a complex number, with the real part describing dispersion and the imaginary part describing attenuation. The complex index of refraction of X-ray radiation is usually written as

$$n^* = n - i\beta, \tag{1.2}$$

which is often written as

$$n^* = 1 - \delta - i\beta, \tag{1.3}$$

because the refractive index of X-ray radiation is extremely close to 1 and therefore δ is very small and positive.

1.2 X-ray production

Apart from a negligible amount of natural X-ray radiation through conversion of high energy particles in the atmosphere and the cosmic X-ray background, most used X-rays are produced in man-made X-ray sources. Mainly, two different processes exist to produce X-ray radiation. The first process is the acceleration of charged particles. This is mostly done by deceleration or deflection of electrons, in more rare cases, light ions or protons can be used. As the kinetic energy of one electron can be converted to radiation in a cascading manner over several subprocesses, this process results in a continuous emission spectrum, which is known as `bremsstrahlung`. In X-ray tubes, electrons from a heated filament are accelerated using a high voltage towards an anode consisting of a high-Z material, where the electrons are decelerated and emit `bremsstrahlung`. Figure 1.1 shows the dominating `bremsstrahlung` in the spectrum of a tungsten anode, with energies up to the acceleration voltage of 60 kV. As this acceleration voltage is an upper-limit to the X-ray spectrum, it is often designated as peak voltage and written as kVp. The other process that

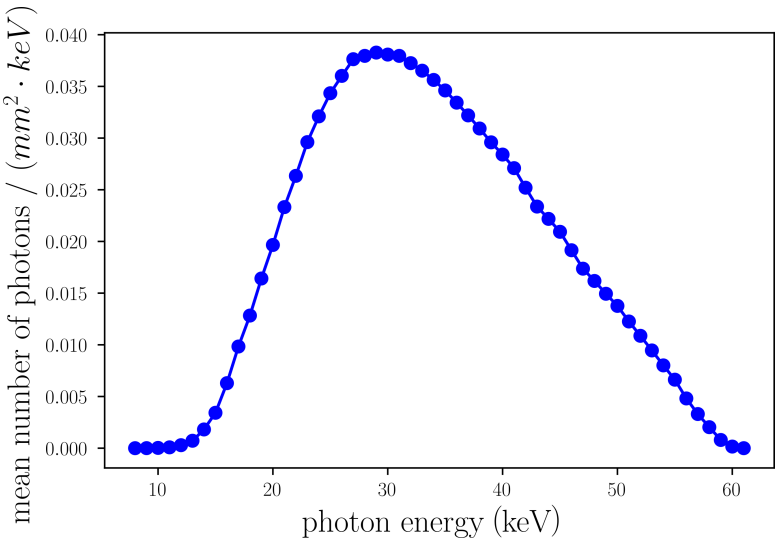

Figure 1.1: The simulated spectrum of a tungsten anode with an acceleration voltage of 60 kVp. The bremsstrahlung peak is dominating. Values calculated with x-ray toolbox [SiemensAG, 2017].

yields X-ray radiation is the transition of high-energy states in the electronic shell of atoms or molecules. If an electron from a low energy state inside an atom is removed, e.g. by ionisation, an electron from a higher energy state can fill this void and release the energy difference as fluorescent radiation. Because of the discrete nature of energy states inside atoms, the spectrum of the emitted radiation is also discrete. This leads to the so called characteristic peaks in the

X-ray spectrum. This peaks are labelled according to the energy state, where the electron ends up on plus a Greek subscript indicating the difference to the originating energy state. Figure 1.2 illustrates one possible process for the K_α line in carbon leading to a peak at 0.277 keV [Bearden, 1967]. In a standard X-

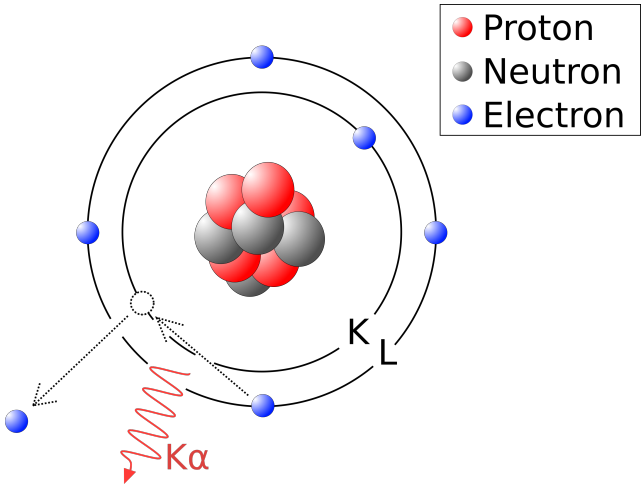

Figure 1.2: One possible process for K_α emission in a carbon atom. A K-shell electron is removed from the atom by ionization. An electron from the L-shell fills the vacancy and radiates the excess energy.

ray tube, both those processes occur and the resulting spectrum includes both `bremsstrahlung` and the characteristic peaks, as can be seen in Figure 1.3. Apart from the position of the characteristic peaks, which are dependant on the anode material, tuning the acceleration voltage between anode and cathode allows tuning the spectrum, whereas increasing the heating current inside the filament leads to a higher intensity of radiation as more electrons are emitted. Not all of the energy of the accelerated electrons is radiated as X-ray radiation. About 99 % of the kinetic energy gets lost in the form of dissipated heat inside the anode, which effectively is an upper limit to the tube's intensity.

1.3 X-ray sources

The first X-ray source of Röntgen himself was nothing more than a very simple discharge tube, an assembly of two electrodes in a closed glass container, that could be evacuated or filled with gas. Originally this setup was used to investigate the so called cathode rays, a dim light between the electrodes, when an external voltage was applied. The coolidge tube, presented by William Coolidge in 1913, introduced the concept of a heated filament for thermionic emission of electrons and allowed the cooling of the anode with circulating water. The concept is still in use today, but has been refined in several ways. X-ray tubes with rotating anode as well as sources using a stream of liquid metal as anode (liquid metal jet sources) have been developed aside magnetic optics to focus the electron beam on a small spot on the target to get a smaller source spot. The discovery of synchrotron radiation opened the way to a whole

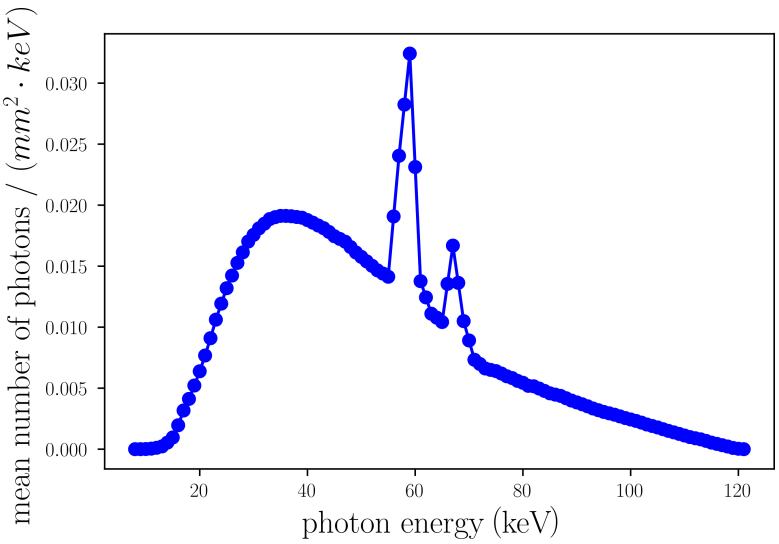

Figure 1.3: The simulated spectrum of a tungsten anode with an acceleration voltage of 160 kVp. The characteristic peaks of tungsten can be seen over the bremsstrahlung spectrum. Values calculated with X-ray toolbox [SiemensAG, 2017].

new generation of X-ray sources. When a charged particle is accelerated in an electric or magnetic field, it emits radiation[1]. This process has been first observed in synchrotron accelerators [Elder et al., 1947]. Since then, the usage of synchrotrons as X-ray sources has been optimized with custom built facilities, including undulators that accelerate electrons on a sinusoidal track. This development culminated in the development of `Free Electron Laser (FEL)`, where the speed of the electrons is matched to the period length of the undulators, which leads to high flux and coherence via constructive interference and the process of self-amplified stimulated emission (SASE).

1.3.1 Characterisation of X-ray sources

As there are a lot of different X-ray sources, it is necessary to find some general describing characteristics to compare them.

Flux

The flux of an X-ray source is a measure for its intensity measured in photons per unit of time. A higher intensity means shorter exposure time in imaging applications or higher statistics in general. An approximate measure of the

[1] The exact cases in which accelerated particles emit radiation are subject to discussion [Dittus and Lämmerzahl, 2007][Rohrlich, 2001][Soker and Harpaz, 2004].

expected flux can be given by multiplying the input energy with the tube's efficiency, that is approximately

$$\text{Efficiency} \approx U \cdot Z \cdot 10^{-6}, \tag{1.4}$$

where U is the acceleration voltage in kV and Z is the atomic number of the anode material [Sprawls, 1996].

Source geometry

In most imaging applications it is important to know the source size and shape, as it has an influence on the achievable image resolution [Matsui and Ono, 1985]. This influence will be treated in subsection 3.3.1.

Spectrum

Depending on the production mechanism of X-rays in the source, the spectrum itself can have various characteristics. X-ray tubes produce the typical mixture between `bremsstrahlung` and characteristic lines as described above, whereas synchrotron radiation or radiation from an `FEL` can be highly monochromatic. Experiments with monochromatic radiation don't suffer from polychromatic artefacts such as chromatic aberration or beam hardening. On the other hand, the dependency of processes on the energy, can be used to extract further information when using polychromatic radiation. This case will be discussed in chapter 8.

Beam geometry

The beam geometry can be described via the shape and the opening angle of the radiation profile, emitted from the source, which is also known as collimation and given in units of milli-radian. Together with the geometrical boundary conditions of the experimental environment, this describes the basis for geometrical optics of the setup. Two common cases are parallel beam and cone beam geometry. Cone beam geometry allows for the use of geometrical magnification, whereas parallel beam allows the simplification of image acquisition due to redundancies in the ray paths (e.g. the projection of a vertically rotating sample under 0° and 180° is only vertically flipped under parallel beam geometry). If the source-sample distance is a lot larger than the sample-detector distance, the beam geometry can often be approximated to be a parallel one.

Brilliance

The characteristic quantities mentioned above are summarized in the source brilliance, which is defined as:

$$B = \frac{N}{t \cdot \Omega \cdot A \cdot \frac{\Delta\lambda}{\lambda}}. \tag{1.5}$$

In this equation N is the number of photons, t the time in seconds, Ω the beam divergence in milli-rad-squared, A the source area in milli-meters-squared and $\frac{\Delta\lambda}{\lambda}$ stands for the spectral bandwith, which is usually defined as the peak-width

at the Full Width at Half Maximum (FWHM) over the wavelength of the maximum. It is a convention to take a fixed relative energy bandwidth (BW) of 0.1% for $\frac{\Delta\lambda}{\lambda}$ [Als-Nielsen and McMorrow, 2011].

1.4 Interaction with matter

The interaction of photons in this section are both important for understanding the attenuation of X-rays inside matter and their conversion and detection after the sample. At first, the different interaction mechanisms are described, after that, the concept of the absorption coefficient is introduced which is needed to describe both radiographic as well as tomographic imaging.

1.4.1 Interaction processes

Coherent scattering

Coherent, or elastic scattering, is the group of scattering processes in which the incident photon changes its direction, but its energy and therefore wavelength is conserved. The two types of coherent scattering of X-rays with matter are Rayleigh- and Thompson scattering, that can both be classically described as wave-particle interaction. An incident wave excites an atom and is therefore absorbed. The atom relaxes immediately into its undisturbed state via emission of radiation. There is no net amount of energy transfer to the atom which makes this process unsuitable for particle detection; in diagnostic radiology its effect is mostly neglected or seen as a source of image noise [Curry et al., 1990, p.61 f.] [Gilmore, 1992, p. 14]. Following the formulation of [Thompson et al., 2009], Thomson scattering can be described for a single electron with a total cross section of

$$\sigma_{\mathrm{T}} = 8\pi r_{\mathrm{e}}^2/3, \tag{1.6}$$

where r_{e} is the classical radius of the electron. In atoms, the total cross section becomes an integral of all electrons, that can be formulated to be

$$\sigma_{\mathrm{R}} = \pi r_{\mathrm{e}}^2 \int_{-1}^{1} |f(\theta)|^2 (1 + \cos^2\theta) d(\cos\theta). \tag{1.7}$$

In this formulation, $f(\theta)$ is the complex atomic scattering factor as described in [Hubbell et al., 2000, p. 473].

Incoherent scattering

In contrast to coherent scattering, in incoherent or inelastic scattering the energy and wavelength of the incident particle is not conserved. One example is Compton scattering, where an incident photon interacts with an outer shell electron of an atom. The photon transfers some of its energy to the electron, which is removed from the atom, and therefore both particles change their energy. The energy of the photon after scattering depends strongly on the scattering angle. This energy loss of the incident photon can be described as

the change in energy of the outer shell electron which follows to be

$$E_\mathrm{e} = E_\gamma \left(1 - \frac{1}{\left[1 + E_\gamma \frac{1-\cos(\theta)}{m_0 c^2} \right]} \right), \tag{1.8}$$

with m_0 being the rest-mass of the electron [Gilmore, 2008]. Strictly, this equation only holds true for scattering with a free electron and for bound electrons, the binding energy has to be taken into account. Especially for small scattering angles and low energies, the Compton cross section gets small and coherent scattering gets more dominant [Thompson et al., 2009].

The probability for Compton scattering is dependant on the electron density inside the material, which is on the one hand dependant on the atomic number (low atomic numbers have higher electron densities in general) and on the other hand dependant on the density of the material itself. The energy dependence follows the Klein-Nishina equation, shown in subsection A.3.1, stating that for higher energies, the probability is slightly decreasing. For the simpler case of unaligned electrons and unpolarized incident X-rays, the approximations of the Klein-Nishina equation can be used to describe the cross-section σ_KN [Thompson et al., 2009]:

$$\sigma_\mathrm{KN} \approx 8\pi r_\mathrm{e}^2 \frac{(1 + 2k + 1.2k^2)}{3(1+2k)^2}, \tag{1.9}$$

with $k = \frac{E_0}{m_\mathrm{e} c^2}$ being the photon energy formulated in terms of the electron rest energy.

Photoelectric effect

If the incident energy of a photon is higher than the binding energy of an electron to its corresponding nucleus, it can transfer all its energy to the electron. In the process, the photon is absorbed and the electron is removed from the atom and becomes a free photoelectron, with a kinetic energy E_e that equals the photon energy E_γ minus the binding energy E_b of the electron inside the atom so that

$$E_\mathrm{e} = E_\gamma - E_\mathrm{b}. \tag{1.10}$$

The photoelectron leaves behind an empty state in its origin shell, that can be filled either from an electron from a higher shell of the same atom or any other free electron from the vicinity. This process is comparable to de-excitation and leads to the emission of characteristic radiation as in section 1.2. The interaction probability for the photoelectric effect is roughly proportional to the third power of the atomic number Z, which makes it suitable to detect different material compositions inside material. Furthermore it is roughly inverse proportional to the third power of the incident photon energy E_γ. This leads to an interaction cross-section τ of

$$\tau \propto \frac{Z^n}{E_\gamma^m}, \tag{1.11}$$

with n and m being between 3 and 5 as well as $m < n$ [Gilmore, 2008]. This leads to the photoelectric effect being more prominent in high-Z materials, which makes them sought after in the design and development of new detector materials.

In semiconductors, the same process is called inner photoelectric effect and leads to the separation of charges in the valence band. The resulting electron-hole pairs can be separated and the charge carriers can produce a current in the conduction band or be collected in a potential well. For this process to be able to occur, the energy of the incident photon has to be larger than the energy separation or band-gap of the semiconductor. This process is especially important for the detection of light in CCD detectors but also for energy conversion in solar cells.

High energy interactions

If the energy of an incident photon exceeds the energy of the rest mass of an electron-positron pair ($\approx 1.022\,\mathrm{MeV}$), pair production can occur. As this production itself isn't conservative of energy and momentum, some excess energy has to be carried away either by a nearby nucleus or an electron, resulting in an even higher threshold energy. Another mechanism of high energy interaction is the photonuclear absorption, in which photons with energies around 10 MeV can excite resonant nuclei states. These two interaction mechanisms are not important in the energy ranges considered in this work and are only mentioned for the sake of completeness.

1.4.2 Attenuation coefficient

For each interaction cross section, an analogous attenuation coefficient can be defined. As an example, the photoelectric attenuation coefficient μ_{PE} can be derived from the cross section as

$$\mu_{\mathrm{PE}} = \tau \cdot \rho \cdot \frac{N_{\mathrm{A}}}{A}, \tag{1.12}$$

where N_{A} is the Avogadro constant, A is the atomic number and ρ is the density of the material, the incident radiation is interacting with. If all interactions are combined, the total attenuation coefficient follows, which is a simple sum of the attenuation coefficients for each interaction process and in this work referred to simply as μ. This attenuation coefficient is a measure for the decrease of the beam intensity of an incident X-ray beam when travelling through material and is in general material- and energy-dependent. A monochromatic beam with an intensity of I_0 that travels through a sample with the thickness d gets attenuated according to the Lambert-Beer law

$$I(d) = I_0 e^{-\mu d}. \tag{1.13}$$

The coefficient μ in this equation is also referred to as the linear attenuation coefficient, and in general is an energy dependent material constant. The two main energy dependencies of the attenuation coefficient μ in the imaging energy

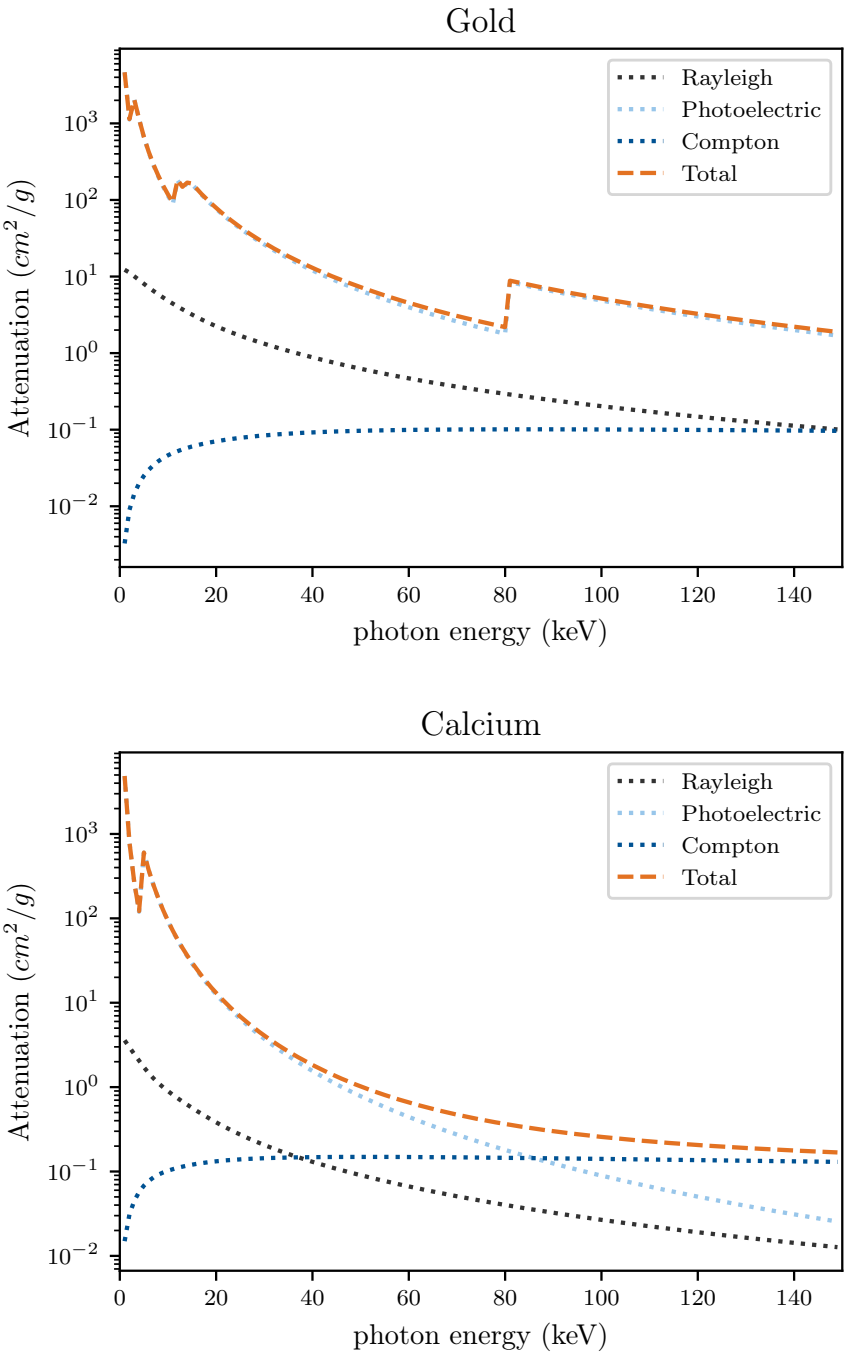

Figure 1.4: The energy dependence of the mass attenuation coefficient of gold and calcium and the constituting components. Values are calculated with xraylib [Schoonjans et al., 2011].

range in this work are the photoelectric effect with approximately

$$\mu_{\text{photo}}(E) \propto \rho \frac{Z^4}{A \cdot E^3} \tag{1.14}$$

and the Compton effect with approximately

$$\mu_{\text{Compton}} \propto \rho \frac{Z}{A} \sigma(E), \tag{1.15}$$

where ρ is the material density, Z is the atomic number, A is the atomic weight and $\sigma(E)$ is the energy dependent formulation of the Klein-Nishina equation as given in subsection A.3.1. This leads to the expanded, energy- and material dependent formulation of Equation 1.13

$$I(d, E) = \int_{E_0}^{E_{\max}} I_0(E) e^{-\int_0^{d_{\max}} \mu(E, d) dd} dE. \tag{1.16}$$

An example of the energy dependence of the mass attenuation coefficient, which is defined as the linear attenuation coefficient divided by the material's density, is given in Figure 1.4 for two different elements. If the `attenuation` of a material is measured at one constant energy, only materials in the beam path that have a notable difference in their attenuation coefficient can be distinguished. If the same sample is scanned at different energies, the energy dependence of the attenuation coefficient can be used to gain additional information. For example, it is possible to differentiate between materials, that have a similar attenuation coefficient at one energy but may differ at another energy. The reason for this can be a difference in the sudden jumps in the absorption coefficients due to different binding energies in the atoms and referred to as K-edges, which can be seen in Figure 1.4 for gold at around 80 keV. Other additional information that can be extracted from a measurement with multiple energies is the concentration of elements or the identification of elements. When two different spectra are used, one speaks about `dual-energy imaging`, a broader term comprising two or more spectra is `spectral imaging`. In this work a novel setup for `dual-energy imaging` is presented in chapter 8.

1.5 X-ray detection

There are many possibilities to detect X-rays, ranging from ionisation chambers over solid-state detectors to scintillation counters with photomultipliers. In this work, the focus lays on imaging of the attenuation of X-rays through a sample, therefore only detectors suitable for imaging will be discussed. As imaging in this context is a spatial sampling of the incident X-ray beam, this naturally leads to the use of pixelated detectors. One possible detection path is the conversion of X-rays to visible light photons via scintillation and their subsequent imaging with cameras, which is treated in chapter 4. Another detection possibility in imaging is the use of semiconductor- or solid-state-detectors, which will be explained in this section. As the understanding of the electronic band-structure is important for the working principle of scintillation, it will be explained first.

Electronic structure

As most semiconductor detectors are based on a *pn*-junction diode, the necessary concepts are introduced first. In a bulk solid, the energy states of atoms arrange in a so-called band structure, where each band is one or more energy states. Each band has a defined amount of available states, that can be occupied by charge carriers. Consequently, one speaks of a full band, when all energetic states are occupied and of an empty band if none is. The highest occupied band at 0 K is denoted as valence band, the next higher band is denoted as conduction band and if no available states exist in some energy ranges one speaks of the band gap. If the band gap is large enough, no charge carriers can cross it due to thermal excitation, no conduction can occur and the material acts as an insulator. On the other hand, if the band gap is small enough, a few electrons from the valence band can be thermally excited to the conduction band, where they can freely move. These materials are therefore called semi-conductors as this conducting behaviour is dependent on external influences such as temperature. Furthermore, the electronic structure of semiconductors can be altered, by inserting impurities into the bulk material, that have a different electronic configuration, which is referred to as doping. If the added impurities provide excess electrons, they are called donors, because this electrons can be thermalized into the conduction band very easily. As the excess charge is existent in the form of electrons one speaks of n-doping (for negative). In the reverse case, elements might provide additional empty spaces, that can be filled by electrons from the valence band. This elements are called acceptors and the resulting doping is referred to as p-doping (for positive).

pn-junction

If an n-doped material is brought into contact with a p-doped material (e.g. by doping different layers of a host crystal with different impurities), the resulting interface is called pn-junction. The diffusion of excess charge carriers between these two domains will lead to an internal electric field, that is in equilibrium with the charge drift. The region in which this happens is spatially limited and called the depletion region. If a voltage is applied to this pn-junction, this depletion region is either increased, leading to an insulating behaviour, or decreases, leading to conduction, depending on the polarity of the applied voltage. Therefore, a pn-junction acts as a diode, where the direction in which the diode acts as an insulator is referred to as reverse-bias. If an incident photon strikes the depletion region, this may lead to the creation of an electron-hole pair via the photoelectric effect. This leads to a measurable photocurrent at the electrodes of the pn-junction and therefore allows the detection of incident radiation. This process can be amplified by using a high voltage as reverse-bias and production of the photodiode in a way that facilitates impact ionization [Renker and Lorenz, 2009].

1.5.1 Scintillation

Until now, all described processes are equally true if the interacting atom is free or bound in a material. Scintillation is a special case, as it can be used to convert X-rays into (visible) photons, which are a lot easier to handle by

optical devices, such as lenses, and to detect in the end. An excited atom emits a photon when it returns to its ground state. Another possibility to get rid of that excess energy exists, when an atom may interact with other atoms in its vicinity. Examples are the excitation of vibrational modes in a complex molecule or lattice vibrations or more generally speaking phonons. Those two basically different interaction principles give rise to two different classes of scintillator material, the organic and the inorganic scintillators. This work will be restricted to inorganic scintillators, more work on organic scintillators can be found in [Gilmore, 1992, p. 36 ff.], [Blasse and Grabmaier, 1994].

Nikl describes the scintillation as a three-step process consisting of conversion, transport and luminescence. An incident particle is converted to electron-hole pairs via photoeffect and Compton scattering. The electrons are thermalized in the conduction band in which they can move. As impurities and defects in the material may lead to electronic levels inside the bandgap, charge carriers can be trapped inside this levels.[Nikl, 2006]
Depending on the nature of these levels, the transition to other states may be occurring via emission of a photon (luminescence centres), via a radiation-less process (quenching centres) or re-emission of the electron after some time (electron traps) [Gilmore, 1992, p. 41]. The emitted photons from the luminescence centres have an energy below that of the band gap, disallowing them to produce further electron-hole pairs. This shift of wavelength makes the scintillator (at least partly) transparent to its own light, which is an important characteristic. There are more describing parameters of scintillation materials from which the most important are described in the following sections. A good overview of different materials and their performance can be found in [Cherepy, 2011], a regularly updated and extensive list can be found in [Derenzo et al., 2017].

Decay time

Depending on the exact material and introduced impurities, the time scales for the different transport and luminescence processes vary wildly. Especially electrons that are trapped and re-emitted may lead to a significant after-glow of the scintillator. The decay time t_0 of a scintillator is defined such, that the fraction $1/e$ of all emitted photons are emitted during this time. A shorter decay time means faster imaging and less overlap between light stemming from different interactions inside the scintillator, which is important for time-resolved measurements.

Scintillation efficiency

Depending on the band gap of the scintillation material and the resulting impurity states, the number of emitted photons per energy of the incident photon, which is defined as the conversion efficiency, varies. Especially the quenching centres, that allow for radiation-less de-excitation lead to a loss of efficiency. As the number of photons is in many cases a function of the energy of the incident photon, it is not enough to give one single number for the efficiency. In many applications, the energy of the incident photons is to be measured via the intensity of the scintillation light. In these applications, the linearity of the

light response with respect to the incident energy and intensity is especially important.

Scintillator resolution

In general, one speaks about resolution as the ability to discriminate two or more signals based on their properties. In scintillators one important characteristic is the energy resolution, meaning that two incident particles with different energy lead to a different output. This is most often quantified as the the ratio R_{energy} with

$$R_{\text{energy}} = \frac{\text{FWHM(keV)}}{662\text{(keV)}}, \tag{1.17}$$

where the numerator is the full-width at half-maximum of the peak in the pulse-height spectrum when an incident 662 keV gamma ray from a ^{137}Cs source is measured [Bell, 2012]. In this work, the more important characteristic is the optical resolution or spatial resolution, which is the ability to discriminate between two events that arrive at different positions in the scintillator plane. As the sources of X-ray radiation in this work are mostly at an effective energy below 50 keV, the primary interaction in the scintillator is via the photoelectric effect. **Koch** et al. have done simulations of a pencil beam of X-ray radiation at the energies of 14 keV, 30 keV and 100 keV onto a disk of a YAG scintillator to simulate the dose distribution in the scintillator. The results show, that most energy of the incident beam is deposited near the center of the pencil beam resulting in a `FWHM` of less than 100 nm. This corresponds with the statement of **Hoheisel** et al. that "most common detector materials [...] operate far from fundamental spatial resolution limits" [Hoheisel et al., 2004]. Instead, the thickness of the scintillator and the imaging optics behind the scintillator have an influence on the achievable resolution comprising of the depth of focus, the diffraction and the spherical aberration [Martin and Koch, 2006]. This dependency is given as

$$R_{\text{spatial}}(\mu m) = \sqrt{\frac{p}{NA}^2 + (qzNA)^2}, \tag{1.18}$$

where z is the scintillator thickness in μm, NA is the nummerical aperture of the optical system and the coefficients are $p = 0.18$ and $q = 0.075$ [Koch et al., 1998]. A more detailed view of resolution can be found in section 3.3.

1.6 Computed tomography

If a sample is being imaged with a pixelated detector, each pixel in the detector records one ray from the X-ray source through the sample. The resulting image holds the intensity value of each ray after traversing the sample and is referred to as radiography. If the intensity of the incident beam is know before it reaches the sample, the attenuation of the sample along the ray can be calculated simply by re-ordering Equation 1.13. The problem of radiographies is their projective nature: elements in the sample that are ordered in different distances along the optical axis, are imaged on one 2-dimensional plane and therefore cannot be discriminated easily. This concept is very similar to the

shadow of a 3-dimensional object being 2-dimensional, except that in the case of X-ray radiographies each image point holds the value of the projection integral which is

$$p(s) = \int_0^s \mu(\eta)\mathrm{d}\eta, \tag{1.19}$$

where s is the thickness of the sample and $\mu(\eta)$ is the attenuation coefficient at the position η inside the sample. If a sample is being rotated perpendicular to the optical axis and several radiographies are taken at different angles, the attenuation coefficient at every voxel - the 3-dimensional equivalent of a pixel - can be reconstructed, which is referred to as tomography. In the following discussion, the reconstruction is limited to voxels on one slice through the sample, perpendicular to the rotation axis of the sample. The expansion to the 3-dimensional case is simply doing the same reconstruction for each of these slices along the rotation axis. In one sample plane, the distribution of the attenuation coefficient in carthesian coordinates is simply

$$\mu(\mathrm{x}, \mathrm{y}). \tag{1.20}$$

If this coordinate system is transformed into cylindrical coordinates, with the rotation axis being at the origin this distribution becomes

$$\mu(\theta, r), \tag{1.21}$$

with the coordinate transformations from carthesian coordinates being

$$r = \sqrt{x^2 + y^2} \tag{1.22}$$

as well as

$$\theta = \begin{cases} +\arccos\frac{x}{r} & \text{if} \quad y \geq 0 \\ -\arccos\frac{x}{r} & \text{if} \quad y < 0. \end{cases} \tag{1.23}$$

A ray through the sample can then be written as

$$x \cdot \cos(\theta) + y \cdot \cos(\theta) = r, \tag{1.24}$$

where θ is the viewing angle and r the distance from the origin. With this transformation, Equation 1.19 becomes

$$p(\theta, r) = \int \mu(x, y)\delta(x \cdot \cos(\theta) + y \cdot \sin(\theta) - r)\mathrm{d}x\mathrm{d}y \tag{1.25}$$

with δ being Dirac's delta function, with the properties described in subsection A.3.2. To get the attenuation coefficients from the measured projection, this function has to be reversed. If the projection is formulated as matrix multiplication with

$$p = R\mu, \tag{1.26}$$

with R being the Radon transform, this problem is equivalent to finding the inverse Radon transform or the inverse matrix R^{-1}. This is an ill-posed problem, which means that even the smallest noise in the measurement can completely destroy the inversion, which poses a problem since real measurements always

suffer from noise. Furthermore, calculating the inverse matrix directly is unfeasible due to its enormous size. However lately, the development in parallel computation on the Graphics Processing Unit (GPU), which is also treated in this work in a later chapter, may allow the computation of parts of that inverse matrix with reasonable time and computation resources [Gao and Blumensath, 2017], [Flores et al., 2015]. A different approach in solving the inverse problem is given by Fourier analysis, which will be explained in the following.

The Fourier transform F of a function f is defined to be

$$F(u) = \int_{-\infty}^{\infty} f(x) \cdot e^{-2\pi i u x} \mathrm{d}x \tag{1.27}$$

with its inverse being

$$f(x) = F^{-1}(F(u)) = \int_{-\infty}^{\infty} F(u) \cdot e^{2\pi i u x} \mathrm{d}u. \tag{1.28}$$

Now, the Fourier transform of the projections along a ray are equivalent to the two-dimensional Fourier transform of the object in radial coordinates, which is known as the Fourier slice theorem [Kalender, 2005, p. 294]. This leads to the identity

$$F(u_x, u_y) = F(u \cdot \cos(\theta), u \cdot \sin(\theta)) = P_\theta(u), \tag{1.29}$$

where $P_\theta(u)$ is the Fourier transform of $p_\theta(\vec{r})$, which is defined as

$$p_\theta(\vec{r}) = \int_0^s \mu(\theta, \eta) \mathrm{d}\eta. \tag{1.30}$$

The space defined via the coordinates (u_x, u_y) is called the spectral space, and if enough projections are measured the attenuation coefficients can be reconstructed by doing a backprojection, which can be written as

$$\mu'(x, y) = \int_0^\pi p_\theta(\vec{r}) \mathrm{d}\theta = \int_0^\pi p_\theta(x \cdot \cos(\theta) + y \cdot \sin(\theta)) \mathrm{d}\theta. \tag{1.31}$$

The μ' in this equation is not yet the correct μ. Due to the nature of the Fourier transform and because the projection integral is a positive function, there is a non-zero contribution to the value of a point from all the surrounding points. This results in a convolution of the attenuation coefficient with the Point Spread Function (PSF) $h(x, y)$ that can be written as

$$\mu'(x, y) = \mu(x, y) * h(x, y), \tag{1.32}$$

with the convolution as defined in Equation 3.19. If the PSF of a system is known, its influence can be reversed by deconvolution, however in general the PSF of a system is not known and another way of minimising its influence has

to be found. One of these ways is known under the term Filtered Back Projection (FBP). The FBP takes advantage from the fact, that after the convolution theorem, the fourier transform of the convolution of two functions in the real space can be expressed as the multiplication of the Fourier transforms of those two functions. To minimise the influence of the PSF, a filter kernel can be multiplied to the projection integral, which approximates the deconvolution. A simple example of such a filter kernel is the high-pass filter $H_\theta(r)$ which is defined as

$$H_\theta(r) = \int_{-\infty}^{\infty} P_\theta(u)|u| \cdot e^{2\pi i u r} \mathrm{d}u. \tag{1.33}$$

and simply becomes a multiplication due to the convolution theorem. Additionally, high frequency noise can be suppressed by using a windowing function $w(|u|)$. Put together, the algorithm for the FBP is

$$\mu(x, y) = \int_{0}^{\pi} F^{-1}\left(F(p_\theta(u) \cdot |u| \cdot w(|u|)\right) \mathrm{d}\theta. \tag{1.34}$$

Chapter 2

Neutron Imaging

2.1 Introduction

Neutrons are non-charged hadrons, consisting of one up-quark and two down-quarks, which is written as (udd). As they are particles with a spin of $\frac{1}{2}$, they belong both to the family of baryons and fermions. A single neutron has a mean radius of about 0.8×10^{-15} m and a mass of $m_\mathrm{n} = 1.675 \times 10^{-27}$ kg and is therefore subject to gravitational forces. Apart from the most common isotope of hydrogen, the nucleus of all atoms consists of several protons ans neutrons, which are hold together by the so called *residual strong force* or *nuclear force*. An unbound neutron or free neutron is unstable and suspect to beta decay with a half-life of about 10 minutes. The propagation of neutrons can be described by a particle wave following the Schrödinger equations. Therefore, a neutrons momentum can be described as

$$\vec{p_\mathrm{n}} = m_\mathrm{n} \cdot \vec{v} = \hbar \cdot \vec{k}, \tag{2.1}$$

with $\vec{v}$ being the velocity vector, $\vec{k}$ being the wave vector and $\hbar$ being Planck's constant. The energy of a neutron can be linked to its temperature using the Boltzmann constant k_B as in

$$E = \frac{1}{2}mv^2 = \frac{\hbar^2 k^2}{2m} =: k_\mathrm{B}T. \tag{2.2}$$

This leads to the useful conversion formula [Schreyer, 2008]

$$E(\mathrm{meV}) = 0.086T(\mathrm{K}). \tag{2.3}$$

Table 2.1 lists some of the properties of neutrons together with their label. Especially cold neutrons are slow enough to be influenced by mechanical beam shaping devices such as choppers or velocity selectors.

2.2 Production of neutrons

For the production of neutrons with a flux high enough for imaging, two commonly used methods exist: spallation and nuclear fission. In a spallation source,

Table 2.1: Properties of some selected energy ranges of neutrons according to [Wagner, 2017], [Schreyer, 2008], [Rangacharyulu, 2014]. Note that these labels are not exclusive.

Label	Energy	Temperature (K)	Wavelength (nm)	Velocity
ultrarelativistic	$> 10\,\mathrm{GeV}$			
relativistic	$0.1 - 10\,\mathrm{GeV}$			
fission	$2\,\mathrm{MeV}$			
continuum	$0.01 - 25\,\mathrm{MeV}$	$10^8 - 10^{12}$		$0.2\,c_0$
fast	$<1\,\mathrm{MeV}$			$0.4\,c_0$
epithermal resonance	$0.001 - 10\,\mathrm{keV}$	$10^4 - 10^8$	$>10^{-3}$	$0.001\,c_0$
low energy	$<1\,\mathrm{eV}$	≈ 11000		$\approx 3\,\mathrm{km/s}$
slow	$0.4\,\mathrm{eV}$	6000		
hot	$40 - 103\,\mathrm{meV}$	2300	0.05	$5000\,\mathrm{m/s}$
thermal	$3 - 150\,\mathrm{meV}$	300	0.2	$2200\,\mathrm{m/s}$
cold	$0.1 - 20\,\mathrm{meV}$	25	0.2 - 25	$600\,\mathrm{m/s}$
ultra cold	$< 0.01\,\mathrm{meV}$	< 0.001	10 - 1000	$5\,\mathrm{m/s}$

highly accelerated protons are shot onto a target, where they interact with the nuclei of the target atoms. This initial transfer of momentum from the impinging particle allows some nucleons (secondary particles) to leave the nucleus, often after cascading interactions with other nucleons, which leaves the nucleus in a highly excited state. The de-excitation of the excited nucleus (evaporation) happens via the release of neutrons. The secondary particles from the intra-nuclear cascade can lead to further spallation reactions in other nuclei, which are accumulated under the label *hadronic cascade* [Russell, 1990].

The nuclear fission process is mostly made usable as a neutron source in research reactors. This reactors have a reactor core with a fuel element, consisting of a material with a high fission cross-section e.g. ^{235}U. A high fission cross-section means, that the nucleus can capture an incident neutron, becomes unstable and decays into two lighter core fragments. This fission process leads to free neutrons that can lead to further fission reactions in a chain reaction. This neutron induced fission process is exemplary shown for ^{235}U in one possible equation:

$$^{235}_{92}\mathrm{U} + ^{1}_{0}\mathrm{n} \longrightarrow ^{139}_{56}\mathrm{Ba} + ^{95}_{36}\mathrm{Kr} + 2^{1}_{0}\mathrm{n}, \tag{2.4}$$

where n stands for a neutron. The fission cross-section depends on the energy of the incident neutron and is, for most elements used in reactors, higher for thermal neutrons than for fission neutrons. This is why fission neutrons have to be slowed down or *moderated* for an efficient reaction and a high neutron yield. This is done, by enclosing the fuel element in a suitable moderator medium, e.g. heavy water. The use of heavy water is preferred over normal water, as the absorption cross-section of deuterium is several magnitudes below that of hydrogen. All the neutrons from the hadronic cascade can either be directly used for experimentation or used in secondary sources. In secondary sources,

neutrons collide with a heated or cooled object and establish thermal equilibrium with it. Primary and secondary neutrons can then be guided towards experiments in neutron guides, which are beam guiding tubes with a reflective surface coating on the inside and filled with a gas with low interaction cross-section for neutrons. To control the speed of the fission chain-reaction, there is a control rod near to the fuel element, consisting of a material with high absorption cross-section to prevent excess neutrons from further chain reactions. To bring the reactor to a halt, there are several shutdown rods serving the same purpose as the control rod, that can usually been brought close to the fuel element in a very short amount of time for fail-safe operation. A very simplified schematic drawing of a research reactor for neutron production is shown in Figure 2.1. The availability of neutron sources is orders of magnitude below that of X-ray sources, as the facilities to produce neutrons are anything but trivial. An overview of existing and planned neutron sources can be found in [Anderson et al., 2016].

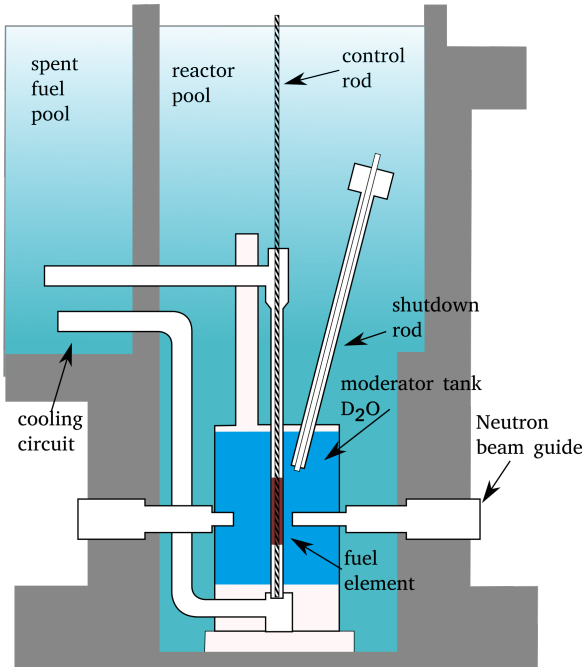

Figure 2.1: Simplified schematic drawing of a research reactor for neutron production. Only one shutdown rod and two neutron beam guides are shown for illustratory purposes. Adapted from [FRM2, 2017].

2.3 Interaction with matter

There are three different neutron interactions, that are useful for non-destructive testing of solid matter. The first of this three interactions is coherent nuclear scattering. As neutrons are non-charged nuclear particles, their interaction with atoms is described with the *strong interaction* with the neutrons and pro-

Table 2.2: Interaction cross-sections of neutrons and X-ray photons for some selected elements. All cross-sections are given in barn with $1\ b = 10 \times 10^{-24}\,\mathrm{cm}^2$. The scattering cross section $\sigma_{\mathrm{sc,N}}$ and the absorption cross section $\sigma_{\mathrm{ab,N}}$ for neutrons are tabulated for $v = 2200\,\mathrm{m/s}$ and taken from [Sears, 1992] and given without the error. The $\sigma_{\mathrm{tot,X-ray}}$ is the total absorption cross-section of X-ray photons calculated with [Berger et al., 2010] for $E = 50\,\mathrm{kV}$.

Isotope	$\sigma_{\mathrm{sc,N}}$	$\sigma_{\mathrm{ab,N}}$	$\sigma_{\mathrm{tot,X-ray}}$
${}_{1}\mathrm{H}$	82.02	0.3326	0.5616
${}^{2}_{1}\mathrm{H}$	7.64	0.000 519	
${}_{5}\mathrm{B}$	5.24	767	2.989
${}_{13}\mathrm{Al}$	1.503	0.231	16.49
${}_{18}\mathrm{Ar}$	0.683	0.675	46.51
${}^{36}_{18}\mathrm{Ar}$	77.9	5.2	
${}_{64}\mathrm{Gd}$	180	49 700	1008
${}^{157}_{64}\mathrm{Gd}$	1044	259 000	

tons in the atomic nuclei. The scattering process can be described by point scattering, as the short range of the strong interaction and the size of the nucleus are small (order of $\approx 10^{-15}$ m) compared to the wavelength of the neutron (order of $\approx 10^{-10}$ m) [Schreyer, 2008]. Furthermore, this leads to the scattering being independent of the scattering angle (isotropic). The second interaction is incoherent nuclear scattering. This interaction depends on the net spin of the neutron and the nucleus with which the neutron scatters. As the strength of this first two interactions depends on the composition of the atomic nucleus, the interaction varies wildly over the periodic table and can even be different for different isotopes of the same element, as can be seen in Table 2.2. The third interaction is magnetic dipole interaction. Despite its neutral net charge, the nuclear magnetic moment allows the neutron to interact with magnetic domains inside different materials. As this information mainly is retrieved via polarisation measurements, it will not further be discussed in this work. In general, the scattering lengths of neutrons are smaller than that of X-rays, allowing them to penetrate deeper in most materials. Besides these three main interaction processes, there are some more complicated interactions, that can have a contribution to the total absorption cross section but will not be discussed here, as their contribution to the information about the probed material is outside the scope of this work.

2.4 Detection of neutrons

As neutrons are electrically neutral particles and not considered to be directly ionising, they have to be converted to charged particles in order to be detected. There are several detection techniques that are able to detect the presence of a neutron, such as gas detectors or nuclear track emulsion detectors. However, for

imaging purposes, the detection principles are limited to energy and position sensitive measurements, which are ideally repeatable in short time-frames to allow for dynamic imaging. One practical detection method is the conversion of neutrons into secondary particles, that can be detected more easily. Exemplary the following possible reactions are shown:

$$^{10}\mathrm{B} + {}^{1}_{0}\mathrm{n} \longrightarrow {}^{7}\mathrm{Li}^{\star} + \alpha + 2.310\,\mathrm{MeV} \longrightarrow {}^{7}\mathrm{Li} + \gamma(0.48\,\mathrm{MeV}) \tag{2.5}$$

$$^{157}\mathrm{Gd} + {}^{1}_{0}\mathrm{n} \longrightarrow {}^{158}\mathrm{Gd} + \gamma(0.08, 0.18, 0.82\,\mathrm{keV}) + e^{-}(0.764\,\mathrm{MeV}). \tag{2.6}$$

These converter material can be implemented in a converter foil in front of a detector, that is able to detect the secondary particles [Jakubek et al., 2009]. Using the same conversion principle, these elements can be mixed with elements that have fluorescent characteristics for the secondary particles to form scintillators. Some regularly used scintillators together with their characteristics can be found in [Engels, 2011, p.14]. As the mean free paths of secondary particles are a main source for loss of resolution in neutron imaging, recent research is directed towards limiting the movement of the secondary particles e.g. by filling converter materials into structures such as defined by a `Micro-Channel-Plate (MCP)` [Siegmund et al., 2007].

Chapter 3

Optics

This chapter will give an introduction to imaging optics and establish the necessary foundations and terminology used in subsequent parts of this work. The field of geometrical optics covers all subjects of reflection and refraction of light rays through a single optical lens or arrays of lenses, called optical systems. As the inner workings of the microscope are of special importance for this work, most discussion will be done along this system as an example for an optical system. Towards the end of this chapter, some topics will include effects arising from the treatment of light as a electromagnetic wave rather than a particle.

Wave-particle dualism

Visible light can be described as a particle carrying energy. This particle is called a photon and exists only at one single place in time and space. At the same time, visible light can equally well be described as an electromagnetic wave in the wavelength range of approximately 400 – 700 nm, so that photons show all wave-optical effects such as interference, colour or diffraction and quantum effects such as tunneling, self-interference and the uncertainty principle[1]. This dualism is formulated in the **de Broglie** equations, that connect the rest mass of a particle m_0 and the velocity v at which it moves to the wavelength λ as

$$\lambda = \frac{h}{m_0 v}\sqrt{1 - \frac{v^2}{c_0^2}}, \tag{3.1}$$

where h is Planck's constant and c_0 the speed of light. In vacuum, light travels with a constant velocity $c_0 \approx 3.00 \times 10^8$ m/s and because of that, the rest mass of a photon is not defined. The **de Broglie** equation doesn't hold for that case, but although the rest mass of the photon being non-defined, or zero, photons do have momentum and therefore Planck's equation as shown in Equation 1.1 holds true. In a medium, light travels slower by a factor, that is called the index of refraction n with

$$n = \frac{c_0}{v}, \tag{3.2}$$

[1] As there is no non-relativistic description of the photon, the details are a little more complicated when treating one single photon and often the wave-formalism equally well describes the observed phenomena.

where v is the phase velocity, that can be understood as the apparent velocity of movement of one peak of the wave inside the medium. For imaging purposes, it makes sense to treat light as a bundle of rays to be able to calculate its way through optical systems. The neglected effects stemming from the wave-like nature of light lead to artefacts, which will be treated later in this chapter.

Snell's law

If a light ray crosses an interface between two media with different indices of refraction in a non-zero angle Θ to the surface normal, the direction of the ray will be changed according to Snell's law as

$$\frac{\sin\Theta_1}{\sin\Theta_2} = \frac{n_2}{n_1} = \frac{v_1}{v_2}, \tag{3.3}$$

where the subscripts stand for the two different media at the interface. This effect is called refraction.

Diffraction

If one follows the description of light as a wave, the application of the Huygens-Fresnel principle, which states, that every point of a wave-front acts itself as a point source, leads to a description of the propagation of this wave-front over time as a sum over all these secondary waves. This idea is closely related to the principle of interference, where the term interference is mostly used when a limited number of coherent light sources interact with each other and the term diffraction, when the interacting light sources are described via the secondary point sources of one wave-front [Feynman et al., 1963, 30-1]. In the field of geometrical optics, diffraction is neglected, as it is a result of the wave-like nature of light.

3.1 Thin lenses

In the most general sense, a lens is an optical element, leading to refraction of incident light, which is usually realised in form of one or more surfaces between continuous optical media. The exact shape of this surfaces has an influence on the direction of the light rays in the bundle. For example a *collection lens* can be shaped in such a way, that incident light-rays from a divergent point source exit the lens in parallel. If a parallel bundle of light-rays converges in one point after traversing a collection lens, this point is called the *focal point* of the lens. The direction, in which a central light ray hits the surface of the lens perpendicularly without being refracted is called the `optical axis`. A collection lens therefore refracts light rays towards the `optical axis`. In contrary, a *diverging* or *dispersing lens*, refracts light beams away from the `optical axis`. The simplest case is the spherical lens with two surface radii R_1 and R_2 as shown in Figure 3.1. If the material of such a spherical lens has an index of refraction n_{lens}, the distance of the focal point f' to the lens can be calculated to be

$$\frac{1}{f'} = \left(\frac{1}{R_1} - \frac{1}{R_2}\right)\left(\frac{n_{\text{lens}}}{n_0} - 1\right), \tag{3.4}$$

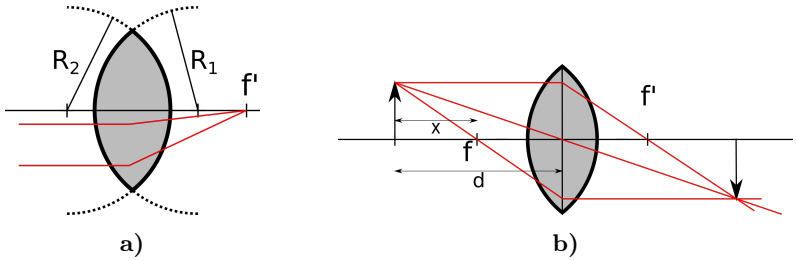

Figure 3.1: a) Schematic drawing of a biconvex lens with radii R_1 and R_2. The horizontal line denotes the optical axis. Marked in red are two par-axial light rays intersecting in the focal point f'. b) Schematic construction of the image of an object through a thin lens using par-axial light rays (red).

where n_0 is the index of refraction of the medium outside of the lens. This equation is often referred to as the lens-maker's equation, because it connects the geometrical shape of a lens to its optical properties and is true for thin lenses, where the distance between the zeniths of the spherical surfaces is small in comparison to the radii [Kühlke, 2011, p.60 f.].

Focal plane

So far, the focal point f' has been established as the point in which par-axial light rays intersect. Other light rays, that arrive at a collection lens in parallel, intersect at a different point, in the same distance f' away from the lens, but off-axis. All these points form the *focal plane*. It is an important feature of geometrical optics, that the way light rays are travelling can be reversed. Therefore, the focal distance f can also be defined on the other side of the lens, which will be called the *object side*. It follows, that light rays reaching the lens from a point source in the focal plane will exit the lens in parallel to each other. Furthermore, light rays from the focal point will exit the lens in parallel to the `optical axis`.

Magnification

If an object that emits light rays is placed in front of a lens, there is a plane behind the lens in which all light rays from one plane in the object will intersect, called the *image plane* The distance of the object to the lens and the optical characteristics of the lens will have an influence on the distance of the image plane to the lens and furthermore on the size of the image. The above mentioned characteristics of the thin lens together with the rule, that a light ray through the center of the lens is not refracted can be used to construct the image of a given object through a given lens. For the following discussion, the dashed variables will refer to the image side of the lens, whereas corresponding variables without a dash refer to the respective measures on the object side. According to the intercept theorem, the object size y corresponds to the image size y' as their distances. As a convention, if the image is upside down, as shown in Figure 3.1 b), the image size is written as a negative measure.

Therefore the proportionality can be written as

$$\frac{y}{|y'|} = \frac{d}{d'}. \tag{3.5}$$

On the image side the ray through f' leads to

$$\frac{y}{|y'|} = \frac{f'}{x'} = \frac{f'}{d' - f'}. \tag{3.6}$$

For a simple lens, the focal length is equal on both sides, therefore f' can be exchanged with f in the above equations. The magnification M_{optical} is defined as

$$M_{\text{optical}} = \frac{y'}{y} = \frac{-d'}{d} = -\frac{f}{x}. \tag{3.7}$$

This means, that the image is smaller than the object if $|M_{\text{optical}}| < 1$ and larger otherwise. Furthermore, the image is upside-down if the magnification is negative.

3.2 Microscope

A microscope is an arrangement of lenses to magnify an object for an observer, which might be the human eye or a digital image sensor. As described in section 3.1, a single lens can already be used as an optical magnification device, familiarly known as magnifying glass. To get to high magnifications with objects close to the imaging system, the focal distance has to be very small. A way to circumvent that is using the image that is produced by such a magnification lens, called the objective lens, as the object for a second lens, referred to as ocular or eyepiece, to further magnify the original object as shown in Figure 3.2. In an optical microscope, the tube length t is defined as the distance between the image side focal distance of the objective and the object side focal distance. If the image is viewed by a human eye, it is a good idea to arrange the lenses in such a way, that the intermediate image is in the focal plane of the second lens. In this arrangement, the rays leave the second lens in parallel and allow the observer to view the image with a relaxed eye, as the image occurs to be infinitely far away. In order to facilitate the manufacturing process and to be able to interchange pieces of the optical system, the tube length t is the same over many different microscopes and agreed on by many manufacturers to be $t = 160\,\text{mm}$. A microscope is not only a system of lenses, but usually also includes a light source. In the simplest designs, this light source is shining through the sample and projects the sample into the optics. Therefore, the resulting image is a function of the transmittance of the sample. Other microscope designs are based on reflection or fluorescence.

3.2.1 Magnification

As the microscope was developed as an optical instrument to be used with the human eye, the magnification is defined via the viewing angle. The viewing angle θ_{eye} is defined as the angle a ray from the object forms with the `optical axis`. If this angle is increased to θ_{system} when the object is viewed through

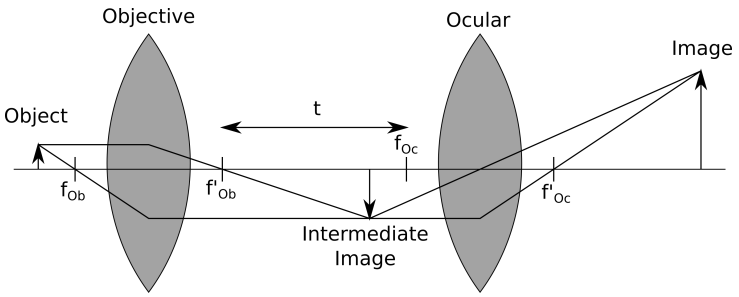

Figure 3.2: Schematic drawing of a two lens system. The intermediate image serves as object for the second lens. The distance t, which is the distance between the focal distance of the objective and the focal distance of the ocular is called the tube length.

an optical instrument, the object is seen to be larger. Using this definitions, the magnification of the system can be written to be

$$M_{\text{system}} = \frac{\tan(\theta_{\text{system}})}{\tan(\theta_{\text{eye}})} \tag{3.8}$$

With the magnification of the single lens as given in Equation 3.7, the magnification of the first lens can be written to be

$$M_{\text{objective}} = -\frac{t}{f'_{\text{objective}}} \tag{3.9}$$

with t being the tube length of the microscope. The resulting magnification of the complete microscope is the product of the magnification of the objective and the ocular lens

$$M_{\text{microscope}} = M_{\text{objective}} \cdot M_{\text{ocular}} = \frac{t \cdot a_{\text{s}}}{f'_{\text{objective}} \cdot f'_{\text{ocular}}}, \tag{3.10}$$

where $a_{\text{s}} = 25\,\text{cm}$ is the closest distance in which the human eye can see sharp [Pedrotti et al., 2008]. As the distances between the optical elements have to be fixed in a standard microscope, the sample can usually be moved along the `optical axis` in order to focus the system.

3.2.2 Imaging aberrations

Until now, all considerations followed ideal circumstances, especially regarding only points and rays which are close to the `optical axis`. In real world applications, there can be different deviations from ideal optical pathways that lead to errors. The origin of these errors is the small angle approximation

$$\sin(\Theta) \approx \Theta, \tag{3.11}$$

which holds true for small angles and therefore rays close to the `optical axis`. If the first two terms of the series expansion of the sine

$$\sin(\Theta) = \Theta - \frac{\Theta^3}{3!} + \frac{\Theta^5}{5!} - \frac{\Theta^7}{7!}... \tag{3.12}$$

are taken into consideration, one speaks of the third order error theory and therefore, the aberrations that arise from this approximation are called *third-order aberrations* or *Seidel aberrations* after the formulation of **Ludwig von Seidel** in 1857 [Hecht, 2001].

Spherical aberration

Light rays that travel through a lens far away from the `optical axis` are refracted stronger than rays close to the axis. When using a collection lens, the rays further away from the `optical axis` therefore have their focal point closer to the axis. In general, spherical aberration is a dependency of the focal distance on the distance of a ray from the `optical axis`. A schematic drawing can be found in Figure 3.3 a). Spherical aberrations also show on light rays that originate from point sources on the `optical axis` an reach the lens in a large angle to the `optical axis`. The reduction of spherical aberration can be achieved via the usage of combination of multiple lenses, so called *doublets*, that consist of combinations of each a collecting and a dispersing lens or by using aspherical lenses, which are a lot more difficult to produce than spherical lenses.

Koma

Koma is an image error, where bundles of light rays farer away from the `optical axis` meet in a point farer away from the central ray. The reason is, that the magnification is different for light bundles closer to the center than for those closer to the edge of the lens. In Figure 3.3 b), positive koma is depicted, where the rays closer to the edge intersect in points farer away from the `optical axis`. If this distance is on the other side of the central beam and therefore closer to the `optical axis`, one speaks of negative koma. An optical system, that is both corrected for spherical aberration and koma is called *aplanatic*.

Astigmatism

Light rays from point sources away from the `optical axis` can have different focal points for different planes. Figure 3.3 c) shows the sagittal- and meridional-plane of light rays from a circular object. Because these planes intersect the lens in different angles, their focal distance is different. Therefore the focal point of each plane is deformed into a line on the other plane respectively. Furthermore, the image of a circular object away from the `optical axis` is an ellipse, except at one plane between the focal line in the sagittal plane and the focal line in the meridional plane. This is also known as the *circle of least confusion*.

Distortion

Even in a system, that is corrected for all aforementioned aberrations, there can be further imaging errors. The effective magnification of an optical system can be different for different points and in general can be dependent on their distance to the `optical axis`. If the magnification decreases with the distance,

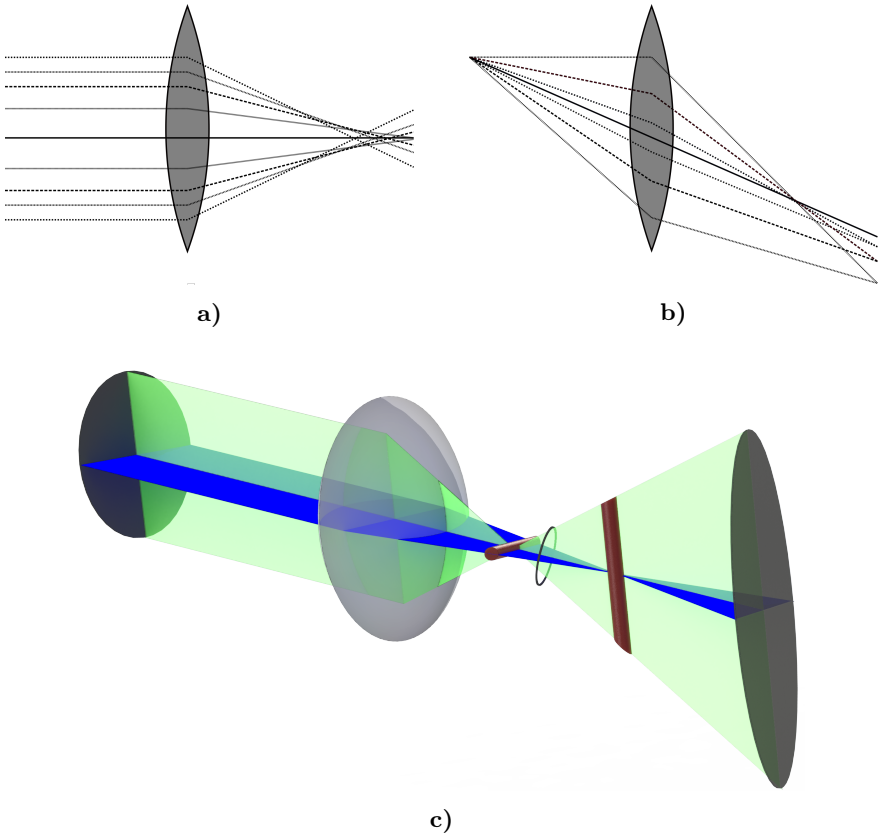

Figure 3.3: a) spherical aberration and b) Koma: Each set of equally dotted lines corresponds to a pair of light rays with the same distance to the central ray (solid black). c) Schematic drawing of astigmatism. The sagittal-plane is shown in blue, the meridional-plane in green. The circular object and the ellipsoidal image are shown in black. The red cylinders mark the position of the focal line of each plane, the black ring in between marks the circle of least confusion.

one speaks of barrel distortion, the opposite is called pincushion distortion. The influence of these distortions on a regular grid is shown in Figure 3.4.

Chromatic aberration

So far, the index of refraction n of a material was assumed to be a material constant. In reality, the index of refraction depends on the wavelength of the incident radiation, which is called `dispersion`. Therefore, chromatic aberration is an effect stemming from the wave-like nature of light. If polychromatic light is used with an optical system, it might have different characteristics for different wavelengths. For example, a system might have different focal planes or different magnifications for different wavelengths. Chromatic aberrations can be corrected with a suitable system of lenses. This correction is usually done for two or three characteristic wavelengths. If a system is corrected for the two

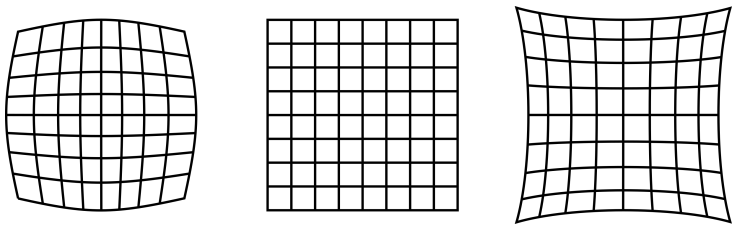

Figure 3.4: Distortion of a regular grid by magnification dependency on the distance to the optical axis. From left to right: Barrel distortion, undistorted object, pincushion distortion.

wavelengths $C' = 643.8\,\text{nm}$ and $F' = 480.0\,\text{nm}$, one speaks of an *achromatic* optical system, if it is furthermore corrected for the wavelength $\lambda = 546.1\,\text{nm}$, one speaks of an *apochromatic* optical system [Kühlke, 2011].

Corrections of aberrations

To correct for the aforementioned imaging errors, it is often necessary to use more complicated lens systems instead of single lenses. The focal distances in Equation 3.10 are then replaced by the effective focal lengths of the respective optical system. Manufacturers mark this lens systems with the effective magnification to facilitate the calculation of the system magnification of the microscope.

3.2.3 Infinity corrected microscope

As mentioned above, the tube length t plays an important role in determining the optical properties of a microscope. This means also, that by changing the tube length, these properties are affected. If one wants to add optical elements in the path between the objective and the ocular, one is limited to optical elements, that don't change the effective optical path length. This allows for the use of (ideal) mirrors inside the tube to change the path of the light away from the optical axis. The design of the so called infinity corrected microscope circumvents that requirement by changing the optical pathway. The objective in an infinity corrected system is designed in such a way, that light from the object leaves the objective in parallel bundles. The next optical element, referred to as tube lens, focusses these parallel bundles to form an intermediate image, which is then again magnified by the ocular. The area in which the light travels in parallel is often referred to as *infinity space*. In this infinity space, optical elements such as polarisers, prisms or beam splitters can be added without having to correct for the change in optical tube length [Greb, 2016]. Therefore infinity corrected microscopes can be used for a larger range of imaging applications such as fluorescence or phase contrast microscopy. In an infinity corrected microscope, the magnification M_{infinity} can simply be calculated to be the fraction of the focal distances of the objective and the tube length

$$M_{\text{infinity}} = \frac{f_{\text{tubelength}}}{f_{\text{objective}}}. \tag{3.13}$$

3.2.4 Depth of field

When imaging with microscopes, it is necessary to focus the optics onto the sample. One speaks about the focal plane of the objective as the distance in which the sample is in focus. Due to diffraction, the extend of this plane along the `optical axis` is non-zero. This means, that there is a non-zero distance from the focal plane, in which points from the sample still can be in focus. This distance is termed *depth of field* or equally well *depth of focus*. When imaging with scintillators, this also corresponds to the optically ideal thickness of the scintillator, as all layers outside the depth of field only contribute to the background of the image. **Spring and Davidson** describe the total depth of field d_{tot}, resulting from the wave optical case at high numerical apertures and the geometrical *circle of confusion* at low numerical apertures to be

$$d_{\text{tot}} = \frac{\lambda n}{NA^2} + \frac{n}{M \cdot NA} e, \tag{3.14}$$

where λ is the wavelength of the used light, n is the index of refraction of the medium between sample and objective, M is the magnification, NA is the numerical aperture of the objective and e is the smallest distance, that can be resolved by a detector in the image plane [Spring and Davidson, 2017]. In the case of pixelated detectors, e is therefore equal to the pixel size. Some values of the calculated depth of field can be found in Table 6.2.

3.3 Resolution

Resolution describes the ability of an optical system to discriminate two distinct points of an object in the image plane. For example the resolution of the human eye can be described via the distance of two black points on a white background that can be distinguished by an observer. In this section, the theoretical limits of optical instruments are treated. In chapter 6, the applicability and limits of these concepts will be discussed.

Abbe-limit

In 1873, **Ernst Abbe** found an expression for the resolution of optical systems, that is based on the idea of diffraction of incoming light at an array of lines. The light from one single object point forms a diffraction pattern in the image plane, which consists of a central, bright spot, surrounded by rings of alternating high and low intensity areas. The whole pattern is known under the term *Airy disk* and the areas of high intensity are referred to as diffraction spot or diffraction rings respectively. With an ideal, focussed microscope, the minima in-between these rings have zero intensity [Silfies et al., 2017]. The Abbe-limit is the distance two object points can have in such a way, that the central maxima of their Airy disks in the image plane don't overlap. This is dependent on the wavelength λ and the angle Θ of the incident light as well as the index of refraction n of the medium in which the optical system is operating. The Abbe-limit therefore is

$$d_{\text{Abbe}_{\text{central}}} = \frac{\lambda}{n \sin(\Theta)}. \tag{3.15}$$

In this equation, the term $n\sin(\Theta)$ is often referred to as the numerical aperture NA, which is a measure of the opening angle of a microscope objective. From Equation 3.15 it is evident, that to achieve higher resolution one can use light with a lower wavelength or increase the numerical aperture of the microscope. The upper limit to the NA of an objective working in air ($n_{\text{air}} = 1$) is 1, a higher NA can only be achieved by using an *immersion microscope*, where the medium (immersion oil) between the sample and the objective has an index of refraction $n_{\text{oil}} > 1$. In order to push the resolution of a microscope below the Abbe-limit in Equation 3.15, one can use an extra lens in the beam path between light source and sample, referred to as *condenser*. This lens is used to focus the incoming light onto the sample and for best performance has to be matched to the microscope objective. As the condenser lens or system also has an numerical aperture $NA_{\text{condensor}}$, the resolution limit becomes

$$d_{\text{Abbe}} = \frac{\lambda}{NA_{\text{objective}} + NA_{\text{condensor}}}, \tag{3.16}$$

as long as $NA_{\text{objective}} > NA_{\text{condensor}}$. This equation collapses to Equation 3.15 if no condenser is used and the respective NA becomes zero. Furthermore, if the condenser and the objective have the same NA, the equation becomes

$$d_{\text{Abbe}} = \frac{\lambda}{2NA}, \tag{3.17}$$

which is alternatively referred to as Abbe-limit.

Rayleigh-limit

Another approach in defining the theoretical resolution limit of an optical system is regarding two points in the object plane as separate light sources. According to the Rayleigh-limit, two points can be resolved as two distinct points in the image plane if their distance is larger than

$$d_{\text{Rayleigh}} = 0.61\frac{\lambda}{NA}. \tag{3.18}$$

In this distance, the Airy disks of the points overlap in such a way, that the central maximum of one lays in the first minimum of the other. As both these definitions rely on the diffraction of light as the ultimate reason for a resolution limit, they are termed the *diffraction limit* of resolution.

3.3.1 Transfer functions

So far, the term Airy disk was used to describe one possible diffraction pattern that stems from light from a point source, that is diffracted at the edges of beam limiting elements, such as the circular aperture of an objective. An example of such an Airy disk, produced by a red laser that is being shone unto a pinhole can be seen in Figure 3.5. This Airy disk is only the result for an ideal optical system without aberrations. In a real optical system, there might be different factors influencing the exact size and shape of the diffraction pattern of one single light source. The resulting diffraction pattern is referred to as the `PSF` of the optical system. If the optical system is a linear system, meaning that

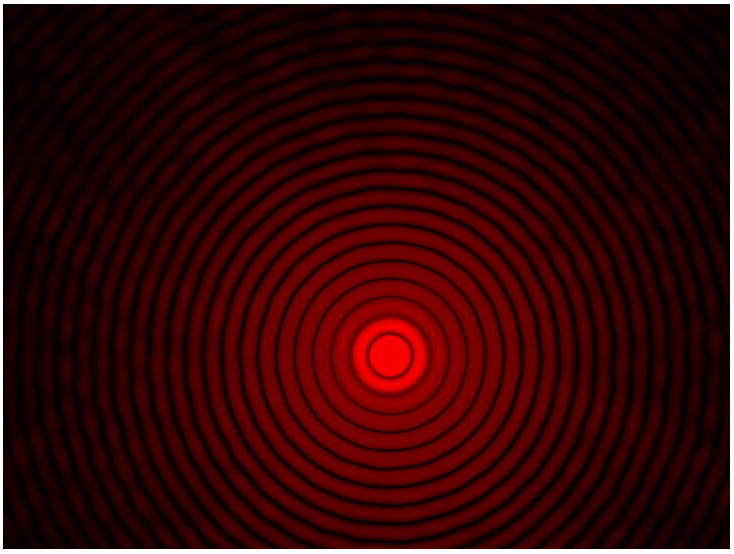

Figure 3.5: Photography of the diffraction pattern of a red laser through a 0.09 mm big pinhole, known as Airy disk. Image taken by Wikimedia user Bautsch, published under Creative Commons license CC0 1.0 [Wikimedia Commons, 2017].

the PSF is invariant to shifts in space and time, the intensity of the image is the convolution of the object intensity with the PSF [Kühlke, 2011, p.105]. The convolution of two functions is defined as

$$f_1 * f_2 := \iint_{-\infty}^{\infty} f_1(x - x', y - y') f_2(x', y') \mathrm{d}x' \mathrm{d}y'. \tag{3.19}$$

Following the derivation of **Pedrotti et al.**, the imaging path of the object intensity I_{object} with an imaging operator A can be written as

$$I_{\text{image}}(X, Y) = A I_{\text{object}}(x, y). \tag{3.20}$$

The PSF of a spatial invariant optical system is introduced to be

$$h(X, Y) = A\delta(0, 0), \tag{3.21}$$

where δ defines the delta function, whose most important characteristics are described in subsection A.3.2. Therefore, the image intensity follows to be the addition of the PSF of each point in the object weighted with their intensity:

$$I_{\text{image}}(X, Y) = \iint h(X - x, Y - y) I_{\text{object}}(x, y) \mathrm{d}x \mathrm{d}y. \tag{3.22}$$

This can be written as convolution

$$I_{\text{image}} = h * I_{\text{object}}. \tag{3.23}$$

The Fourier transformation $\mathcal{F}$ of a one-dimensional function is defined to be

$$\mathcal{F}(f(y)) := \frac{1}{2\pi} \int f(x) e^{-iyx} \mathrm{d}x. \tag{3.24}$$

It is an important characteristic of the Fourier transformation, that the Fourier transformation of the convolution of two functions becomes a multiplication of their Fourier-transforms, and therefore it follows that

$$\mathcal{F}(I_{\text{image}}) = \mathcal{F}(h * I_{\text{object}}) = \mathcal{F}(h)\mathcal{F}(I_{\text{object}}), \tag{3.25}$$

which is also known as *convolution theorem*. [Pedrotti et al., 2008, p.746 ff.] The Fourier transform of the PSF is often referred to as *Optical Transfer Function* (OTF). As this OTF is a complex function in general, its magnitude is referred to as *Modulation Transfer Function* (MTF) and its phase as *Phase Transfer Function* (PTF). It is evident, that there is a connection between these transfer functions and the achievable resolution of an optical system. Therefore an alternative way of specifying the resolution of an optical system is measuring the width of the PSF, where it has fallen to 50 % of its peak value. This is known as the *Full Width at Half Maximum* (FWHM). Figure 3.6 shows the simulation of two point sources with varying distances as seen by a pixelated detector. Several characteristics of a detection setup influence the MTF of the

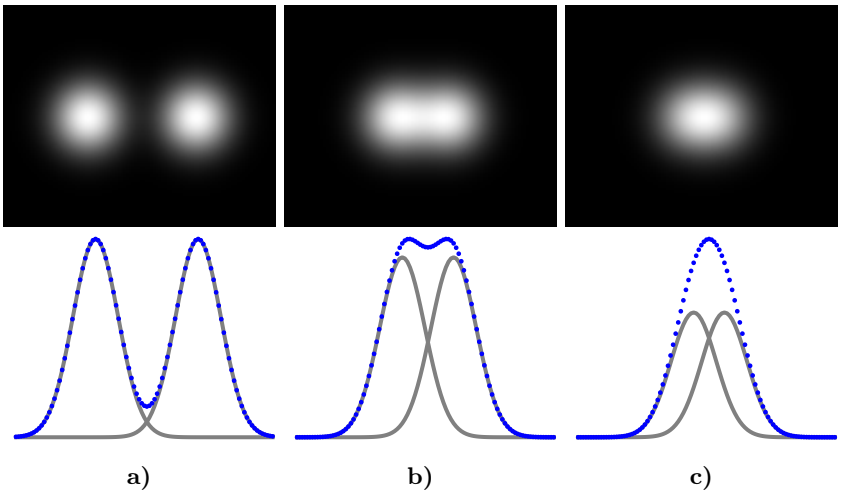

Figure 3.6: Top row: Simulated image of two point sources with varying distance and Gaussian intensity distribution. Bottom row: Line plot through the center of the corresponding image, normalized to the maximum. Grey lines show the contribution of the single light source, the blue dots show the resulting intensity profile. In a), the point sources are far away. In b), the distance of the light sources is chosen to be equal to the FWHM of the resulting intensity distribution on the detector, whereas in c) the distance is smaller and the two light sources are no longer resolved.

system. In the general case of a linear system, it is enough to multiply the MTFs of the respective imaging elements together to get the resulting MTF of the whole system. If the MTF of other processes, such as scattering, is additionally taken into consideration, the expression can become more complicated. As an example, **Jain et al.** show the *Generalized MTF* (GMTF) of a system to be the combinations of "the MTFs for detector (MTF_{D}), focal spot (MTF_{F}), and

scatter $(MTF_{\mathrm{S}})[...]$:

$$GMTF(u,v,\rho,m) = \left[(1-\rho)MTF_{\mathrm{F}}\left(\left(\frac{m-1}{m}\right)(u,v)\right) + \rho MTF_{\mathrm{S}}\left(\frac{(u,v)}{m}\right)\right] \cdot MTF_{\mathrm{D}}\left(\frac{(u,v)}{m}\right), \tag{3.26}$$

where u and v are spatial frequency in the object plane, m is the magnification of features in the object plane onto the detector plane, and the scatter fraction ρ is defined as,

$$\rho = \frac{S}{S+P} \tag{3.27}$$

where S and P are scatter and primary components, respectively" [Jain et al., 2010].

Chapter 4

Image Processing

This chapter will start with the image processing basics and establish the terminology. Following, the imaging pathway through the camera will be explained with a focus on noise. Image processing steps and methods will be explained and demonstrated along some examples. The chapter will finish with some information about the implementation of the image processing algorithms.

4.1 Terminology

Sampling and interpolation

Sampling can be understood as a mapping of a continuous function onto a discrete representation. This can be done in the spatial or the temporal domain, and one speaks of spatial- or temporal-sampling correspondingly. One single value of the underlying continuous function at one specific point in space or time (or both) is called a sample. If the number of samples from a given function is decreased, one speaks of downsampling. As an example, the downsampling of an image with the factor two, halves its resolution. Increasing the number of samples without knowing the original continuous function does not lead to any additional information. For image processing, it is often necessary to get information between sampling points. This is done via interpolation. In the simplest case, the value of the sample next to the desired point is taken. This process is called nearest neighbour interpolation. For higher precision, a function is fitted to the discrete data points and the interpolated value is taken from that fitted function. Depending on the type of the function, one speaks about square-, cubic-, or spline interpolation and it is possible to take more points into account than just the two samples closest to the interpolation position. If the underlying function is a higher-dimensional one, which is true for images, the interpolation steps can be repeated for the different independent variables. The linear interpolation on each axis of a two-dimensional image is e.g. called the bilinear interpolation.

Digitalisation

To store and process information which is given in continuous, analogous form, a digitalisation step is necessary in addition to a sampling step. Usually this

can be described as mapping a continuous input range of values to a discrete range of values, that can be stored and therefore is comparable to sampling in the data domain.

Image

For image processing concerns, we are talking about digital images rather than images in the optical sense. A digital image is an array of discrete samples in two- or three-dimensional space, sampling a continuous object with regard to the imaging modality. For example a picture taken with a digital camera is a spatial and temporal sampling of the light rays transmitted, reflected or emitted from the pictured object during the acquisition time.

Pixel and voxel

The word pixel is used ambiguously, as a unit cell on a detector, the smallest unit on a data displaying device or the smallest bit of information in a two-dimensional image. In this work, the latter use of the word is used when talking about image processing. However, there is an intrinsic connection: When imaging an object, using a pixelated detector, the recorded data points correspond to the digitalised information from the detector pixels and are represented in the image pixels in the case of an unprocessed image. If the concept of pixels is transferred to three-dimensional space, one speaks about voxels.

Resolution

Resolution is another term, used widely and in different meanings. In section 3.3, the optical resolution is defined. However, in image processing the resolution of an image is merely its size given in pixels or the density of physical pixels on a surface on e.g. a detector or a sensor. In this work, the term resolution will always refer to the optical resolution, in contrast the term pixel-size is used where appropriate.

4.2 Imaging with pixelated detectors

Pixelated detectors are detectors, whose active area is physically subdivided into elements that often share a common set of readout electronics. One distinguishes between counting and integrating detectors. Counting detectors are able to record one single event e.g. an incident particle per pixel inside the boundary condition of low light levels. Integrating detectors have an output that corresponds to the integrated signal over the area of one pixel and the acquisition time. This thesis will focus on EMCCD cameras, which are integrating pixel detectors.

4.2.1 Particle detection

Any detection of particles by a detector involves the transfer of energy from the particle to the detector. As the amount of this energy transfer usually is very low compared to the thermal energy of the detector's particles it does not suffice to simply measure the energy transfer directly. However, in suitable materials,

the energy transfer of a particle to a detector can lead to localized effects, which are distinguishable from those caused by thermal effects [Gilmore, 1992]. Some of the interaction processes described in section 1.4 and section 2.3 inhibit this property, the photo effect being the primary one when it comes to the detection of light with CCDs.

4.2.2 Charge coupled devices (CCD)

A charge coupled device (CCD) sensor, usually is an array of photodiodes, with each photodiode corresponding to one detector pixel. In principle, each photodiode is a doped semiconductor, coated with an insulator and contacted with two electrodes. If a voltage is applied to the electrodes, the band-structure of the semiconductor forms a potential well, in which charge can be trapped. If a particle, with an energy exceeding the band-gap in the semiconductor hits this arrangement, it can produce an electron-hole pair via the photo effect. The applied voltage leads to a separation of charge and a collection inside the potential well. The applied voltage of such an array can be varied in a way, that the trapped charges are shifted along a row or a line inside a CCD array from one pixel to another neighbouring one. This can be done subsequently, until the charges reach the readout electronics of the CCD chip, called readout registers. Therefore, the signal of neighbouring pixels arrives at the readout registers in serial.

4.2.3 EMCCD

The further development of CCD chips lead to an additional electron multiplication register directly behind the readout register, giving the `Electron Multiplying Charge Coupled Device (EMCCD)` their name. In principle, with each transfer of electrons to a neighbouring register, there is a non-zero probability, that any electron leads to the formation of another electron-hole pair via impact ionisation. To facilitate the process of impact ionisation and therefore an effective gain in signal, the EM gain registers are contacted with a second electrode at a much higher voltage than necessary for charge transfer alone and multiple instances of this gain register cells are chained together.

4.2.4 Signal count

Due to the inner workings of (EM)CCD cameras, the number of counts retrieved does not directly correspond to the number of incident photons. The process to retrieve the number of photons from the signal count is a multi-stage process and will be explained in the following. In most cameras, a constant electronic offset is added to the signal in order to improve the dynamic range close to zero. This constant bias might be different for different settings of the readout electronics and therefore has to be measured. This can be easily done via subtraction of an empty dark-current image. In a next step, the signal counts are corrected for the sensitivity of the electronics. The sensitivity gives the number of electrons needed to produce one count in the analog-digital (A/D) converter of the system. The now retrieved counts correspond to the electrons reaching the A/D converter. In an EMCCD, this signal has to be divided with

the EM gain factor to retrieve the numbers of electrons (actually electron-hole pairs) produced in the semiconductor of the CCD chip. To get the number of photons from this number, the quantum efficiency (QE) of the CCD has to be known. The QE defines the number of electrons that can be produced by one photon with given wavelength. Due to the principle of the inner photo effect, this number is dependent on the wavelength of the incident light and always smaller than unity. Therefore it can also be interpreted as the probability that one single photon produces one electron-hole pair.

4.2.5 Noise

In general, noise is an inherent uncertainty in any measured signal. If for example a constant number of photons fall onto a CCD sensor, due to the statistical quality of the conversion and detection process, the signal may show different outputs for the same number of incident photons per unit of time. Different sources of noise can be distinguished and their influence on the detection process explained. Furthermore, the strength of the different noise sources usually depends on different external parameters. This section will treat the different sources of noise, typically present in experiments where light is detected with CCDs or flat-panel detectors.

Dark current

Even if no actual signal is measured with a CCD, there can be a non-zero output. This can be due to the thermal energy of electrons inside the semiconductor material. If any thermal movement leads to the release of a charge carrying particle, this can be detected as a non-zero current. The strength of this effect is strongly dependent on the movement of particles inside the detector material and therefore on the temperature of the detector. This is why cooling of the detector helps in significantly reducing this source of noise. The strength of the dark current is exponentially falling with decreasing temperatures with a rule of thumb giving half the dark current with a decrease in temperature of 7 K [Widenhorn et al., 2002][ON Semiconductor, 2014]. Besides the possibility to lower the dark current via cooling, its effect on the final image can be decreased via the subtraction of an image which is taken without any signal present (dark image).

Readout noise

During the readout process, the electronic signals pass through a very sophisticated set of electronic circuits. Especially any electronic amplification of signal levels introduces noise. Furthermore there is the chance of electronic interference (for example with the power supply of the camera). This type of signal is independent on signal levels and varies only slightly with the temperature. The readout noise has a very strong dependence on the set of used readout electronics together with their intrinsic settings. If a camera has one ore more distinct sets of readouts, amplifiers or analog-digital converters, the readout noise is characteristic for each of this sets and might differ in orders of magnitude. The readout noise is modelled to be a Gaussian distribution around the

electronic bias of the readout, which is a fixed number. For the camera, used mostly in this work, the values are given in Table 4.1.

Table 4.1: Noise values from the Andor iXon Ultra Performance Sheet. The two different readout channels with and without EM amplification are listed at different readout rates and different settings of the pre-amplifier. The sensitivity defines how many electrons are needed to give one single count in the analog-digital converter. The Noise is the measured RMS of the single pixel noise at −75 °C and corresponds to the standard deviation of the Gaussian noise distribution.

System Readout Rate	Preamp	Sensitivity	Noise
17 MHz EM amplifier	1	16.2	284
	2	9.02	158
	3	5.11	86.7
10 MHz EM amplifier	1	15.0	162
	2	7.91	92
	3	4.79	64.9
5 MHz EM amplifier	1	16.8	69.1
	2	8.03	45.3
	3	4.28	37.5
1 MHz EM amplifier	1	16.9	25.5
	2	8.17	17.4
	3	4.27	15.0
3 MHz conventional amplifier	1	3.86	13.7
	2	2.98	11.8
	3	1.40	9.66
1 MHz conventional amplifier	1	3.86	7.18
	2	2.95	6.43
	3	1.38	5.33
0.08 MHz conventional amplifier	1	3.81	3.54
	2	2.99	3.38
	3	1.39	2.97

As the readout noise is pretty much constant in regard to the signal level, it gets smaller in relation to the signal if the signal is amplified before readout. Therefore, with a high enough sensitivity of the CCD or strong amplification of the signal, the readout noise gets insignificant. In an EMCCD this leads to a trade-off between readout noise and the multiplicative noise mentioned below.

Shot noise

Shot noise is the representation of the statistical nature of signals. If for example the same number of photons is incident onto a CCD detector per image, the pixel count may vary due to the exact position of each single photon being randomly distributed. The probability of the arrival of a single photon per unit of time follows a Poisson distribution. This source of noise is especially dominant if only a small number of photons is collected during the exposure time. Therefore the influence of shot noise is reduced when the signal count

is increased, either by increasing the incident flux or the exposure time. Both signal and dark current are suspect to shot noise. The shot noise is scaling as $\sqrt{n}$, with n being the number of events, therefore amplifying the signal before readout improves the signal to noise ratio. This can be achieved by using the gain register in an EMCCD.

Fixed Pattern Noise (FPN)

As a CCD chip is a semiconductor device, there might be impurities, defects or other influences that lead to different pixels having a different response to the incident signal. Defective pixels might produce no signal at all (cold pixels) or a very high signal close to saturation (hot pixels). On top of that, as the CCD readout is a serial one, the different readout time of pixels may lead to a different level of dark current or to a noise contribution by the readout electronics if they are not temporally stable. This noise source can be reduced by background subtraction, which is usually done with flat-field correction. Additionally a mask for dead pixels can be used to eliminate their influence.

Multiplicative noise

Especially in EMCCDs, the effective gain from one single signal electron traversing the gain register is unknown. As the underlying process is a stochastic one, it is only possible to calculate probabilities for certain output gains with a given input signal. **Robbins et al.** define the noise factor F to be

$$F^2 = \frac{{\sigma_{\text{out}}}^2}{M^2 {\sigma_{\text{in}}}^2}, \tag{4.1}$$

where M is the mean gain and σ^2 are the respective variances of the input and output signals [Robbins and Hadwen, 2003]. Furthermore, they derive an equation for the noise factor, that depends only on the number N of gain stages in the gain register and the gain factor M:

$$F^2 = 2(M-1) \cdot M^{-\frac{N+1}{N}} + \frac{1}{M}. \tag{4.2}$$

From this equation, it can be seen, that F^2 rapidly goes towards 2 when the gain is increased and is unity for no gain. This result is pretty much constant for a wide range of gain stages. There are two equivalent ways to interpret the influence of multiplicative noise onto the signal. On the one hand, one can simply multiply the noise with the shot noise to get the resulting overall readout noise. On the other hand, the multiplicative noise can be seen as a factor decreasing the effective quantum efficiency of the sensor. Therefore, a multiplicative noise factor of $F^2 = 2$ halves the quantum efficiency of the sensor [Basden et al., 2003].

Total noise

The total noise is dependent on many different factors mentioned above. All of the sources of noise mentioned above add together to yield the total noise. After the rules of the Gaussian propagation of uncertainty and under the assumption,

that the different sources of noise are mostly independent, the total noise is calculated as:

$$\text{noise}_{\text{total}} = \sqrt{\text{noise}_{\text{readout}}{}^2 + \text{shotnoise}_{\text{dark}}{}^2 + \text{shotnoise}_{\text{signal}}{}^2}. \tag{4.3}$$

4.2.6 Background

In contrast to noise, which is inherent to the measured signal, there is also the possibility to measure events, which are objectionable or unwanted and therefore referred to as `background` or underground signal.

Stray light

Especially in applications, where very low light levels are to be detected, it is crucial to operate the measuring setup in light tight environments. At the same time, it is desirable for an operator to access the setup for sample changes or modifications. Special care has to be taken, that no stray light is allowed to arrive inside the setup through any encasing and the setup itself has to be constructed in such a way, that for example auto-fluorescence of any part or even the light from signal LEDs on any device might not reach the sensor. If imaging a scintillator with a microscope objective, another source of stray light is the scintillator itself. As the focal depth of any objective is limited, parts of the scintillator that lay outside the focal depth contribute light, that is in effect unfocussed and contributes to the overall background. In the design of a setup, it is therefore necessary to match the scintillator thickness to the focal depth of the employed optics for the lowest possible background.

Gamma spots

When high energy particles directly hit the detector inside the camera, they can produce a signal via the photoelectric effect. This signal usually is a lot higher than the signal produced by visible light photons. In cases, where the resulting charge is too large to be completely trapped inside the potential well of the pixel, the charge can spread to neighbouring pixels. This effect is also known as blooming. If the energy of the incoming particle is high enough or the particle hits the detector during the readout phase, the charge spread can lead to one or more lines of subsequent pixels being over-exposed. This effect is known as smear effect. Both effects lead to corrupted data in the affected sensor area. As CCD sensors are designed to facilitate the flow of charges in the vertical direction, the excess charge manifests as streaks along the vertical direction of the CCD sensor. An example of two direct detections of high energy gammas on the sensor are shown in Figure 4.1. In the described setup, those high energy particles are X-ray photons, therefore there are always present, when the X-ray tube is running. When measuring with neutron sources, those high-energy particles can stem from nuclear reactions such as activation of materials close to the detector. This means that both the signal image and the flat-field image have to be corrected before they are used further. The registration of gamma spots can be decreased, if adequate shielding is introduced into the setup. This requirement often leads to design choices in the setup, where the detector is placed outside the direction of the primary beam.

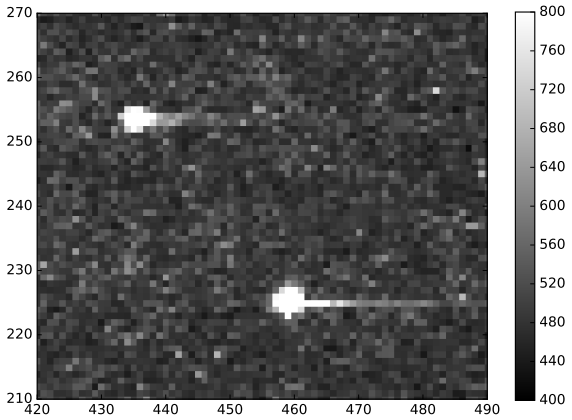

Figure 4.1: Direct hits of two high energy particles on the detector. The camera is rotated 90° counter-clockwise; the bottom of the camera is on the right side of the image.

Scintillator effects

When a scintillation screen is employed inside the setup, there can be additional effects leading to a background signal. If the decay time of a scintillator is larger than the acquisition time per frame in a dynamic measurement, there is chance to register light contributions from events that occurred in the past. This is referred to afterglow and can only be minimised by choosing an adequate scintillator material. Another inherent problem is the temporal non-linearity of some scintillator materials. It is possible, that scintillation properties change over time, e.g. by bleaching, and the efficiency therefore changes during the measurement. This effect can be minimised by taking several flat-field images without a sample in the beam at different times and correct each acquisition with the nearest set of correction images.

4.3 Image registration

4.3.1 Motivation

In imaging, one often deals with movement of the measuring system relative to the sample or different beam paths for different imaging modalities. This leads to images from the same sample being distorted relative to each other. When the measuring system is stable over time and one only deals with shifts of relative positions between the datasets from different beam paths or different modalities, there is often a simple geometric transformation to overlay both results over each other. In this case, the goal is to find this transformation. If this transformation is then applied to the dataset, the resulting dataset is registered, meaning that pixels or voxels from one dataset correspond to pixels or voxels from the other dataset. This is an essential step to gain additional information in imaging with different modalities. For the following sections,

the image which is not transformed during the registration is referred to as the `template` T and the image which is transformed as `image` I.

4.3.2 Implementation

Registration models

Depending on the origin of distortion of the image, there can be a restriction on the free parameters of the image transform needed to register the image to the template. This free parameters are grouped in different registration models. More general, a model can be understood as a mapping from one set of coordinates to another. The affine transformation is a very commonly used transformation and is therefore used as an illustrative example. If an image has the coordinates x and y, the new coordinates X and Y after affine transformation can be written as

$$X = s_{\mathrm{x}} \cdot \cos(r) \cdot x - s_{\mathrm{y}} \cdot \sin(r + c) \cdot y + a_2 = a_0 \cdot x + a_1 \cdot y + a_2 \tag{4.4}$$

and

$$Y = s_{\mathrm{x}} \cdot \sin(r) \cdot x - s_{\mathrm{y}} \cdot \cos(r + c) \cdot y + b_2 = b_0 \cdot x + b_1 \cdot y + b_2, \tag{4.5}$$

where s is the scaling factor in both dimensions respectively, r is the rotation, c is the shear and a_2 and b_2 are the shifts in each dimension. With this definition, the image transform can be written as

$$\begin{bmatrix} X \\ Y \\ 1 \end{bmatrix} = \begin{bmatrix} a_1 & a_2 & a_3 \\ b_1 & b_2 & b_3 \\ 0 & 0 & 1 \end{bmatrix} \begin{bmatrix} x \\ y \\ 1 \end{bmatrix}. \tag{4.6}$$

In general, this equation is a function of the coordinate vector $\vec{x}$ and the vector $\vec{p} = [p_0, ..., p_n]$ that holds the n free parameters $[a_1, ..., b_3]$. Any subset of these six free parameters is a restriction to the general affine transformation. Most transforms will lead to non-integer coordinates, and therefore the transformed image has to be interpolated to yield values at the original coordinates. The following, most often used and implemented, transforms are ordered on their degrees of freedom.

- **RotationCenter:** A rotation around the image center.
- **Shift:** A shift of the image along its x- and y-axis.
- **IsoscaleShift:** A shift transform and a scale of the x- and y-axis with the same scaling factor.
- **Rotation:** A rotation around an arbitrary point.
- **Rigid:** Like the **Shift** but with added rotation around the origin.
- **ScaleShift:** Like **IsoscaleShift** but with different scaling factors for each axis.
- **Affine:** Fit of all six free parameters of the affine transformation.

More complex image transforms can be implemented by defining this transformation matrices and finding the respective Jacobian. Furthermore, affine transformations can be chained together in a multiplicative manner. As an example, the rotation around an arbitrary point was found by shifting the coordinate system to the origin, by a translation $T(-x, -y)$, a rotation around the origin $R(\theta)$ and a shift back to the original position $T(x, y)$. The resulting rotation matrix can be found by the matrix multiplication

$$T(x, y)R(\theta)T(-x, -y), \tag{4.7}$$

where the transformations appear from right to left in order of execution, because the point on which they are acting is multiplied on the right. The result and explicit notation of the transformation matrices and the corresponding Jacobians can be found in section A.4. Projective transforms are implemented in the same way, but are outside of the scope of this work.

Registration step

The implemented registration in this work is a slightly modified version of the iterative registration algorithm as described by **Lucas and Kanade** in [Lucas and Kanade, 1981]. This section follows closely the derivations of **Baker and Matthews** in [Baker and Matthews, 2004]. The right hand side of Equation 4.6 is often called a `warp` and written as $W(\vec{x}, \vec{p})$. The goal of image registration is, to minimize the difference, between the template and the warped image

$$\sum_x [I(W(\vec{x}, \vec{p})) - T(\vec{x})]^2. \tag{4.8}$$

The idea behind the Lucas-Kanade algorithm, is to start with an initial guess for the vector $\vec{p}$ and updating it in each iteration step to minimize the equation above. With this in mind, the first order Taylor expansion of Equation 4.8 on $\vec{p} + \Delta\vec{p}$ leads to

$$\sum_x [I(W(\vec{x}, \vec{p})) + \nabla I J \Delta p - T(\vec{x})]^2, \tag{4.9}$$

where J is the Jacobian of the warp as defined in Equation A.4 and ∇I is the gradient of the image under the actual estimated warp. The equation

$$S = \nabla I J \tag{4.10}$$

will be used as a shortcut and introduced as it is an frequently used quantity, termed the `steepest descent image`. Furthermore, this leads to a very simple expression for the Gauss-Newton approximation to the `Hessian` matrix H:

$$H = \sum_x S^\intercal S. \tag{4.11}$$

With this, the partial derivative of Equation 4.9 can be written as

$$2 \sum_x S^\intercal [I(W(\vec{x}, \vec{p})) + S\Delta p - T(\vec{x})]. \tag{4.12}$$

This leads to the parameter update Δp that minimizes Equation 4.9:

$$\Delta p = H^{-1} \sum_{x} S^{\intercal}[T(\vec{x}) - I(W(\vec{x}, \vec{p}))]. \tag{4.13}$$

With the new estimate

$$p_{\text{new}} = p + \Delta p, \tag{4.14}$$

the next iteration is started. The iteration is stopped, when either the error metric, as defined in Equation 4.8, or the parameter update reaches a predefined threshold ϵ.

Problems in image registration

One drawback of the Lucas-Kanade method is, that the calculated Hessian might not be positive definite at points outside the local minimum, leading to divergent iterations. This issue can be addressed by the introduction of a dampening factor, that is added to the diagonals of the Hessian matrix and that decreases, if the error decreases during one iteration step. Furthermore, the Lucas-Kanade method can get stuck in local minima, especially when registering images with periodic structures. This can be addressed by using the Gaussian pyramid approach, described below. In general, the chance to get stuck in a local minimum can be substantially decreased with an adequate initial guess of the free parameters to be fit, which also increases the convergence speed of the algorithm.

Gaussian pyramid

The image registration algorithm used in this thesis is a multi-resolution approach, that can be used iteratively. In a first step, the image is smoothed using a Gaussian kernel and downsampled by a factor of two. The standard deviation σ of the Gaussian kernel is chosen to be twice the size of the scale factor. This procedure is repeated, so that each subsequent image has half the size and the resolution of its predecessor. The result is often referred to as `Gaussian pyramid`. The whole registration process is initialized on the chosen layer in the Gaussian pyramid and iteratively repeated for each higher layer with the upscaled result of the last step being the initial guess of the next step. This minimizes the optimisation steps in each iteration and ensures, that the whole registration does not get stuck in a local minimum of the error function. The results of each iteration step have to be scaled accordingly before being fed into the next iteration step.

Graphical User Interface

As the selection of the starting parameters and the choice of the correct registration model is essential for the speed and quality of the convergence of the algorithm, a Graphical User Interface (GUI) was developed. Besides giving the user the choice between different registration models and tweaking the free variables for a good starting estimate, the GUI should be used to visualise the fitting iterations and the initial and end difference between the image and the template. An exemplary workflow is visualised in Figure 4.2. The GUI

in this example is initialised with an image and a transformed template, both taken from **scipy.misc**. The error corresponds to the maximal values seen on the histogram and equals ± 1 for the unregistered image with normalised grey scales. To optimise visual presentation, the colour map can be chosen as well as displaying the image or the template only as well as their difference. After choosing the registration model from a dropdown-menu, the free parameters can be tweaked and are applied to the preview in real-time. After starting the fitting procedure, each update step is shown in the preview window and the resulting transform can be copied after the fit is converged. The quality of the end result is shown in Figure 4.2, where the bottom row shows the transformed image after user input and the final converged registration with the corresponding total error in the colourbar.

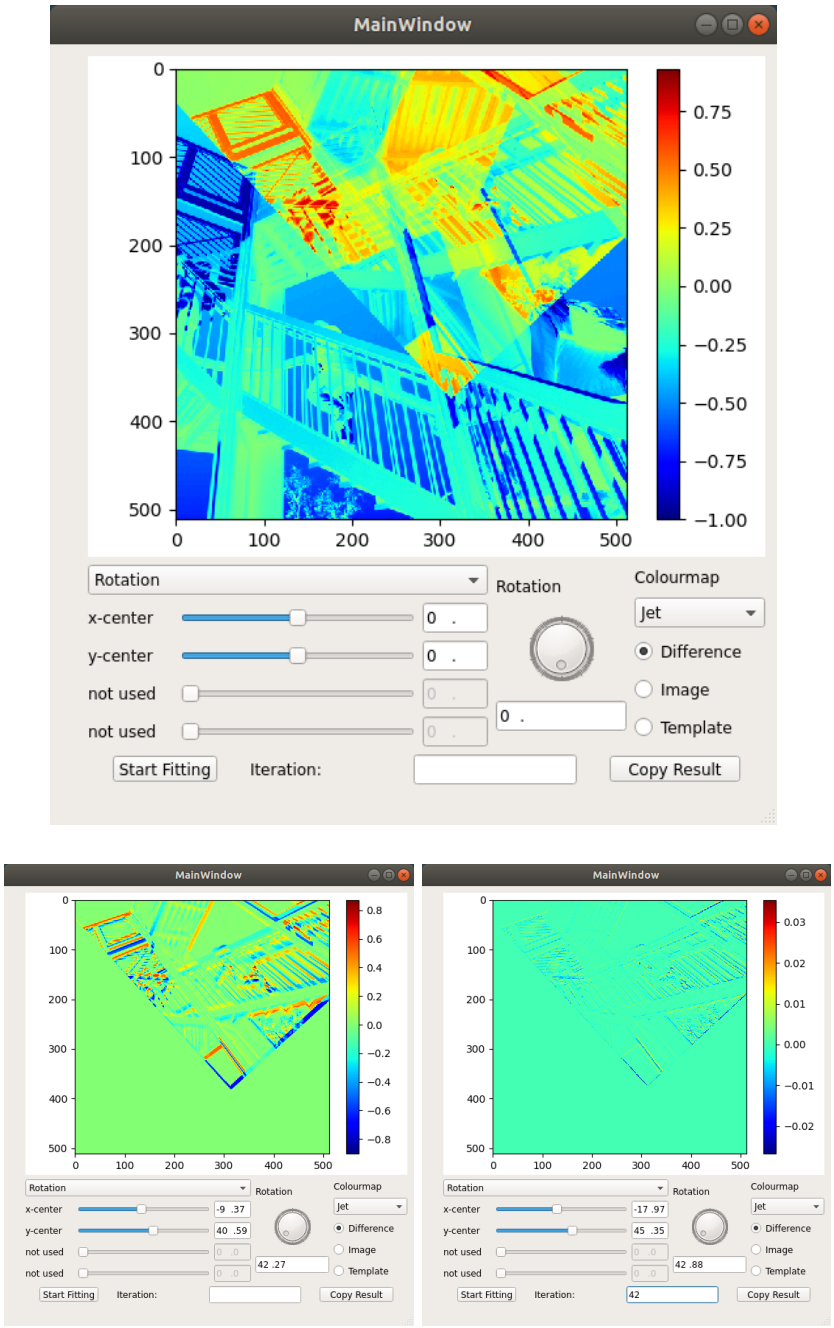

Figure 4.2: The Graphical User Interface (GUI) used for visual feedback and user input to facilitate pre-alignment of image and template. Top: The difference between the image and the randomly rotated and shifted template. Bottom: The pre-alignment done with user-input (left) and the converged registration after 42 iterations (right).

Chapter 5

Implementation

This chapter gives an introduction on the implementation details of the image processing techniques described in this work. It begins with an overview over massive multiprocessing possibilities and discusses the used model in detail. The chapter ends with some specific problems and solutions in multiprocessing environments.

5.1 Compute model

This section will introduce different computing models and mention some core differences before moving to the description of the underlying framework used in this work in section 5.2.

5.1.1 Processing unit

A processing unit is a collection of electronic circuits, that can be programmed to execute calculations, implement algorithms or in general move and manipulate data. Most commonly, the word `processor` refers to the `Central Processing Unit (CPU)`, which is the main logical component of nearly every modern computing device from mobile phone to desktop computer. The `CPU` is a electronic component that consists of different logical compartments, which have different tasks. The different parts of the `CPU` consist of memory modules, different calculation units or more advanced subsystems for sound- or audio-processing. In this work, the word `core` will refer to one logical group, consisting of at least one Arithmetic Logic Unit (ALU) and some kind of memory unit which is connected to this ALU via one or more buses and usually managed via the Memory Management Unit (MMU). Modern `CPUs` most often have multiple cores and a multitude of other processing elements to make all these cores work together. One important element is a global clock, which is needed to synchronise work done by different cores and memory access. This system clock is realised in the form of an oscillating electronic signal that changes periodically between a high and a low state.

5.1.2 Processing speed

The system clock is distributed to each core and used as the base clock of the core. The core clock doesn't have to be identical with the system clock, but can be a fixed or variable multiple. The core clock defines the upper limit of the processing speed of one core and is given in cycles per second. As an example, a recent generation **Core i9 7980XE** `CPU` from Intel has 18 cores with a base core clock of 2.60 GHz, with an option to increase the multiplication factor to achieve a maximum core clock of 4.20 GHz. The execution speed of a program run on one core depends on more variables than just pure clock speed. Some instructions of a program might take more than one cycle, in fact simple things such as the division of two floating point numbers might take as long as 40 cycles, whereas one read from global system memory (Random Access Memory, RAM) can easily cost 100-150 cycles [Agner, 2017],[Levinthal, 2009]. Floating point operations are of such essential importance to program execution, that the speed of big computer systems is compared in Floating Point Operations per Second (FLOPS). Core clock speed is one part of the underlying measures to define the overall processing speed. The other part is circuit design and complexity, which will be discussed in the following section.

5.1.3 Moore's law

The essential building block of an electronic circuit that is capable of storing and manipulating data is the transistor, an electronic component, that can switch a current between two of its terminals depending on a signal on its third terminal. In the 1950s, the first computers were built, that used transistors instead of vacuum tubes, as used before [Cooke-Yarborough, 1998]. As an increasing number of transistors in a circuit allows for a more complex circuit design, it steadily increased and allowed for more powerful computers with a higher processing speed. In 1965, **Gordon E. Moore** predicted, that the number of components in a circuit that can be manufactured at the cost minimum roughly doubles every year [Moore, 1965]. In 1975, this projection was revised and adjusted to project the increase of the complexity to a factor of 2 every two years [Moore, 1975]. This projection, known as **Moore's law** hold true several decades and is stated to have slowed down only until around 2012. As a modern example, the transistor count in the 32-core **AMD Epyc** `CPU`, presented in 2017 was around 2×10^{10}.

5.1.4 Multicore systems

As mentioned above, processing speed is dependent on circuit complexity and core clock speed. Another important factor for the efficiency of a system is the connection between power consumption and processing speed. **Chandrakasan et al.** derived, that the power consumption of an integrated circuit on a microprocessor scales as

$$P = CV^2 f, \tag{5.1}$$

where C is the capacitance of the circuit, while V is the operating voltage and f is the clock speed [Chandrakasan et al., 1995]. In the same paper they show, that the processing speed of a system can be maintained when moving from a

single core to a multi-core design. In the simple example of switching from one to two cores, they show, that for such a system with the constraint of equal data throughput, the capacitance roughly doubles, whereas the voltage and the core clock speed can be roughly halved. This leads to a decrease of power consumption of about 62 % for the whole system. Power consumption is directly connected to heat production and those two factors are an important point especially in portable consumer electronics, which makes multi-core design a favoured choice in many systems.

5.1.5 GPUs

Starting around the 1970s, graphical output for computer systems became more and more popular and increasing complexity of graphical applications such as graphical desktop environments and games defined the needs for dedicated processing units handling graphics. These GPUs are different from CPUs especially in their design and function. Where CPUs are designed to cope with every task from user input to memory handling, GPUs are especially designed to suit the needs in graphics processing, namely massive parallel execution of very simple mathematical functions to update pixels in images or frame buffers. This specialisation in function also comes with specialisations on the hardware level, that allows this simple mathematical functions to be implemented more efficiently than on the CPU. The GPU can be designed as a part of a discrete part, known as graphics card, which also implements memory that can be accessed by the GPU, or as part of a CPU assembly and also as part of the CPU itself. Dedicated modern graphics cards can have core counts of several thousands, with each core running on a core clock of 1 – 2 GHz.

5.2 Heterogeneous computing

A modern computer might have different processing units, organised in different hardware units. For example a modern portable computer usually has a CPU with an integrated GPU and an additional dedicated graphics card with a GPU on it. There are a lot of other processing units, specialised for different tasks, and they can be built in as discrete devices or as part of other processing units. The advantage such a heterogeneous system has over its homogeneous counterpart is, that each different task can be run on the most suitable hardware, leveraging their hardware acceleration feature and therefore being more efficiently run. The challenge of this approach is, that different processing units might be essentially incompatible to each other because of hardware optimizations or specializations that include, but are not limited to

- incompatible bus connections,
- different memory organisation, -layout or -management or
- different performance, power consumption or clock speed.

5.2.1 OpenCL

The Open Computing Language (OpenCL) is a framework for programming the different processing units of heterogeneous computer systems with one

unified programming model. OpenCL was first released in 2008 in version 1.0 by the **Khronos Group** as an open, royalty-free standard[1]. OpenCL defines a set of abstraction layers, that define a general concept. The application of this concept and the realization and transfer to hardware is the responsibility of the hardware manufacturer. In the following sections, the platform- and memory-model of OpenCL will be explained. The advantage of this abstraction layer is, that a programmer can use this concepts on all different hardware implementations without the need to take special care of the variety of underlying circuitry. This section will only introduce the basic concepts needed for the implementations in this work, elaborate information can be found in the public available OpenCL specifications [Khronos Group, 2015].

Platform model

The OpenCL platform model describes the infrastructure of the hardware abstraction layer used. The most important element in the OpenCL platform model is the host. The host is the connection between the external resources of a system, such as memory and user input and the other parts of the OpenCL environment. There is always only one single host in every OpenCL environment. The next element is a *compute device*, often referred to as simply *device*. An OpenCL device does not necessarily have to map to a physical device, but most often this is the case. A device can be one graphics card, one CPU, an Field Programmable Gate Array (FPGA), Digital Signal Processors (DSPs) or others. On each device, there are one or more *compute units*. These can for example be the single cores inside a graphics card or a CPU. In some cases, one compute unit can handle more than one task in parallel, which is taken into account by the OpenCL *processing elements* or *work-items*. Furthermore, several work-items can be organised together in a *work-group*. Figure 5.1 shows one possible realisation of an OpenCL platform with two devices. Each device is managed by the *implementation* or *platform* of the hardware manufacturer or vendor, where it is possible that multiple compatible devices can be managed by the same implementation. The scope of one program is referred to as *context*. It is possible to use several devices, several implementations and combinations of those in one and the same context.

Memory model

Comparable to the platform model, a similar abstraction model exists for different memory spaces. All memory outside the OpenCL implementation, that is accessible only by the host is referred to as *host memory*. Host memory can be realised as hard drive or the *Random Access Memory* (RAM) of the host and therefore be both arbitrarily big in size and slow in access speeds. On the device, there is *device memory*, which is fractioned into four sub-regions *global memory*, *constant memory*, *local memory* and *private memory*. Global memory is a memory region, which is accessible by both the host and the device and is therefore used for memory transfers between host and device and vice versa. Furthermore global memory is both readable and writeable from each

[1] Although the implementations in this work are based on the 2.2 specifications, most of the basic concepts are true for all versions of the standard.

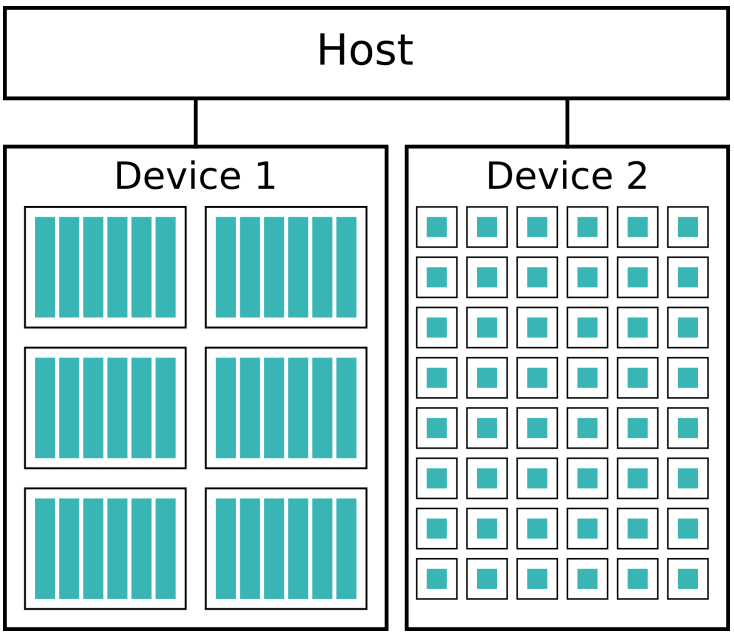

Figure 5.1: Schematic drawing of one possible realisation of an OpenCL environment. One host manages two devices, where Device 1 has six compute units with six processing elements each and Device 2 has 48 compute units with one processing element each.

work-item on all devices in the same context. The constant memory region is a region of the global memory, that is read-only to the work-items and writeable by the host. It is used for memory objects, that are unchanged during the execution of a program, such as the program code itself. Local memory belongs to one work-group and is writeable and readable by all work-items in the group. It is therefore used for the allocation of variables that are shared by all items in a work-group. Each work-item has its own private memory and memory objects in this memory space are not visible to other work-items. Memory management in `OpenCL` is not done implicitly, the user or programmer has to explicitly define which memory object to store in which memory region. As the different regions have differences in access speed in orders of magnitudes, this is a very sensitive choice that reflects in execution performance. In general, the speed increases from global over local to private memory, whereas in the same direction the available memory size decreases.

Memory objects

`OpenCL` implements two essentially different memory objects. *Buffer objects* are contiguous blocks of memory, which can be addressed using pointers. This buffer object is optimized for sequential access, meaning that coalesced access of threads to this memory object are substantially faster than misaligned access patterns. As an example on an **NVIDIA GeForce GTX 8800** graphics card, the transfer speed with an optimal access pattern is $\approx 74\,\mathrm{GB/s}$ whereas with an offset access pattern it is decreased to $\approx 7\,\mathrm{GB/s}$ [Nvidia, 2011]. The situation is

a little different for *image objects*, which are the second type of memory objects in OpenCL. The image object is optimized for the storage and manipulation of digital images as defined in section 4.1. As GPUs are originally designed for graphics processing, they usually posses a dedicated hardware memory region often referred to as *texture memory* or *texture cache* that is the basis of the optimisations which are exposed to the implementation via the OpenCL image object. The most important optimisation of the image object is the caching of memory reads, meaning if a value is read from a pixel coordinate in an image, subsequent reads to the same pixel or pixels in a close 2D neighbourhood are a lot faster. The image object has other optimisations that include automatic bound-checking or coordinate normalisation and unpacking of multi-channel data. A downside of using image objects is, that one single OpenCL kernel can not write and read to the same image object[2].

Execution model

The smallest entity of an OpenCL program is a kernel. A kernel is a set of instructions executed by one single processing element. In a parallel multiprocessing environment, a large number of processing elements can each run its own instance of the same kernel only differing in parameters, data input or private memory. Several kernels make up an OpenCL program. The kernels are compiled by the OpenCL implementation for each device in the context. After that the memory objects are created and send to the processing elements together with the compiled kernels via *command queues*, where they are then executed one after another. If not explicitly changed, a kernel run is only started before the kernel before has finished execution. The OpenCL standard supports the usage of events, that can be used to measure execution timing on the device, which is used in this work as the host only sees the points in time where tasks such as kernel executions or memory transfers are pushed into the queue for scheduling on the device. In some scenarios, it is beneficial to leave the order of tasks to the device, in other scenarios this is impossible due to the need of later kernel executions to access data from earlier kernel executions. This dependencies can also be handled via OpenCL events or OpenCL synchronisation primitives. A schematic diagram of this execution model is shown in Figure 5.2. The kernels shown in this diagram are written in a static subset of the C or C++ programming language. To interface the OpenCL implementation from the host, there exist several *Application Programming Interfaces* (API), in different languages. In this work, the Python binding **pyopenCL** is used [Klöckner et al., 2012].

5.3 Selected problems

5.3.1 Non-locality

A lot of image processing algorithms rely on values of other pixels to adjust or correct the value of one pixel. As an example this is true in the correction of the streak artefacts from high energy particles as shown in Figure 4.1. As

[2]This is something that might be handled different by certain devices and in different OpenCL versions.

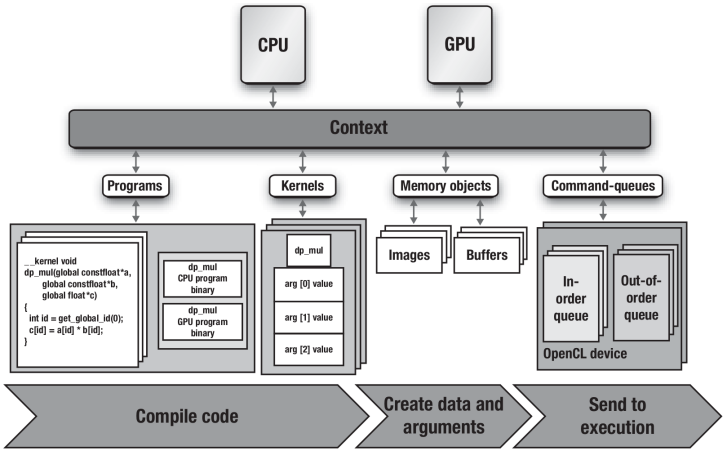

Figure 5.2: A block diagram of OpenCL components and the execution model as seen from the host [Munshi et al., 2012, p.35].

the speed of all implementations in this work is highly due to the parallelism of the underlying platform, an approach where each pixel is handled by the instance of a kernel run on one single processing element is natural. One has no influence on the execution speed of one kernel instance relative to an other and therefore a race-condition exists between pixel reads and updates. In this work, three strategies were used to circumvent this problem, which are shortly outlined in the following. The first strategy is a temporary storage strategy. Each processing element reads the needed pixel values to its private memory, and stores its result in local memory. A subsequent kernel reads this temporary memory chunks and combines them together into global memory. This strategy is possible, if the end result in global memory is a commutative combination of the results in local storage, such as a simple addition, multiplication or averaging. The second strategy is the usage of masks. The dimension of an image is expanded by one or more dimensions that are used to store intermediate values. The first kernel only reads values from the image and marks the pixels in which there is a change to be applied in the mask. A subsequent kernel reads only the masked values and writes back the updated values to the original image. This strategy can be applied, if the application of the first kernel leads to a sparse distribution of pixels in the mask, so that the constraint of non-locality is no longer true for the second kernel, e.g. an algorithm that finds exclusive maxima in a pixel neighbourhood. The downside in using this strategy is, that writes and reads to the same image in one kernel are not always supported and memory usage goes up as an additional image has to be used as source or destination respectively. The third strategy is to use synchronisation primitives offered by `OpenCL`. This strategy is not used in this work as it only allows synchronization between work-items inside the same work-group and not over multiple devices and therefore is a lot harder to scale up.

5.3.2 Iterative mean

When a set of n measurements x_k is given, the empirical mean of the values is simply

$$\bar{x} = \frac{1}{n}\sum_{k=1}^{n} x_k. \tag{5.2}$$

Furthermore, the empirical standard deviation σ is defined[3] via this mean as

$$\sigma = \sqrt{\frac{1}{n}\sum_{k=1}^{n}(x_k - \bar{x})^2}. \tag{5.3}$$

However the calculations of both these equations require an a priori knowledge of all x_k for the calculation. In a setup, where values are continuously arriving, as given in most long exposure imaging applications, an iterative replacement of Equation 5.3 is needed. One possible iterative formulation of the two equations above is

$$\bar{x}_{k+1} = \bar{x}_k + \frac{x_{k+1} - \bar{x}_k}{k+1} \tag{5.4}$$

and

$$\sigma^2_{k+1} = \frac{k \cdot \sigma^2_k + (x_{k+1} - \bar{x}_k)(x_{k+1} - \bar{x}_{k+1})}{k+1} \tag{5.5}$$

respectively. There is a more intricate problem with these two iterative formulas. Especially for a large number of datapoints, the update in each iteration step tends to get relatively small in comparison to the end result. When using simple floating point arithmetics as implemented in most programming environments, this error accumulates quite fast. A formula that circumvents this problem is given in [Knuth, 1997](section 4.2.2 eq. 15 f.):

$$M_1 = x_1 \qquad M_k = M_{k-1} + (x_k - M_{k-1})/k \tag{5.6}$$

$$S_1 = 0 \qquad S_k = S_{k-1} + (x_k - M_{k-1})(x_k - M_k) \tag{5.7}$$

with

$$\sigma_n = \sqrt{S_n/n} \tag{5.8}$$

for $2 \leq k \leq n$. Note, that Equation 5.8 was adapted to conform with Equation 5.3.

5.3.3 Floating point precision

Another possible source of error is floating point precision and its implementation in `OpenCL`. In the compile step of a kernel, some optimisations are applied, that are implementation specific and may vary between hardware vendors. This optimisations can in some rare cases lead to different results in simple mathematical operations that can be optimised at compile time. One of these exampled will be presented here. Assume at some point in a program this code

[3] Note, that there is another definition, using $n-1$ in the normalizing fraction. This is the unbiased estimate of the underlying population, the random samples x_k are drawn from.

```
1 x = 3
2 y = x*x
3 z = sqrt(y)
```

is executed. The value of z after this code block is assumed to be equal to the value of x. However, calculating the square root of any number might lead to numbers that have no exact representation in finite length decimal numbers. Even worse, some decimal numbers have no exact representation in floating point data types. Therefore the above code might lead to numerical errors. A possible compiler optimisation in this case is to take the absolute value of x instead of calculating the square root of a square, which leads to an exact value in cases where x can be represented exactly in the chosen data type. The loss of precision is an intrinsic problem of floating point mathematics and cannot be circumvented in general. The problem that can be circumvented is having different numerical output if the same code is run on different devices. One possible way to achieve this is to completely turn off compiler optimisations which has extensive consequences in performance degradation. The approach in this work was to make sure, that all different computing devices are run under the same implementation and therefore the same compiler can be used for each device. To minimise the errors arising from floating point operations, all calculations on the device are done with double precision wherever possible.

Part II

Applications

Chapter 6

Super Resolution

6.1 Introduction

As described in section 3.3, there seems to be an intrinsic limit in resolution to any optical system, either being the diffraction limit or being the characteristics of single components of the system which are combined in the General Material Transfer Function (GMTF). But this statement does not hold true for all imaging systems. In the early years of the 20th century, fluorescence microscopy has been discovered and further developed. This technique is based on light of a specific wavelength that excites fluorescence and therefore emission of a different wavelength. The resulting image can show structures, which are not resolvable by simple diffraction limited systems. Several other techniques have been developed that find other or more sophisticated ways of circumventing the resolution limit. These techniques are collected under the term super resolution to emphasize, that structure sizes below the classical resolution limit can be resolved. In this work, the main focus is imaging with X-ray and neutron sources, so the application of this super resolution techniques to this imaging modalities is of main interest and will be discussed in this chapter. Before that, the most common imaging techniques in the super resolution domain will be presented together with a discussion of resolution in these applications.

6.1.1 STED

In 2014, the Nobel prize in chemistry was shared by three different scientists for their recent work in the development of super resolution microscopy using stimulated emission: **Stefan Hell**, **W.E. Moerner** and **Eric Betzig**. The method they developed is known under the term STimulated Emission Depletion (STED)-microscopy. The basis for STED is a concept called *REversible Saturable OpticaL Fluorescent Transitions* (RESOLFT). Incident light can not only excite molecules which then relax via fluorescent emission but also stimulate emission itself. An important characteristic of this stimulated emission is, that its wavelength is equal to the incident light. This is not true for fluorescent light and therefore light stemming from those different processes can easily be discriminated using e.g. a beam splitter such as a dichroic mir-

ror. Furthermore, it is important, that the process of excitation and stimulated emission is reversible and can be repeated several times. If a part of the fluorescent states of molecules inside the sample are excited by light from the excitation beam, this process follows the diffraction limit [Hell and Wichmann, 1994]. A second beam (referred to as STED-beam) can now be used to stimulate emission in those molecules. The shape of the STED beam can be chosen to have a minimum in the middle, which leads to a small spot inside the sample, where stimulated emission is not happening. This small spot is still excited and can cause fluorescent emission. The two incident light beams are then rasterised over the whole sample to record the full image. The resulting resolution follows to be

$$\Delta d \geq \frac{\lambda}{2n\sin(\alpha)\sqrt{1+\frac{I}{I_{\text{sat}}}}}, \tag{6.1}$$

where I_{sat} is the saturation intensity at which the fluorescence of a molecule is suppressed with a probability of 0.5 [Hell, 2005]. The approach of **Betzig** is a little different as light with different wavelength is used together with switchable fluorescent molecules but in principle is based on the same idea [Betzig et al., 2006]. An example of the resolution gain from STED over confocal microscopy is illustrated in Figure 6.1.

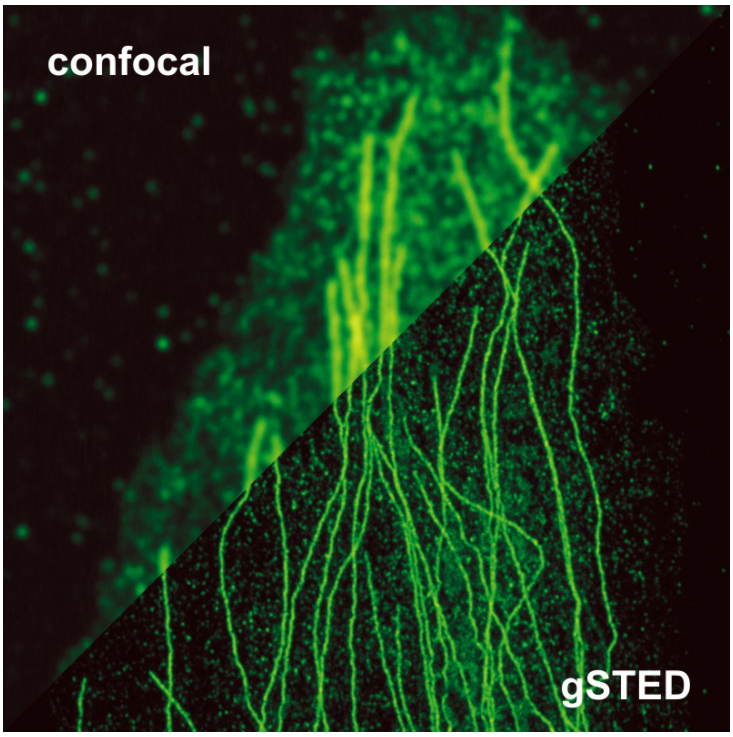

Figure 6.1: Comparison between the resolution of confocal microscopy and gated STED (gSTED) of a tubulin sample. The elongated structures are microtubuli with a diameter of $\approx 20 - 30\,\text{nm}$. Courtesy of PicoQuant [PicoQuant, 2018].

6.1.2 STORM and (F)PALM

The main problem regarding resolution is overlapping of the PSFs from multiple light sources in the object plane. If objects are further away from each other than the distance defined by the resolution criteria above, they can be resolved as single objects. Furthermore, if the PSF of the single light source is known, it's exact position can be reconstructed from the PSF via simple deconvolution or fitting. This essential sparsity of light sources is in STED provided via the scanning approach in the spatial domain. The methods under the terms (Fluorescence) PhotoActivated Localization Microscopy ((F)PALM) and STochastic Optical Reconstruction Microscopy (STORM) make use of the fact, that this sparsity of light sources also can be provided in the temporal domain. If at any given exposure of an image only a small enough subset of fluorescent centres in the object are activated, their PSFs do not overlap in the image plane and therefore their exact position can be fitted with a resolution below the diffraction limit and below the FWHM of the GMTF of the system. If this is repeated several times with different subsets of light sources, a super-resolution image can be calculated simply as an addition of all these subsets. The main difference between STED and STORM/(F)PALM is, that the former is a scanning approach, while in the latter multiple light sources can be captured at once, which is typical for wide-field applications. There is no difference between (F)PALM and STORM in the regard, that both techniques rely on the temporal sparsity of fluorescence events, however the way how this is achieved chemically and structurally is different, which is treated in detail elsewhere [Huang et al., 2008], [Huang et al., 2012], [Knorpp and Templin, 2009], [Rust et al., 2006].

6.1.3 Resolution

In contrast to classical, optical microscopy, the PSF no longer dictates the overall achievable resolution in super resolution techniques but rather the achievable resolution is dependent on the knowledge one has about the PSF and the possibility to reverse its effect on image formation. Therefore, resolution becomes a statistical problem, where the precision depends on signal statistics and the *Signal to Noise Ratio* (SNR) of the imaging system [Passon and Grebe-Ellis, 2016]. Furthermore, for different emitters that are localized via fitting, there might be different fitting precisions due to different signal statistics and the underlying luminescent properties of the sample. This leads to the image formation description as a convolution with a single PSF to hold true no longer. **Ram et al.** have established a stochastic framework to define a Fundamental REsolution Measure (FREM) that is applicable to single molecular imaging and super resolution techniques in general. They give an analytical expression for the FREM, that gives the best-case estimate of achievable localisation precision dependent on the distance d of two point light sources as

$$\delta_d := \frac{1}{\sqrt{4\pi\Lambda_0 \cdot (t - t_0)\Gamma_0(d)}} \cdot \frac{\lambda}{NA}, \tag{6.2}$$

where λ is the wavelength of the photons emitted by the light sources, NA is the numerical aperture Λ_0 is the photon detection rate of one single emitter,

$[t_0, t]$ is the acquisition time interval and $\Gamma_0(d)$ is defined as

$$\Gamma_0(d) := \int_{\mathbb{R}^2} \frac{1}{\frac{J_1^2(\alpha r_{01})}{r_{01}^2} + \frac{J_1^2(\alpha r_{02})}{r_{02}^2}} \left(\left(x + \frac{d}{2} \right) \frac{J_1(\alpha r_{01}) J_2(\alpha r_{01})}{r_{01}^3} - \left(x - \frac{d}{2} \right) \frac{J_1(\alpha r_{02}) J_2(\alpha r_{02})}{r_{02}^3} \right)^2 \mathrm{d}x\mathrm{d}y, \tag{6.3}$$

with J_n denoting the n-th order Bessel function of the first kind and

$$\alpha = \frac{2\pi NA}{\lambda}$$
$$r_{01} = \sqrt{\left(x + \frac{d}{2} \right)^2 + y^2}$$
$$r_{02} = \sqrt{\left(x - \frac{d}{2} \right)^2 + y^2}.$$

This definition is in analogy to the Abbe limit a theoretical limit in absence of noise and therefore a lower limit to the achievable resolution. From this result it is possible to derive an analytical expression for the `Practical REsolution Measure (PREM)`, which takes the pixelsize of pixelated detectors into account as well as additional noise sources. [Ram et al., 2006][Ram et al., 2007]

6.2 Application to particle detection

In a classical particle detection setup, the convolution approach of image formation holds true. Therefore, the resolution is mainly determined by the detection element with the largest `PSF`. As described in the section above, this formalism can be circumvented by `super resolution` techniques. In this section, the applicability of `super resolution` techniques to the case of particle detection with pixelated detectors will be discussed. The discussion will be done for X-ray detection systems, but most results are applicable to neutron detection as well with the exception of intrinsic scintillator resolution.

6.2.1 Boundary conditions

`super resolution` as described above deals with detection of single, fluorescent molecules as emitters. In a particle detection setup, the interaction of the detected particle with the scintillation screen takes the place of the fluorescent molecule. Therefore two constraints can be established. The first constraint is to be able to detect two distinct particle-scintillator interactions, which will be referred to as the constraint of separability. The second and more fundamental constraint is, to actually detect a single particle interaction at all. The best case scenario of the first constraint of separability can be quantified using Equation 6.3. This equation is dependent on the numerical aperture NA, the photon count of the light source, the emitted wavelength λ and the quite complicated

$\Gamma_0(d)$ function. According to **Derenzo et al.** the scintillator with the highest light yield per incident X-ray photon to the time of this writing is LuI_3:Ce with up to 115 000 photons/MeV at an emission wavelength of $\lambda = 522\,\text{nm}$ [Glodo et al., 2008], [Derenzo et al., 2017]. At a typical medical X-ray energy of about 60 keV this leads to a scintillator light yield of 6900 photons per interaction. For these ideal values, Equation 6.3 yields a FREM of $1.02 - 3.33\,\text{nm}$ for distances of the particle-scintillator interactions of $500 - 10\,\text{nm}$. This result confirms, that in theory a separation of particle-scintillator interactions is possible down to a few nanometres. However this result neglects the complex interdependencies between several parameters in a practical setup that will be discussed in the next section.

6.2.2 Parameter dependencies

The discussion of parameter dependencies will be done along the light path from the source towards the detector.

Particle source

The source flux will determine the number of particle-scintillator interactions per time. In a `super resolution` setup, the events have to be separated in the temporal domain or in the spatial domain. The boundary condition in the spatial domain is given by the separability criterion in the section above. The spatial separation is dependant on the time resolution of the scintillator together with the readout speed of the detector. These numbers will together determine the image statistics of the `super resolution` image and therefore have an influence on the acquisition time of the whole system. The spectrum of the source will on the one hand determine the possible imaging applications regarding the penetrable materials and thicknesses. On the other hand the spectrum will have an influence on the scintillator choice, as particles with higher energy require a higher stopping power and therefore either a higher atomic number or a higher scintillator thickness. Furthermore, a higher particle energy leads to a higher light-yield in a particle-scintillator interaction.

Scintillator

As already mentioned the scintillator choice depends on the source in the regards of stopping power. The thickness of the scintillator is limited by the depth-of-field of the optical elements behind the scintillator as defined in Equation 3.14. A thinner scintillator will limit the stopping power and therefore have an influence on the available source spectra as well as the detection efficiency. A thicker scintillator will in general have a lower scintillator resolution and furthermore negatively influence the SNR as out of focus planes in the scintillator add to background noise. The choice of scintillator material furthermore depends on the mechanical characteristics which can limit the lowest achievable thickness and furthermore powder scintillators start to loose scintillation properties when manufactured in very thin layers. Some scintillation materials are hygroscopic, meaning that they need an encasing to ensure their proper function over longer periods. Furthermore the emission wavelength of the scintillator should be in a region where the optics have a high transmittance and

the detector has a high quantum efficiency. In these boundaries the scintillator should have the highest possible light yield per particle-scintillator interaction. With a substrate-mounted scintillator the light yield is optimal, when the refractive index of the scintillator is matched to this of the substrate. In an immersion configuration this should also be close to the refractive index of the immersion liquid.

Optics

The highest light yield is achieved, when the entry-piece of the optics has the largest possible *NA*. Typically high *NA* is only available in high-magnification or immersion objectives. These two factors together with the emission wavelength determine the useful scintillator thickness according to Equation 3.14. The magnification defines the field-of-view of the system together with the pixel-size of the detector. The optics should have the highest possible transmittance in the region where the scintillator has its emission peak to achieve the best possible sensitivity of the whole setup.

Detector

The detector should have the best quantum efficiency in a regime where the scintillator emission is maximal. The pixel-size and numbers of pixels defines the sampling on the detector plane and therefore the usable magnification of the optics and the field of view. Readout speed of the detector is essential for the temporal separation of events and therefore is a limit to count rate, image statistics and overall exposure time. The most important factor is readout noise. This defines the lower limit of single event detectability and furthermore limits the statistical precision and with this has an influence on the `PREM`.

These dependencies show, that the optimisation of a `super resolution` system has to be done in a very complex multidimensional parameter space.

6.3 Light yield

In order to calculate the light from one X-ray photon in the scintillator, that reaches the camera the following calculation is done. All scintillation photons from one interaction are assumed to be irradiated homogeneously on a sphere with the surface of the sphere being

$$A_{\text{sphere}} = 4\pi r^2, \tag{6.4}$$

where r is the radius of the sphere and therefore the distance from the scintillation center. The formula of the surface of a spherical cap is given by

$$A_{\text{sphere,cap}} = 2\pi r h = \pi(a^2 + h^2), \tag{6.5}$$

where a is the radius of the circular ground plane of the spherical cap, h is the height of the spherical cap and r is the radius of the sphere as also shown in Figure 6.2. The spherical cap corresponds to the light emitted by a scintillation

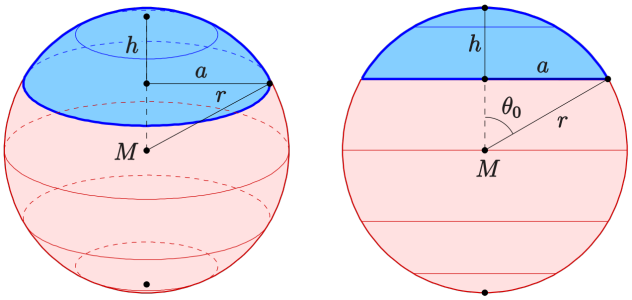

Figure 6.2: Schematic drawing of the variables needed to describe a spherical cap. Illustration by Wikimedia user Ag2gaeh, published under creative commons license BY-SA 4.0 [Wikimedia Commons, 2015].

centre into a cone with opening angle θ_0. With the transformations

$$a = r\sin(\theta_0), h = r(1 - \cos(\theta_0)), \tag{6.6}$$

Equation 6.5 becomes

$$A_{\text{sphere,cap}}(\theta_0) = 2\pi r^2 \cdot (1 - \cos(\theta_0)). \tag{6.7}$$

The percentage of light emitted in this cone relative to the whole sphere is

$$\frac{A_{\text{sphere,cap}}}{A_{\text{sphere}}} = \frac{(1 - cos(\theta_0))}{2}. \tag{6.8}$$

This opening angle of the light cone can be limited by two different boundaries. On the one hand, total reflection on material boundaries can occur, for example between scintillator and substrate material due to their different index of refraction. On the other hand the opening angle can be limited by the numerical aperture and the entrance aperture of the optical system. Both cases involve calculations for optical beam paths using Snell's law:

$$n_1 \sin(\theta_1) = n_2 \sin(\theta_2). \tag{6.9}$$

This law connects the two angles of refraction inside two media with their indices of refraction. In the case of the second angle being perpendicular to the normal of the surface, the incident angle is called critical angle, because all light coming in with larger angles will be completely reflected. The equation for the critical angle becomes

$$\theta_{critical} = \arcsin\left(\frac{n_2}{n_1}\right). \tag{6.10}$$

In all cases regarded for the presented system, the numerical aperture is a stricter limit than the critical angle. The numerical aperture NA is defined with the index of refraction n of the medium in which the optical system is working and its maximum possible opening angle θ_{opening} to be

$$NA = n\sin(\theta_{\text{opening}}). \tag{6.11}$$

Inversely, an optical system, working in air, with a given NA accepts light in a maximum opening angle of

$$\theta_{\text{opening}} = \arcsin(NA). \tag{6.12}$$

This can be translated to an opening angle in the scintillation material by application of Equation 6.9. Depending on the exact composition of the scintillator, it is possible to have different materials in the optical beam path and Equation 6.9 has to be applied multiple times. As the scintillator in the presented case was produced on a substrate and the scintillator could be placed with the substrate towards source or detector, this two cases were treated differently. The calculation is shown exemplary for the latter case. The angle $\theta_{\text{substrate}}$ inside the substrate can be calculated as [1]

$$\theta_{\text{substrate}} = \arcsin\left(\frac{NA}{n_{\text{substrate}}}\right). \tag{6.13}$$

In this case, the visible opening angle inside the scintillator can be calculated with

$$\theta_{\text{scintillator}} = \arcsin\left[\sin\left(\theta_{\text{substrate}} \cdot \frac{n_{\text{substrate}}}{n_{\text{scintillator}}}\right)\right]. \tag{6.14}$$

Putting this angle into Equation 6.8, one can calculate the percentage of light that can be captured from an isotropic emitting scintillator with an objective with given NA.

If light traverses a boundary interface between two media with different indices of refraction, there can also be a loss of light due to reflection. After the Fresnel equations, the strength of reflection depends on the angle and polarization of the incident wave and two cases for s-polarization and p-polarization are distinguished. The respective reflectance is given as

$$R_s = \left[\frac{n_1\cos(\theta) - n_2\sqrt{1-\left(\frac{n_1}{n_2}\sin(\theta)\right)^2}}{n_1\cos(\theta) + n_2\sqrt{1-\left(\frac{n_1}{n_2}\sin(\theta)\right)^2}}\right]^2 \tag{6.15}$$

and

$$R_p = \left[\frac{-n_2\cos(\theta) + n_1\sqrt{1-\left(\frac{n_1}{n_2}\sin(\theta)\right)^2}}{n_2\cos(\theta) + n_1\sqrt{1-\left(\frac{n_1}{n_2}\sin(\theta)\right)^2}}\right]^2 \tag{6.16}$$

and for unpolarized light the effective reflectance is the average of these two. To account for the reflectance for rays under different angles, first an array of equidistant angles is calculated. For each ray in this array, a ray-tracing calculation of refraction and reflection at each interface is done iteratively. The resulting reflection coefficients for each ray are averaged to yield an effective reflection coefficient for the complete beam profile.

[1] This is not true for immersion optics, as the index of refraction of the immersion medium is neglected in this formula.

6.3.1 Detector plane

With the results from the above section, an estimation for the amount of light that reaches the scintillator is given. In most cases, where the PSF has to be fitted in order to achieve super resolution, the PSF can be approximated as a Gaussian function without loosing fitting precision significantly [Quirin et al., 2012] [Stallinga and Rieger, 2010]. Its shape can then be described via the two-dimensional Gauss-function

$$G(x,y) = A \cdot \exp\left(-\left(\frac{(x-x_0)^2}{2\sigma_\mathrm{x}^2} + \frac{(y-y_0)^2}{2\sigma_\mathrm{y}^2}\right)\right), \tag{6.17}$$

where A is the amplitude, x_0 and y_0 are the coordinates of the center and the σ are the standard deviations in each direction. The indefinite integral over the whole plane can be evaluated to be

$$\int_{-\infty}^{\infty}\int_{-\infty}^{\infty} G(x,y)\,dx\,dy = 2\pi A\sigma_\mathrm{x}\sigma_\mathrm{y}, \tag{6.18}$$

which corresponds to the total number of recorded photons. To determine the values for the free parameters in Equation 6.17, the values for σ can be calculated. If a Gaussian function is taken into account, the FWHM and the standard deviation are connected via

$$FWHM = 2 \cdot \sqrt{2\ln 2}\,\sigma. \tag{6.19}$$

When determining the resolution of an optical system, the PSF can be taken as a limiting factor. The PSF defines the spread of a point source through an optical system. Objects with a distance lower than the FWHM of the PSF can not be optically separated because of their overlapping PSFs. In reverse, if the PSF is known and estimated to be in the shape of a Gaussian function, the resolution of a setup is equally connected to the σ of Equation 6.17. **Koch et al.** defined an equation for the resolution R of an optical system, where a microscope with an numerical aperture NA is looking onto a scintillation plane with the thickness z to be

$$R = \sqrt{\left(\frac{p}{NA}\right)^2 + (qzNA)^2}, \tag{6.20}$$

where the parameters p and q are found via fitting of numerically simulated resolution curves and in the case of the FWHM are $p = 0.18\,\mu\mathrm{m}$ and $q = 0.075$ [Koch et al., 1998]. The calculated parameters can then be used to model the signal on the detector plane. To calculate the amount of light each pixel on the detector plane sees, the signal has to be integrated over the area of a pixel. The integration of a two-dimensional Gaussian function over rectangular areas is non-trivial and has to be done numerical. For this task, a python implementation of the 7th degree Stoud formula $C_2 : 7-3$ was used [Stoud, 1971]. A short overview of this principle is given in section A.1. The results of this calculation are included in Table 6.1. An important relation is as following:

The expected number of counts inside a region of $\pm x\mu$ around the mean value of a Gaussian function can be calculated as

$$\mathrm{erf}(\frac{x}{\sqrt{2}}), \tag{6.21}$$

with erf being the error function, defined as

$$\mathrm{erf}(x) = \frac{2}{\sqrt{\pi}} \int_0^x \exp(-t^2)\, dt. \tag{6.22}$$

If the standard deviation is known in terms of the pixel size, one can therefore calculate the needed area on the detector to capture a certain fraction of incident photons.

6.3.2 Best case scenario

The calculation of the highest possible light yield is done with the aforementioned LuI_3:Ce scintillator at X-ray energies of 60 kV. This corresponds to an initial light production of 6900 photons. As the index of refraction is not yet consistently documented in literature, it was set to $n_{\mathrm{Scintillator}} = 1.84$ and used with the same substrate as in the real application example mentioned below with $n_{\mathrm{Substrate}} = 1.45$. The results of this calculation are given in Table 6.1.

Table 6.1: Light collection efficiency for the different objectives. Listed are the objective ID as in Table 6.2, values for the maximal capturing angle at the objective entrance α_{entry}, the corresponding opening angle in the scintillator material α_{scin}, the transmission T with Fresnel reflection and the total capture ratio for all effects combined. Using the scintillator yield, the numbers of photons, that can be captured per one 60 kV gamma are calculated for an ideal case as described in subsection 6.3.2 and for a real example as described in the following sections. Additionally the calculated standard deviation σ as mentioned in subsection 6.3.1 is given. For objective 5 the light yield is calculated in immersion oil with $n = 1.515$.

ID	α_{entry} (°)	α_{scin} (°)	T(%)	Capture ratio (%)	N_{ideal}	N_{real}	σ (pixel)
1	14.48	7.81	95.27	0.44	31	3	0.205
2	26.74	14.16	95.24	1.45	100	11 ± 1	0.342
3	48.59	24.05	94.88	4.12	285	31 ± 1	0.931
4	64.16	29.28	93.82	5.99	414	45 ± 1	1.096
5	59.10	44.95	97.44	14.24	983	107 ± 3	1.560

6.3.3 Practical scenario

According to the aforementioned boundary conditions, the parts of the system were chosen as following. As an X-ray source, the **MCBM 65B-50 Mo** from

Table 6.2: A list of the used objectives together with their most important characteristics: Magnification M, numerical aperture NA, working distance wd and depth of field d_{tot}, which is calculated according to Equation 3.14 for a wavelength of 545 nm and a pixel size of 16 µm

ID	M	NA	wd (mm)	d_{tot} (μm)	Manufacturer
1	10	0.25	4.4	15.12	Carl Zeiss
2	20	0.45	0.51	4.47	Carl Zeiss
3	40	0.75	0.66	1.50	Nikon
4	40	0.90	0.30	1.12	Nikon
5	40	1.30	0.2	0.95	Olympus

RTW with a peak voltage of $U_{\text{Peak}} = 65\,\text{kVp}$ and a molybdenum target was chosen. To match the effective energy, as mentioned in the following section, and the focal depth of the desired microscope objective a LuAg:Ce screen from **CRYTUR** with a thickness of $d = 15\,\mu\text{m}$ on a quartz substrate with $d = 170\,\mu\text{m}$ was chosen. The light yield of this scintillator is reported to be up to 12 500 photons/MeV [Mares et al., 2004] which gives a light production of 750 photons per 60 kV gamma. Furthermore, this scintillator has a high stopping power and can be produced with the desired thickness to fit into the focal depth of a wide range of microscope objectives. The detection system is a **Andor iXon Ultra** EMCCD with a very high frame-rate at a very low readout noise. The calculation of light yield was done for each objective through all layers in the scintillator-substrate complex for both possible directions. As the forward case, with the scintillator layer being closer to the detector than the substrate layer, shows a better light yield, the forward case is chosen for the setup and the calculated values are shown in Table 6.1. For completeness, the results of the calculations for the reverse case can be found in section A.2. The results from this calculations will be further decreased by the effects of a polychromatic spectrum as mentioned below.

Mean energy

As the experiments with X-ray radiation in this work were all done at laboratory X-ray sources, the underlying spectrum is always a broad, polychromatic spectrum showing both characteristic peaks at the anode material X-ray emission lines and a broad bremsstrahlung spectrum. In order to facilitate calculations, the mean energy of the spectrum was defined. If a distribution of values is sorted into bins, with the centres of the bins being the values x_i and their corresponding frequency of occurrence is y_i, a simple weighted mean can be calculated to be

$$\text{mean}_i = \frac{\sum_i (x_i \cdot y_i)}{\sum_i y_i}. \tag{6.23}$$

In order to calculate the mean energy of the spectrum in use, the spectrum was measured with an **Amptek XD-123** X-ray spectrometer. The spectrometer

was placed at the position of the scintillator screen and the spectrum of the tube running at the maximum voltage of $U_{\text{peak}} = 65\,\text{kVp}$ and the minimum current of $A = 0.5\,\mu\text{A}$ was measured for five minutes. The resulting measurement is given in counts over detector bins. This measurement was calibrated linearly with the two characteristic peaks of molybdenum at 17.4 keV and 19.6 keV and verified with the small fluorescent peak of the detector at 25 keV. The signal, plotted in Figure 6.3, shows, that the detector is prone to pile-up in the high energy bins above 65 keV. All values above that peak tube voltage were neglected for the calculation, which results in a mean energy of $E_{\text{mean}} = 15.2\,\text{keV}$.

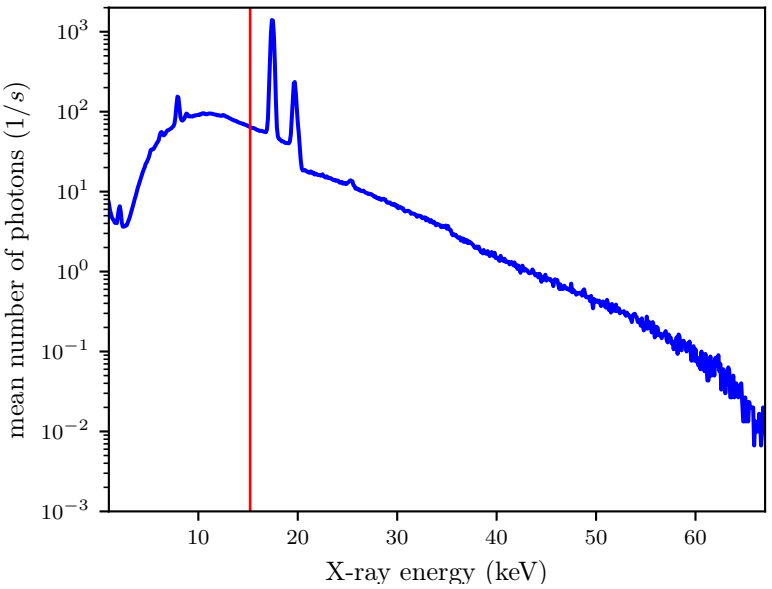

Figure 6.3: Spectrum of the molybdenum X-ray tube at 65 keV. The vertical red line marks the mean value of 15.2 keV.

Energy dependent light yield

The mean energy of the spectrum as defined and calculated in section 6.3.3 is given to 15.2 keV. According to the measurements of [Chewpraditkul et al., 2009], the scintillator light yield does depend non-linearly on the incident radiation and at the mean energy is 75 % of the photon yield of LuAG:Ce at the 662 keV photo-peak. This results in a light production of 143 photons per interaction at the effective energy of the system and a total count of 20 captured photons for the objective with the highest capture ratio.

6.4 Calculated pixel counts

To get the estimated photon count each detector pixel sees, the PSF on the detector plane is integrated over the area of the underlying detector pixels. Depending on where the center of the PSF is placed relative to the pixel matrix, the light spread to the neighbouring pixels is different. In an ideal case, the PSF is exactly centred over one pixel, and the light spreads evenly onto its nearest neighbours. In a worst case scenario, the peak of the PSF is exactly in the point where the corners of four adjacent pixels meet. All positions of the PSF relative to one single pixels are situated between those two extreme border cases, which were representatively chosen because of their inherent symmetries. The resulting integration areas for the calculation are shown in Figure 6.4 and the resulting pixel counts for three selected cases are shown in Figure 6.5.

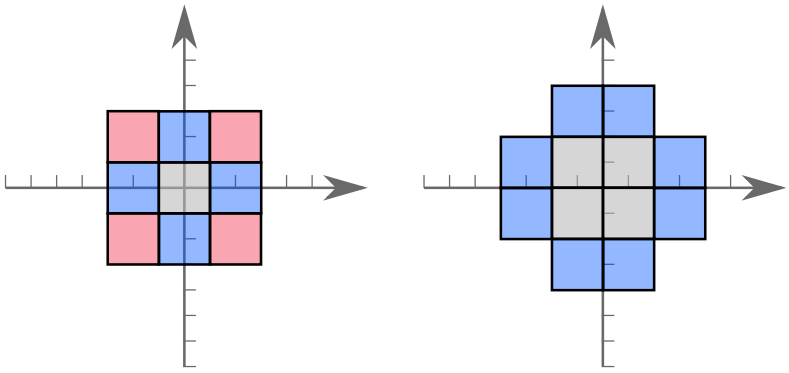

Figure 6.4: Placement of integration areas for the PSF in a best case scenario a) and a worst case scenario b). The ticks on the axis are 0.5 in arbitrary units, so that each pixel has one unit area. The grey pixels are the central pixels, the blue pixels the edge pixels and the red pixels the corner pixels. Note that figure b) has four central pixels. In both cases, the PSF is centred over the origin.

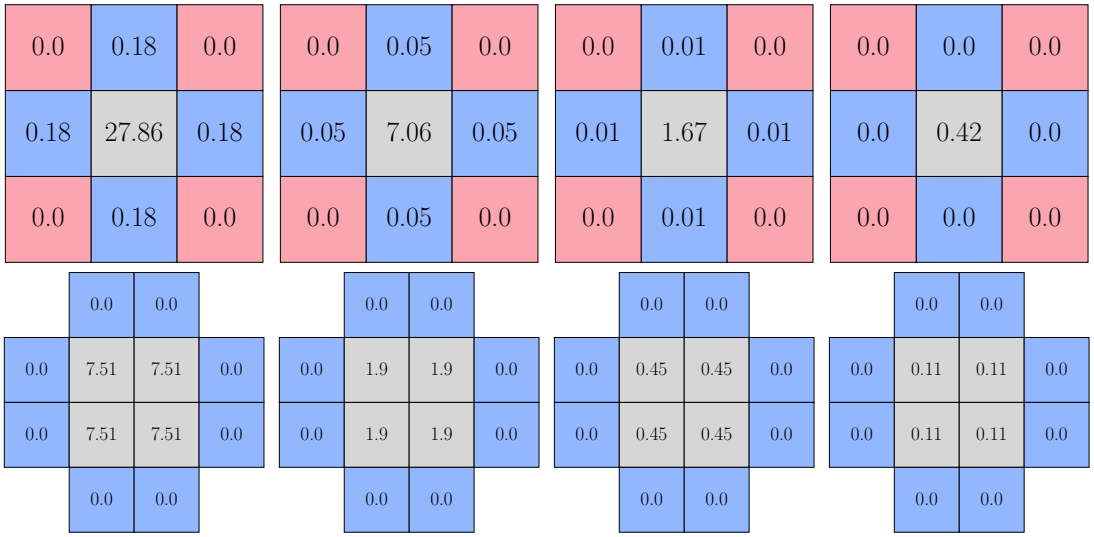

a) Objective 1

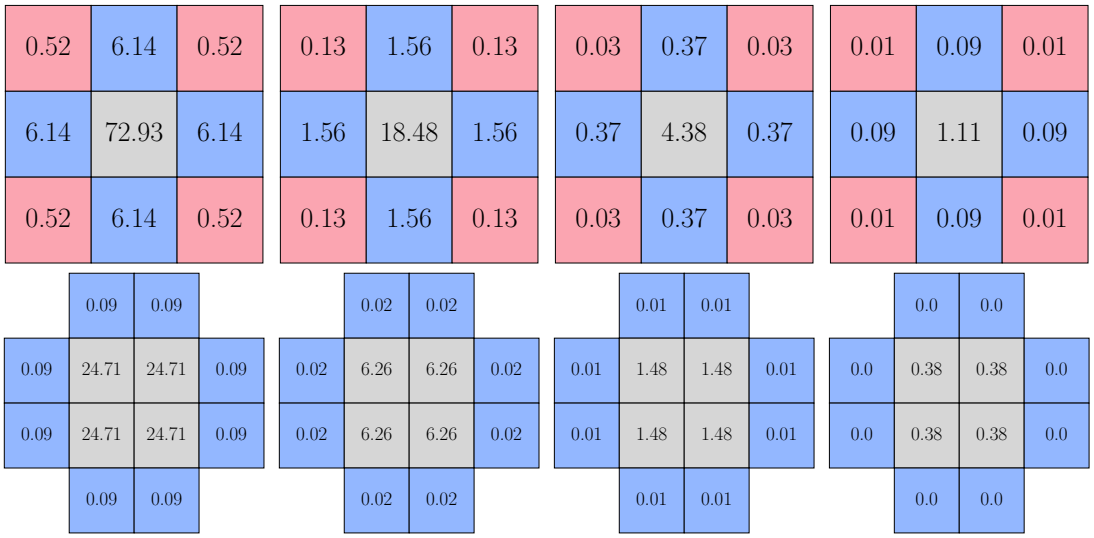

b) Objective 2

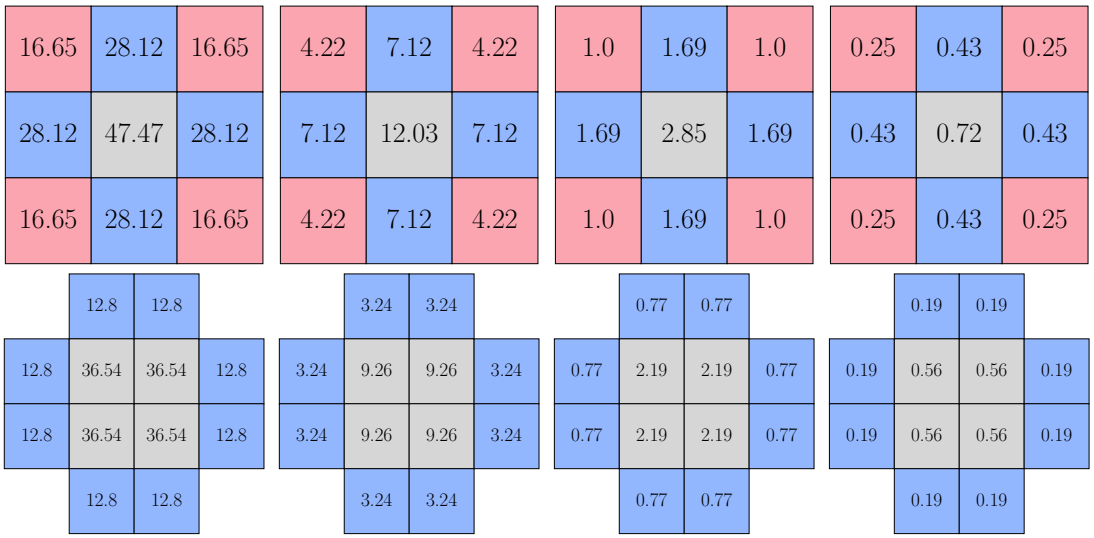

c) Objective 3

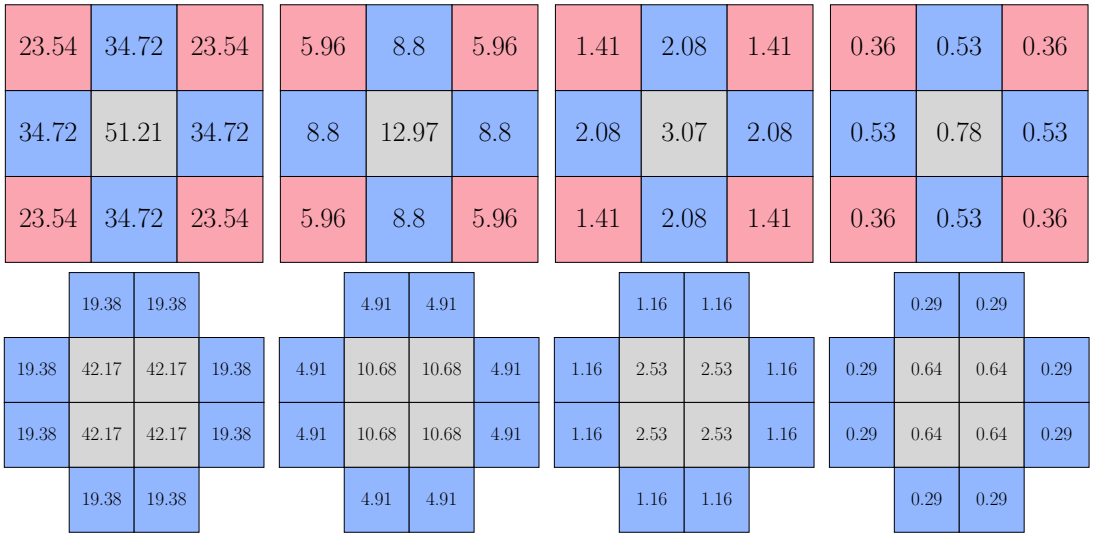

d) Objective 4

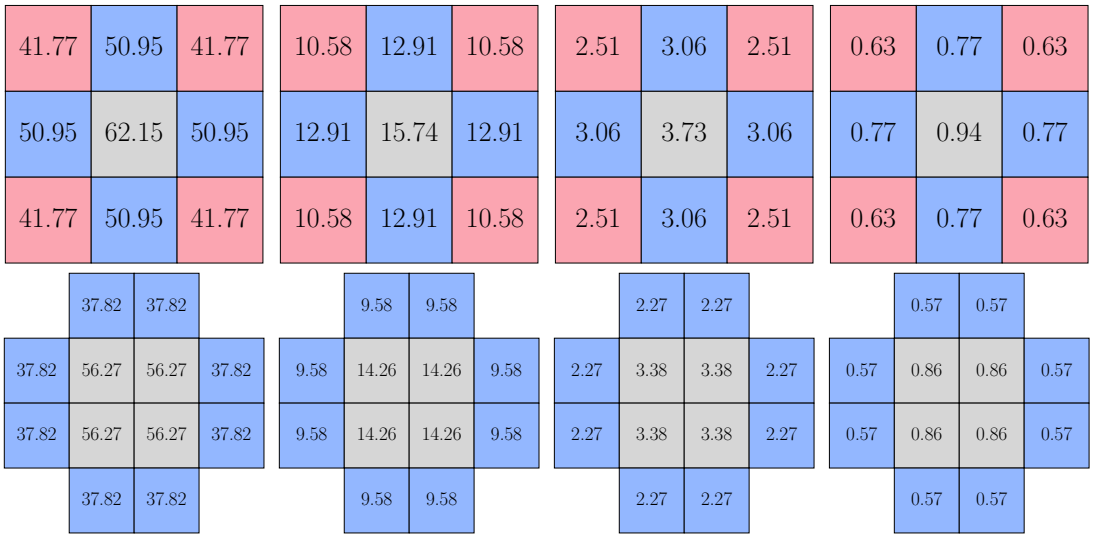

e) Objective 5

Figure 6.5: The numerical results of integrating a PSF according to the two scenarios described in Figure 6.4, rounded to two decimals. Each subfigure corresponds to one objective, where the top row gives the best and the bottom row the worst case scenario. The first and second columns give the values for the LuI_3:Ce scintillator at a wavelength of 545 nm at 60 kV (first column) and the effective energy of 15.2 kV (second column). The third and last column give the values for LuAg:Ce at a wavelength of 545 nm and a energy of 60 kV (third column) and the effective energy of 15.2 kV (last column).

6.5 Results and discussion

From the simulated detector counts, it is evident, that in the case of a real setup at the effective energy the expected photon count is around 1 even with the highest *NA* immersion objective. Even with an assumed quantum efficiency of 1 and no further loss of light inside the optical system, this is below the detection limit of the detector in use, as can be seen in the column for CCD sensitivity in Table 4.1. In the case of the LuAg:Ce scintillator at X-ray energies of 60 keV (third column of Figure 6.5), the signal is detectable with the conventional amplifier in terms of sensitivity, but the single pixel noise is too high to discriminate the signal over the noise. The overall pixel count in the LuI_3:Ce scintillator is overall higher. At the mean energy of 15.2 kV, some objectives lead to photon counts over the detection limit, which can be seen in the second column of Figure 6.5. With objective 1, the expected photon counts are right below the detection level and starting with objective 2, the central pixel has photon counts right above the detection level. However, this is not enough to calculate the centroid of the `PSF` needed for `super resolution`. With the other objectives, more pixels show expected photon counts above the detection limit but another problem arises. A simple estimation of the expected fitting precision can be given by the ability to discriminate between the best and the worst case scenario of pixel counts. Even this coarse discrimination is not given, as the differences of expected pixel counts between worst and best case scenario lie inside the readout noise for the conventional amplifier and inside the sensitivity for the EM amplifier and therefore cannot be resolved. The pixel count for the theoretical case of the LuI_3:Ce at X-ray energies of 60 keV (Figure 6.5 leftmost column) is high enough to be detected even with the EM amplifier and therefore readout noise can be neglected as the gain of the EM-CCD can be used. Furthermore, the dynamic range in the difference between the worst and the best case scenario look promising to allow for a discrimination of these cases which is the precondition for the fitting step for resolution. This leaves two possible approaches to enable `STORM super resolution` with thin films and pixelated detectors. The first approach is going to scintillators with higher light yields. The theoretical light output of LuI_3:Ce is high enough to match the detectability criteria. To the time of the writing of this work, this scintillator was not yet commercially available and the academically produced samples do not yet match the high criteria of high resolution imaging thin film screens especially when it comes to producing the needed very low thicknesses. The other approach is going to higher energies of the incident radiation as this increases the light yield. Increasing the energy of a setup is not trivial, as the stopping power of the scintillator decreases with increasing energy. As an example, the absorption coefficient of LuI_3:Ce at an X-ray energy of 60 keV is approximately $\mu = 3543\,\mathrm{m}^{-1}$. With the Lambert-Beer law

$$I_0 = I_d \cdot e^{-\mu d}, \tag{6.24}$$

where I_0 is the intensity of the incident radiation, I_d is the intensity of radiation after travelling through a material with the thickness of d and an absorption coefficient of μ, the amount of radiation that is captured by a scintillation, and therefore available to produce scintillation light, can be calculated as the

difference

$$1 - e^{-\mu d}. \tag{6.25}$$

For the exemplary case, this leads to an attenuation of the incident radiation of approximately 5.18 %.

Imaging speed

So far, the pixel count based on one single interaction of an X-ray photon with the scintillator has been discussed. A very big challenge is the readout speed of a STORM system. The highest density of events that can be registered is given by the extend of the PSF on the detection plane and therefore is dependent on the numerical aperture of the microscope objective. The separation of events in the same image has to be larger than the FWHM of the underlying PSF and therefore even in the low NA cases not more than one event per array of 3 pixels in each dimension can be captured. To get a super resolution image with half the effective pixel size in each dimension, this leads to a fourfold increase of sub-pixel count and in this example to 36 sub-pixels that can capture at most one event per image. In the discussed application, the camera can record 59 images in one second, which is referred to as the frame-rate. This means, that in this example a maximum of approximately 1.64 events per second per sub-pixel can be captured, which results in an acquisition time of approximately 156 seconds for an image with a dynamic range of 8 bits. This is a very low capture rate even in comparison to intrinsically low-flux applications as neutron imaging.

In neutron imaging, the same problem exist, but will be described from the source perspective: The ANTARES beam-line described in chapter 7 has a capture ratio of approximately 1 neutron per second and square micron. With a pixel size of 16 µm and a super resolution with half the physical pixel size in each dimension, the virtual pixels would have an area of 64 µm^2, corresponding to approximately 64 counts per second. For a dynamic range of 8 bits, the needed 256 counts in this setup could be collected in 4 seconds. To be able to discriminate these events in the temporal domain and to be able to do the super resolution fits, not more than one event is allowed to be captured on a sub-area comprising three by three pixels. With the aforementioned factor-two super resolution, the needed frame-rate f of a camera is the number of events per second times the pixel area times the number of super resolution sub-pixels and in this case equals to

$$f = \frac{64}{s} * (3 * 3) * 4 = 2304 fps. \tag{6.26}$$

The frame-rate of the cameras used in this work is way below this limit when imaging the full sensor without binning. The possibility to go to higher frame-rates is given when going to smaller FOVs. This means, that the needed frame-rates have to be traded against the achievable FOV which essentially makes the STORM approach only possible in scanning mode, with additional overhead. The needed frame-rate also is an estimate of frames to be taken per super resolution projection per second. In the example mentioned above, one projection with a dynamic range of 8 bits would result in over 9000 frames as

raw material for one super resolution image. For an image with a region of interest in the size of 1024x1024 pixels, the resulting uncompressed raw data would amount to approximately 9 GB.

All the above considerations show, that unless a way is found to increase the light yield about one to two orders of magnitude, the STORM approach to super resolution with thin film screens and pixelated detectors is unfeasible. However, recently two other approaches to achieve super resolution in X-ray imaging have been investigated, which will be shortly discussed in the next section.

6.6 Outlook

The problem of the detection of very low light levels is well suited for single-photon counting and charge-integrating hybrid detectors. In these detector type, the incident X-rays are directly converted to a charge cloud, which can then be electronically read out. Incident X-ray photons produce numerous electron-hole pairs in a layer of silicon which are accelerated towards the readout by the application of an electric field. This process is prone to diffusion and results in the distribution of the readout signal over the pixels in the neighbourhood of the pixel that experienced the primary interaction, which is known under the term *charge sharing*. This charge sharing process can be exploited to calculate the interaction point of the incident particle with sub-pixel precision, which has been demonstrated by **Cartier et al.** However, this approach suffers from a low field of view as well as even lower capture speeds in comparison to the EMCCD approach that result in an exposure time of approximately 1440 seconds for a super-resolution image with a virtual pixel size of 1 micron and the aforementioned dynamic range of 8 bits [Cartier et al., 2016].

As mentioned above, another possibility to reduce the PSF is by using STED. **Alekhin et al.** have recently shown a proof of concept, that STED can also be used on an X-ray scintillator in order to achieve super resolution together with thin film X-ray imaging [Alekhin et al., 2017]. In principle, the STED beam was used to deactivate an X-ray scintillator everywhere but in a small active region inside the minimum of the STED beam. Effectively this limits the PSF of the X-ray interaction in the scintillator to this active area. However, this is a scanning approach, which is inherently different to the other described approaches, being full-field techniques.

As a conclusion, the principles of super resolution techniques can be transferred into X-ray imaging and will enable new imaging applications such as G2-less grating interferometry in the near future. The main challenges are the readout speed and light collection efficiencies which are intrinsic in the STORM and STED case and subject to technical development in the case of super resolution imaging with charge-integrating hybrid detectors.

Chapter 7

Neutron Radiographies

In this chapter, the setup for neutron radiographies used for this work will be introduced. Some image processing techniques will be introduced and shown along with examples.

7.1 Setup

All neutron imaging experiments in this work were done at the Heinz Maier-Leibnitz Zentrum (MLZ) in Garching, Germany either at the advanced neutron tomography and radiography experimental system **ANTARES** or the **NECTAR** facility inside the research neutron source facility **Forschungs-Neutronenquelle Heinz Maier-Leibnitz (FRM II)**. The neutron source itself is a nuclear fission reactor running on one single nuclear fuel element which runs on an average power of 20 MW in cycles of a maximum of 60 days. Besides the fuel element and the moderator tank, the reactor pool holds several secondary sources that can be used to convert the neutrons from the hadronic cascade either to neutrons with different energies or positrons. A schematic drawing of the reactor is shown in Figure 2.1. The experiments are placed at the end of the neutron beam guides and work with different secondary sources.

7.1.1 ANTARES

Neutron source

The experiment ANTARES is supplied with cold neutrons from a secondary neutron source with a 20 l tank of deuterium with a temperature of about 25 K [Calzada et al., 2009]. The cold neutrons are fed into the first chamber of the hutch of the experiment via neutron beam guides. The first chamber holds space for beam- and spectrum shaping devices, amongst them being a mechanical velocity selector, a double crystal monochromator or interference gratings for grating based phase contrast imaging [Schulz and Schillinger, 2015]. An additional pinhole allows for different spot sizes and thus corresponds to a difference in the flux at the sample positions. The largest pinhole corresponds to an $L/D = 200$, where L is the detector-source distance and D is the source size, with a resulting neutron flux of $4 \times 10^8 \, \frac{\mathrm{n}}{\mathrm{cm^2 s}}$.

Sample stage

The ANTARES experiment has two distinct measuring chambers, situated one behind the other in the direction of the travelling beam. The difference is, that in the rear chamber, the beam divergence leads to a bigger usable field of view. All experiments in this work have been done in the front chamber, as indicated in Figure 7.1. The sample stage itself is an XY-Phi-table with a travel range of $x = 800\,\text{mm}$, $y = 600\,\text{mm}$ and an additional 360° rotation axis for tomographies, that can carry a sample weight of up to 500 kg.

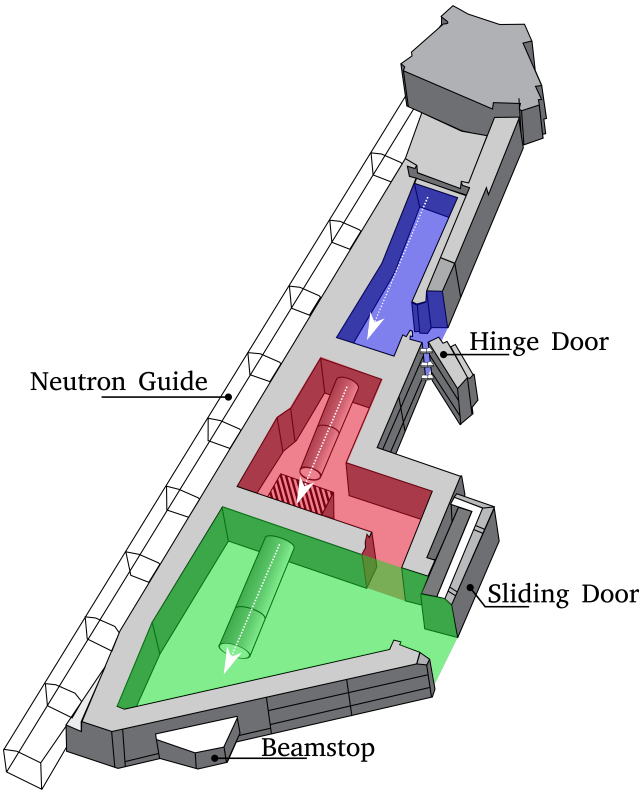

Figure 7.1: Schematic drawing of the ANTARES experiment inside FRM II. The blue area marks the beam shaping chamber, red and green mark measuring chambers 1 and 2. The hatched area in chamber 1 marks the position of the sample stage, approximately 8 m away from the beam entry into the hutch. The beam direction is shown with the white, dotted arrows. Adapted from [Calzada et al., 2009].

Detector system

The detection system of ANTARES is a modular system consisting of a camera box with an entry window that can be fitted with different scintillation screens. A neutron beam is able to dope semiconductors and therefore of doing irreversible damage to semiconductor devices such as (EM)CCD cameras. Therefore, the camera box is fitted with a mirror system, to be able to place

the camera outside the primary beam. The camera box itself is encased with borated polyethylene and can be filled with lead blocks to further shield the camera from neutrons and secondary high energy particles.

7.1.2 NECTAR

The NECTAR setup is identical in its working principle as a neutron radiography and -tomography setup. The main difference to the ANTARES setup is the installation at a different neutron source and therefore a different spectrum. The neutron beam port **SR10** at which NECTAR is placed allows for the use of two different spectra, a fission neutron spectrum with a mean energy of 1.9 MeV and, by changing the assembly in front of the entrance window of the beam tube, a thermal neutron beam option [Mühlbauer et al., 2017].

7.2 Fuel-cell radiographies

As neutrons have a relative low interaction cross-section with metal in comparison to water, the investigation of water management in fuel-cells is a suitable application. In the next sections the investigated fuel-cell will shortly be introduced and the resulting neutron radiographies will be presented and discussed. Partial results of the work presented in this section have been published in [Breitwieser et al., 2016] and parts of the following subsections are adapted from this article.

7.2.1 PEMFC

A fuel-cell is a device to convert chemical energy into electrical energy. The

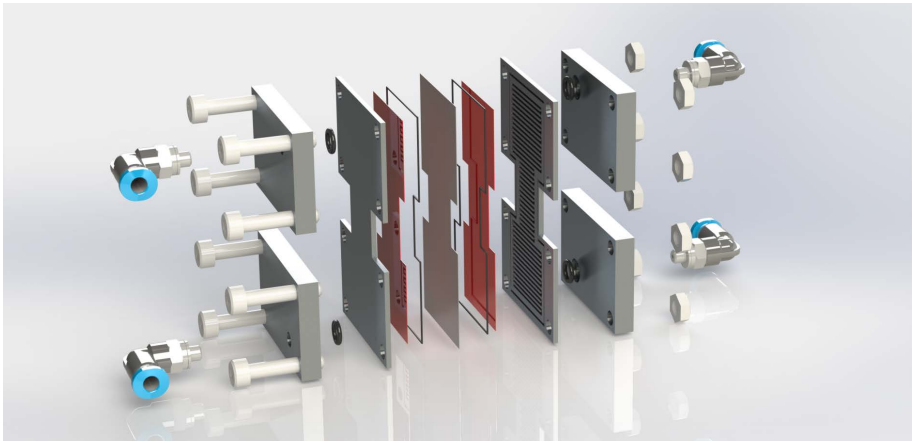

Figure 7.2: Schematic explosion drawing of the prototype of the PEMFC used in this work. The MEA is shown in the middle together with the gas diffusion layers, contacting plates with embedded flow-channels as well as the outer assembly for mounting and connection.

fuel-cell used in this work is a `Proton Exchange Membrane Fuel Cell (PEMFC)` which is also known under the terms *Polymer Electrolyte* - or *Solid*

Polymer Fuel Cell. A PEMFC gains its name from the polymer membrane in the middle of the cell, which usually has thicknesses of 50 – 200 µm. On both sides of this membrane, a catalyst layer is added to enable the chemical reaction of the two reactants, in this case oxygen and hydrogen to water and electricity. The catalyst layer is coated with a micro-porous layer and a gas diffusion layer to facilitate the distribution of the reactants over the whole surface of the active layer. This assembly is referred to as Membrane Electrode Assembly (MEA). On the outside, this MEA is contacted with conducting current collectors, which at the same time act as gas distributors via embedded flow-channels. A schematic drawing of the PEMFC used in this work is shown in Figure 7.2.

At the anode side of a PEMFC, hydrogen is split into single protons and electrons inside the catalyst layer. The protons diffuse through the PEM to the cathode side, where they react with oxygen to produce water while the electrons can be used in an external circuit. The overall reaction

$$\mathrm{H_2} + \frac{1}{2}\mathrm{O_2} \longrightarrow \mathrm{H_2O} \tag{7.1}$$

can be split into the anode-side reaction

$$\mathrm{H_2} \longrightarrow 2\,\mathrm{H^+} + 2\,\mathrm{e^-} \tag{7.2}$$

and the cathode-side reaction

$$\frac{1}{2}\mathrm{O_2} + 2\,\mathrm{H^+} + 2\,\mathrm{e^-} \longrightarrow \mathrm{H_2O}. \tag{7.3}$$

In order for that process to work, a constant level of humidification inside the MEA is needed, a too low level decreases the proton permeability of the membrane whereas a too high level decreases the flow of reagents to and from the MEA [Sridhar et al., 2001]. This water management can be controlled via humidification of the reactant gas. Direct Membrane Deposition (DMD) is a novel MEA fabrication method, where the membrane layer of a PEMFC is directly deposited onto its anode and cathode gas diffusion electrodes using a process comparable to inkjet printing. Beside a high cell power density, fuelcells with this membrane show a stable performance over the whole range of reactant gas humidification from 0 – 100 % relative humidity [Klingele et al., 2015].

7.2.2 Measurements

As a first step of the experiment, the usability of the design for X-ray and neutron radiographies was confirmed before moving to the in-situ radiographies.

Ex situ radiographies

In a first measurement row, the overall absorption and contrast of the sample was measured. One through-plane projection of the fuel cell was taken at a grating based Talbot-Lau interferometer as described in [Prade et al., 2015] and [Prade, 2017] and the results of the three different imaging modalities are shown in Figure 7.3. All three modalities can be used to show the flow channels

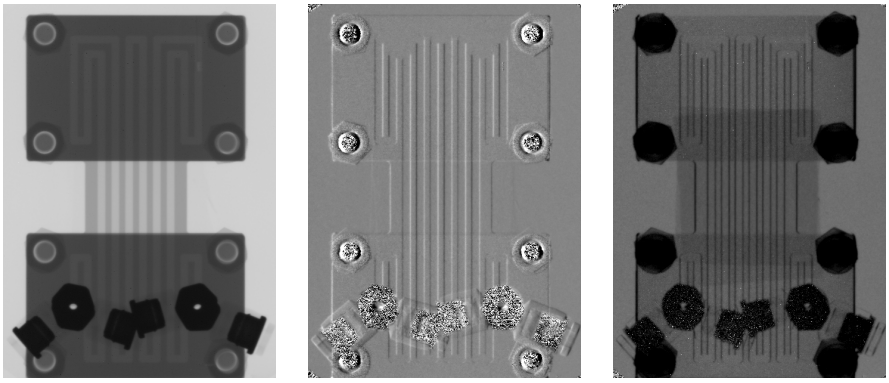

a) b) c)

Figure 7.3: Trough-plane radiographies of the prototype fuel cell in three different contrast modalities. Absorption image a), differential phase contrast b) and dark-field contrast c).

inside the fuel cell, whereas the MEA only is visible in the darkfield or small angle scattering contrast (Figure 7.3 c)). The results from this measurements lead to a redesign of the fuel cell in order to maximize the field of view to contain the largest possible active area of the fuel cell with minimal absorption in the beam direction. A resulting *micro resolution X-ray Computed Tomography* (microCT) from the optimized design, done at the **Zeiss/X-radia Versa XRM**, is shown in Figure 7.4.

7.2.3 In situ radiographies

The in-situ measurements for this work were done at the ANTARES beam-line described above and the sample location is indicated by the hatched area in Figure 7.1. The mounting assembly of the fuel-cell was designed using aluminium to be as transparent as possible to the neutron beam. The fuel cell was contacted with 5 m long heated gas lines to assure constant temperature of the reactant gases and to allow control over the setup from outside of the beam chamber. This is especially important, as the ionizing characteristic of neutrons can otherwise damage the readout and control electronics of the setup. For the neutron experiments, the fuel cell was placed in-plane with the beam direction to observe the dynamic water evolution inside its anode and cathode flow channels separately. An 18 mm pinhole was used, resulting in an L/D ratio of 500 at the sample position. The detector in use was an **Andor Ikon L** CCD sensor with 2048 pixels in each dimension. The effective pixel size was about 27 µm and was determined experimentally from the known geometry of the micro-milled gas flow channels of 500 µm width. All additional measurements beside the neutron radiographies were done with a **Scribner 850e** fuel cell testing system. To extract the actual water generation in the flow channels, the neutron absorption of the dry fuel cell was taken as reference and all images were corrected with a dark image, recorded with a closed beam shutter. The additionally applied gamma spot correction will be explained in detail in the next section. Before each in situ experiment a neutron image under open-

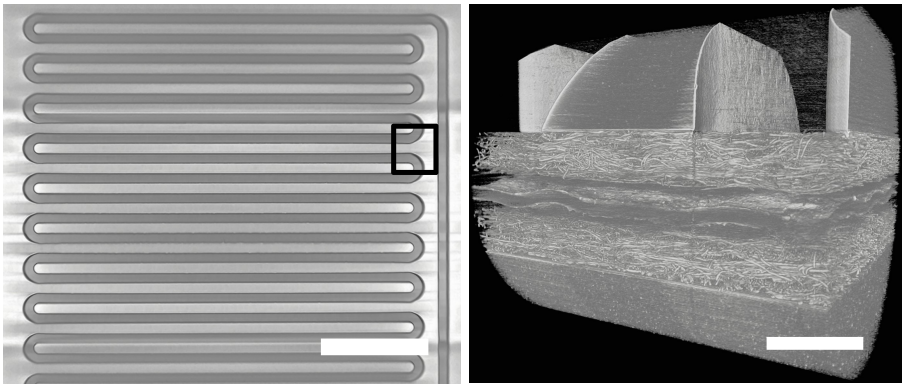

a) **b)**

Figure 7.4: X-ray micro CT of the optimized fuel cell layout. a) Reconstructed slice through the flow channel plate. The black square indicates the cut-out region which is shown magnified in figure b), the scalebar is 5 mm. b) Volume rendering of the cut-out marked in subfigure a). On top, the flow channels are visible, in the middle the MEA with the carbon fibre structure of the gas distribution layer is visible. Scalebar is 500 µm.

circuit voltage conditions was recorded to exclude a falsification by residual water from previous operation. The two different test series described below were done for a DMD sample and repeated with a commercially available N-112 Nafion membrane. Both samples were stacked with the same gas diffusion media for comparability.

Application of a voltage step

In a first test series, the dynamics of water evolution from application of a voltage step to steady state condition was investigated. A fixed potential of 0.5 V was applied to the fuel cell and in situ neutron radiographies were taken each with an integration time of 5 s. During this test series, the *high frequency resistance* (HFR) was measured by a frequency response analyser, which is part of the aforementioned fuel cell tester. Both current density and HFR are measured with 1 s precision, and can therefore be correlated with the neutron radiographies. In Figure 7.6, the results from this correlated measurements are shown. From this figure it can be seen, that besides having a significantly higher current density, the DMD sample converges to a stable current density whereas the N-112 sample shows a drop in current density with a rise of HFR, which in contrary is stable for the DMD sample over the whole measurement period. The correlation with the water evolution measurement shows, that this is connected to a very constant humidification of the MEA in the DMD sample and a drop in humidification in the N-112 sample. Furthermore the huge amount of water on the anode side are a sign for increased back diffusion of water into the MEA in the DMD sample.

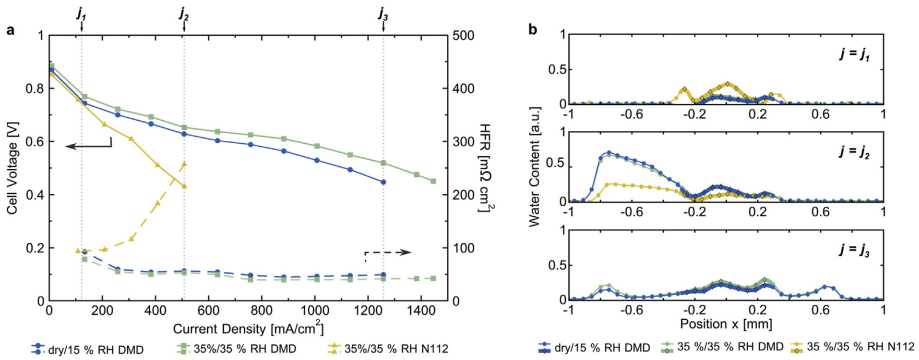

Figure 7.5: Water evolution in different PEMFCs during stepped current densities in a polarisation measurement. a) The cell voltage and HFR is plotted at each current density step. b) Shows the sum of the water profile along the x-axis of the cell as in Figure 7.6. The three different profiles correspond to the current densities marked in a) at 125, 500 and 1250 $\mathrm{mA/cm^2}$. The blue and green lines correspond to the DMD sample, the yellow line corresponds to the N-112 sample. Relative humidities are given below each plot for the anode/cathode side respectively. Taken from [Breitwieser et al., 2016].

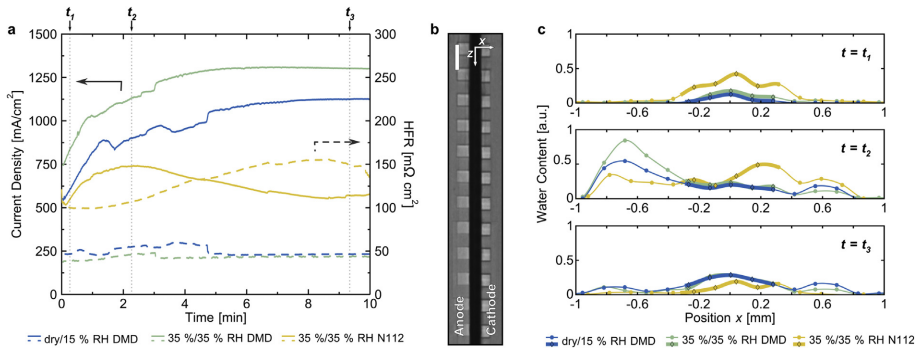

Figure 7.6: Water evolution in different PEMFCs after application of a voltage step. a) The current density and HFR is plotted. b) Shows a radiography of the dry cell for reference of the axis used in c), the scalebar corresponds to 1 mm. c) Shows the sum of the water profile along the x-axis of the cell marked in b). The three different profiles correspond to the points in time marked in a) at 20 s, 140 s and 560 s. In a) and c) the blue and green lines correspond to the DMD sample, the yellow line corresponds to the N-112 sample. Relative humidities are given below each plot for the anode/cathode side respectively. Taken from [Breitwieser et al., 2016].

Polarisation measurement

In a second test series, polarisation curves are measured and a neutron image with an integration time of 60 s was taken at each current density step. At the same time, the resulting cell voltage and HFR were measured. The results are shown in Figure 7.5. As this figure shows, the HFR of the reference sample increases rapidly with the current density and leads to a breakdown of operation at a current density of 500 mA/cm^2. Below a RH of 35 % no operation of the reference cell was possible at all, as even slight loads lead to an immediate breakdown of the fuel cell voltage. For the DMD sample, the HFR is very constant over the whole range of current densities measured. Furthermore the two different operating conditions of the DMD sample lead to very similar HFR curves and at the same time the water profiles are nearly identical. This again shows, the correlation between water management and fuel cell performance. In the N-112 fuel cell, the increase in HFR and the breakdown of fuel cell operation hints to a decrease in proton conductivity due to poor humidification, whereas in the DMD sample the water level evolution hints to an enhanced back diffusion which results in constant membrane humidification.

7.3 Image processing

In this section, the three main image processing procedures used for the neutron radiographies in this work are described in detail. The results in the next section have been published in [Schock and Schulz, 2018].

7.3.1 Gamma spot removal

As mentioned in subsection 4.2.6, high energy particles may lead to unwanted noise in an image, which are referred to in this work as *gamma spots*. This is especially true for neutron imaging, as secondary particles in the form of high energy gamma radiation are present in nearly every image and therefore massively deteriorate image quality. Simple image filters like a median filter or a Gaussian blur can be used to correct images for this kind of noise with the compromise of decreasing image quality in respect to image detail due to the spatial averaging nature of these filters. To preserve image detail and at the same time eliminate bright spots, adaptive algorithms can be used that match the strength of a image filter to some metric, describing the presence and strength of image artefacts. As a result, this kind of filters act locally at image areas where noise is present and have minimal influence in the remaining image area. **Li et al.** describe such an adaptive algorithm suitable for gamma spot removal and their findings will be shortly summarized in the following.

To define the areas, where gamma spots are present in an image, an edge finding filter is applied to the image. Gamma spots are bright spots in a relatively uniform background, therefore they represent a fast changing intensity in a small, confined area. In contrast, image edges are relatively smooth and can therefore be discriminated by a suitable edge finding algorithm. A Laplacian of Gaussian (LoG) filter is a well-known edge finding algorithm and is a

convolution with the LoG kernel, that can be written in the discrete form

$$h(n_1, n_2) = \frac{(n_1^2 + n_2^2 - 2\sigma^2)h_\mathrm{g}(n_1, n_2)}{2\pi\sigma^6 \sum_{n_1} \sum_{n_2} h_\mathrm{g}}, \tag{7.4}$$

with the abbreviation

$$h_\mathrm{g}(n_1, n_2) = e^{-(n_1^2+n_2^2)/(2\sigma^2)} \tag{7.5}$$

and n_1 and n_2 denoting the position of the kernel element in each dimension. The filtered image shows high intensities in areas, where a fast change in image intensities is present in the original image. By thresholding the filtered image, only the high intensity pixels corresponding to gamma spots in the original image can be selected. If different threshold levels are chosen, the intensity of the gamma spots can further be divided into classes. A subsequent smoothing filter, such as the aforementioned median filter, can be adaptively chosen to act stronger on those gamma spots with a higher intensity and weaker on low intensity spots, therefore preserving as much as possible image detail. [Li et al., 2006]

Especially when dealing with huge datasets, the performance of image processing algorithms is crucial. Dynamic measurements can easily comprise several hundreds of projections and the numbers increase drastically when moving towards high frame-rate acquisitions as needed in super resolution measurements. This is also true for tomographic reconstruction, where the whole processing chain has to be done several times in order to tweak free parameters to optimize the end result. The proposed LoG filter has been chosen as a proof of concept, how such an image processing pipeline with several steps can be implemented in a performant way and optimized for throughput and speed.

Profiling

In a simple test implementation, it can be seen, that in principle the running time for the algorithm is a simple addition of the running time for the convolution with the LoG kernel and the running time for the median filter as the time needed for thresholding can be neglected. Figure 7.7 shows the running time of the convolution and the two-dimensional median with three different window sizes acting on three-dimensional arrays with variable z-size and equal x and y sizes of 1024. This array corresponds to a stack of z images with a 1024×1024 shape. The resulting runtime of the complete LoG-filter based gamma spot removal strongly depends on the chosen thresholds: In the observed range, both the median and the convolution scale linearly with the size of the z-axis and therefore also linearly with the number of pixels in the array. As in the adaptive filter described above, three different thresholds are set and the corresponding median kernel size is selected accordingly, the median filter only acts on pixels between the respective thresholds. Linearly extrapolating the values measured and plotted in Figure 7.7, the calculated values for one

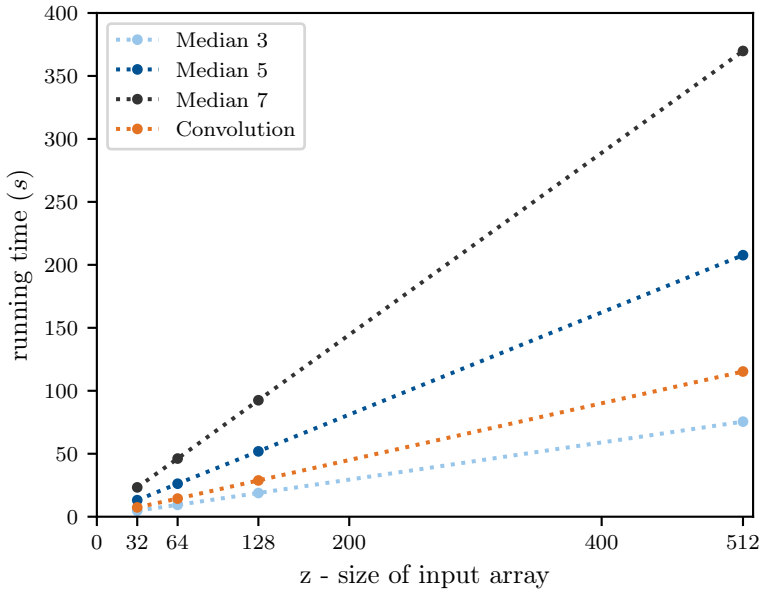

Figure 7.7: Running time of different image processing algorithms compared with the z-size of the three-dimensional array $[z, 1024, 1024]$ on which they are acting. All implementations are single-threaded and scale approximately linear. The median runs are two-dimensional median filters with the size being the x and y dimensions of the lookup-window. The convolution is done with the LoG Kernel with a size of 9×9 and $\sigma = 0.8$. Benchmark implementations are done with **scipy.ndimage** [Jones et al., 2001].

2048×2048 pixel image can be calculated to be:

$$\begin{aligned} \text{Convolution} &= 0.91\,\text{s} \\ \text{Median3} &= 0.59\,\text{s} \\ \text{Median5} &= 1.63\,\text{s} \\ \text{Median7} &= 2.89\,\text{s}. \end{aligned}$$

To get an estimate of the running time for the whole image, the median runtimes can simply be multiplied with the noise density which is the number of resulting points in each threshold band. The example in [Li et al., 2006] mentions a noise density of 13.35 %, 1.68 % and 0.33 % in the chosen threshold bands for a respective median size of 3, 5 and 7. With these noise densities, the overall runtime is dominated by the time taken in the convolution step and is about 1 s. Compared with the running time of 5 s mentioned by **Li et al.**, this suggests, that there is room for improvement in the implementation.

Optimization

In order to speed up the LoG filter, it was massively parallelized and ported to OpenCL to make use of GPUs as processors. The outline of the resulting algorithm is described in the following. In a first step, the input array is split along its z-axis into sub-arrays that fit into the texture memory on the GPU. The z-axis was chosen in order to not have image boundaries inside the image area, which would arise when tiling in x- or y-direction and would have to be treated with special care due to arising boundary conditions. As all file transfers from the host to the OpenCL device tend to be slow, the whole sub-array is copied at once and the whole LoG filter is run on the sub-array before copying the next work junk. The convolution part is split into one kernel per window, so that the result can be calculated for each pixel in parallel. The same is true for the subsequent runs of the threshold kernel and the binary dilation. As an example, the source code of the LoG convolution is shown in Listing 1. The last kernel is an adaptive median, that runs the median parallelized on each pixel with the size defined by the threshold kernel. The OpenCL kernel is listed in Listing 2. This algorithm ensures, that no additional copies between host and device are necessary between the single image processing steps. Furthermore, by using OpenCL's image memory object, subsequent reads to neighbouring pixels are cached and therefore speed-up. On the host, each kernel invocation is passed through a wrapper, that enriches each kernel call with an OpenCL event and allows exact timing from the moment the kernel is enqueued into the job queue up to it being finished. For benchmarking a worst case scenario, a 3D array containing $64 \times 1024 \times 1024$ random integers between 0 and 1000 where created, which corresponds to an image stack of 64 images with the resolution delivered by the camera. The result of the LoG kernels acting on this array with thresholds set to 50, 100 and 400, running on one **Nvidia Tesla K10 G2** is shown in Figure 7.8. The resulting running time is about 0.5 s for the whole

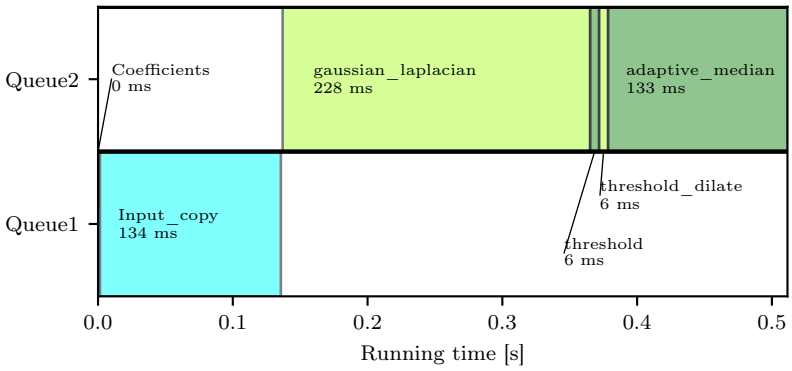

Figure 7.8: Running time of an optimized version of the Laplacian of Gaussian adaptive median filter. Queue 1 lists all input timings, Queue 2 holds all numeric calculations, each coloured block is one separate kernel. Shown is the timing for one run of the whole LoG filter on a 3D array with a size of $64 \times 1024 \times 1024$ random values between 0 and 1000 with thresholds at 50, 100 and 400.

image stack, including transfers to the device. This is a speed increase of 160 times compared to the non-parallelized version presented by **Li et al.**. Transfer time back to the host from the device is not included, as this time depends strongly on the speed of the output storage destination. The time needed for output is roughly equal to the input time and scales linearly with the size of the output. Furthermore, if necessary, the speed can simply be increased by using multiple OpenCL devices, each with their own command queues. As in this implementation, all pixels are handled in parallel, the running time is constant over a whole range of noise densities, as additional pixels do not add to the overall run-time as long as the calculations can be covered in the unoccupied workspace on the GPU device. When running the algorithm on larger arrays, it is automatically tiled in a way, that each sub-array can be handled by the benchmarked algorithm. Each subsequent block of 64 images takes exactly the same time. On devices, where the copy kernels are allowed to run in parallel with the numerical calculations (which is true for most modern graphics cards), the input transfers can be overlapped with the calculation for additional speed-up.

Results

The result of the LoG filter applied to the in-situ fuel-cell neutron radiographies is shown in Figure 7.9. It can be seen, that the noise can be effectively removed while keeping the image structure. This filter has been applied to all images acquired at the ANTARES setup.

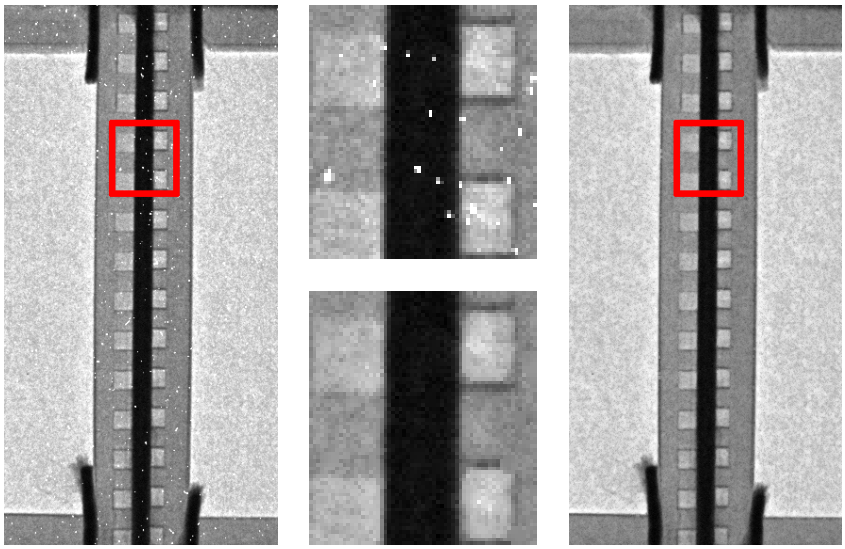

a) **b)** **c)**

Figure 7.9: One projection of the in-situ neutron radiographies of a fuel-cell. Subfigure a) shows the uncorrected radiography, c) shows the same radiography after correction. Red boxes indicate the regions shown in the magnification in b) with the corrected version being below the uncorrected version.

7.3.2 Adaptive mean

In the section above, all image processing steps were applied to one single image. The information to correct outliers is taken from a spatial neighbourhood. This is especially useful in environments where a change over time has to be recorded with a temporal resolution that results in changes in the image series over time. In contrast to this situations, there are several applications, in which statistics over an image series has to be gathered. As an example, in order to get the standard deviation of the camera noise, several frames have to be acquired in order to be able to calculate the desired measure. Especially in low-light environments, these values have to be calculated very precisely in order to discriminate low-count events from e.g. pixel noise. Extreme outliers as seen in the examples above can be corrected for with a spatial filter as e.g. the median filter. However, the replacement values are from the spatial neighbourhood and differences in the noise of single pixels are therefore not taken into consideration. Furthermore, there are cases, where a local event has a large influence area, which makes locally acting filters impossible. One example is the large tail caused by charge overflow of direct hits, as depicted in Figure 4.1. Therefore to get correct values for statistical measures of single pixels over time that are free from additional external noise, the affected pixels have to be detected in each frame and excluded from the calculation.

Implementation

In a first step, the mean and standard deviation of one image in the stack is calculated. Depending on the quality of the noise, three different noise finding methods can be applied. In simple cases of additive salt and pepper noise, constant thresholds can be given. If the noise is dependent on image intensity, which is especially the case for noise that is scaled with the image gain e.g in EMCCDs, the threshold can be chosen in terms of standard deviations from the image mean. The third approach is taking the first step of the LoG algorithm above for edge finding. Once chosen, the threshold can usually been used for the whole stack of images. The images are transferred to the OpenCL compute device and a mask is built on the device, that has the same dimensions as the image. The mask is pre-populated with ones. Depending on the threshold, a region of the mask in the neighbourhood of affected pixels is set to zero to indicate, that these pixels are to be excluded from further calculations. As an example, the long streaks resulting from charge transfer in Figure 4.1 can be masked by taking a structure that extends several tens of pixels in the direction of camera read-out which in this case is towards the right direction in the image. After masking is done, the image statistic measures can be calculated using the mask as multiplicative weight. In order to preserve numerical precision, algorithms as described in subsection 5.3.3 are used. The adaptive mean is used in this work for averaging of dark- and open-beam-images produced at the neutron source, as these images are prone to noise from scattered radiation, activation of elements close to the detector or high energy gammas from nuclear reactions.

7.3.3 Image stitching

The image registration algorithm described in section 4.3 can be used to minimize differences between a template and an image, which is a slightly transformed versions of the image. The output of this algorithm are the free variables needed to apply this transform to the image to match the template as closely as possible. Another application of this algorithm is the fusion of two images, that have been acquired at slightly different detector positions. This image fusion is often referred to as *stitching* as several input images are combined to form one big, continuous image. Image stitching is essential in imaging applications, where the sample exceeds the field of view of the detector system and the sample has to be scanned at different positions. An example of a stitched image is shown in Figure 7.10. It is possible to shift either the sample relative to the source-detector assembly, or the detector relative to the sample. The first approach has the advantage, that the beam geometry stays constant and therefore the magnification, opening angle, beam intensity etc. stay the same. However, in this approach, areas of the sample which are at the edge of the FOV in one scan, can end up in a central position in a subsequent scan. This leads to same areas of the sample being pictured in different magnifications relative to each other due to image aberrations as described in subsection 3.2.2. In the second approach, the mechanical shift of the detector can be seen as sampling a bigger, virtual detector. Therefore, the imaging aberrations are limited to those introduced by the optical system and the aberrations introduced via the beam geometry can be neglected. If the relative shifts are kept constant between measurements, the resulting image aberrations can be measured and corrected for, by picturing a template sample. This approach will be discussed in detail in the next chapter.

Figure 7.10: An illustrative example of image stitching. The original image, taken from **scipy.misc.ascent**, is shown in a) [Jones et al., 2001]. b) and c) show overlapping regions of a), where c) is the inverse of the original image, the vertical lines indicate the border of the overlap. d)-f) show the result of blending the images together with a two-pixel mismatch and different blending functions. d) is the average, e) is a linear and f) a sigmoid blending.

Implementation

Especially in neutron radiography, the source-detector distance is much larger than the sample-detector distance, which leads to an approximate parallel beam geometry. Therefore, the transform in the image space to map one stitching section to another is mainly dominated by shifts. In cone beam geometries, as experienced in most X-ray setups, this doesn't hold true and an additional homography has to be added to account for the resulting camera shift, pitch and yaw. In order to be able to stitch two subsequent FOVs together, they have to be taken with a common, overlapping area in order to calculate the relative transform between the two images from that shared information. The relative transform is calculated for this regions, using the Lukas-Kanade algorithm as described in section 4.3, and applied to the complete image.

Image blending

After calculating the transform to connect two subsequent FOVs together, the images have to be combined. The area in which the common information is present has to be treated with special care. The reason is, that although the Lukas-Kanade algorithm minimises pixel differences between the overlapping areas, the resulting difference is usually non-zero due to uncorrected aberrations or sampling differences due to slightly different imaging positions. If two regions of the image are combined by simply adding them side by side, the edges of the regions become visible in the image. In order to get a homogeneous transition between stitched regions, the overlapping areas can be blended into each other. If the two overlapping regions are referred to as A and B and the coordinate transforms have been applied to both images, in a way that the pixel at (x, y) pictures the same sample area, the resulting blended overlap C can be written as a function of the pixel values of A and B:

$$C(x, y) = f(A(x, y), B(x, y), x, y), \tag{7.6}$$

where f is a general function, referred to as *blend function*, acting on the intensity values of A and B and can (but doesn't have to) depend on the position. The pixel-wise addition of A and B or the pixel-wise mean of A and B are simple examples of possible blend functions. All blend functions used in the scope of this work can be written as weighted additions of the pixel values in the form

$$f = a(x)A(x, y) + a'(x)B(x, y), \tag{7.7}$$

where a and a' follow several boundary conditions. Both functions are normalized and output values in the interval $[0, 1]$ with $a(x) + a'(x) = 1$ everywhere. Furthermore if the two functions are not identical and constant, a is strictly monotonously falling and a' is strictly monotonously rising. These conditions ensure, that the overall intensity of the blended area is continuous and there is a smooth transition between A and B. Examples of functions that follow these conditions are linear or sigmoid functions such as the error function. An example of the influence of different blend functions can be seen in Figure 7.10 d)-f). The average blend in Figure 7.10 d) leaves visible edges in the resulting image, which is no longer visible in the linear or sigmoid blend. The sigmoid blend results in a smaller intermediate region compared to the linear blend but

also to faster changing intensity values in the case of strongly different image intensities. An example of a projection stitched together from several ROI projections is shown in Figure 7.11. The sigmoid blend is chosen here, because the image borders are prone to noise, which is suppressed in the result.

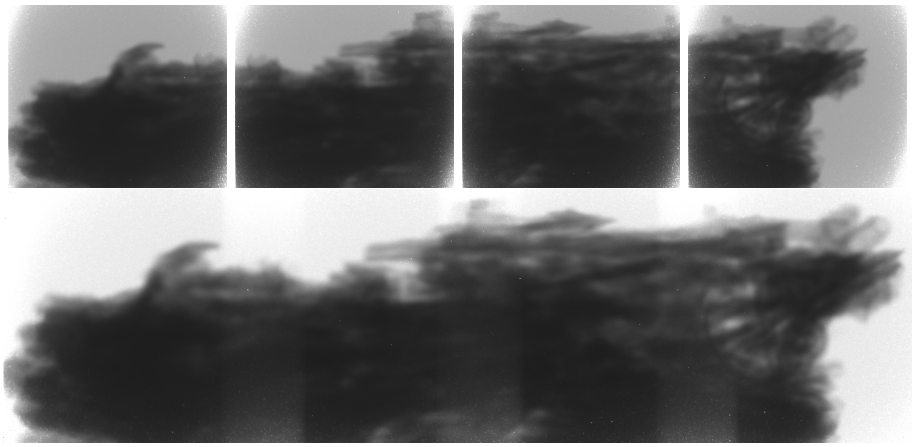

Figure 7.11: Image stitching with neutron radiographies from a cultural heritage sample scanned at the NECTAR experiment. Top row: Single ROI radiographies with approximately 150 pixel overlap. Bottom row: Stitched projection.

7.4 Conclusion and outlook

Neutron imaging is a valuable tool in non destructive testing and can be used complementary to X-ray applications especially when materials are involved that show a poor contrast in one of the two modalities but an enhanced contrast in the other. The fuel-cell measurements show, that neutron radiography can give dynamic information as shown along the example of water evolution. The image processing tools developed in this work are applicable to a wide range of neutron imaging applications and can be optimised for high throughput using massive parallel implementations as shown along the example of the implementation of the LoG filter on GPUs. In general, a lot of image processing algorithms that are already in use in the X-ray community can be easily transferred to neutron imaging with only slight adjustments needed, which arise from lower image statistics and a difference in noise characteristic. Increasing the resolution in neutron imaging is mainly driven by the development of new scintillators, so that enhancing image quality by post-processing will be an important field in the future.

Chapter 8

Dual Energy CT

All presented results in this work so far are based on absorption measurements from a single source. As mentioned in chapter 1 and chapter 2, the source spectrum is a defining characteristic of sources both in X-ray and in neutron radiographies and tomographies. In subsection 1.4.2, the advantage of using different spectra to gain additional information is discussed. This chapter presents a conceptual dual energy X-ray setup, that is an application of this principle. Parts of the results in this chapter are published in [Maier et al., 2017].

8.1 Introduction

The realisation of the `dual-energy imaging` methods described in subsection 1.4.2 can be separated into two classes, source based and detector based. Source based methods use different sources or one source at different energies to produce distinct spectra. This can be done by doing two imaging passes with the same sample and changing the source parameters in between or during the measurement (known as rapid voltage switching). These methods have in common, that the dose absorbed by the specimen is increased in comparison to the single energy measurements. Besides from the approach with multiple sources, the measuring time is also increased. The advantage of this approach is the relatively free choice of spectra, that can be matched to the desired application. The other class of spectral methods are detector based. In this approach the measurement has to be done with a polychromatic spectrum coming from one single source. The detector has to be built in a way that allows differentiation between particles of different energies. This can be realised by using photon-counting detectors or layered detector assemblies. The advantages of this approach are the constant dose and measuring time compared to the mono-energetic case. Disadvantages are worse separation of the spectra and more complicated detector design. In the next section, the application of a layered detector together with a laboratory polychromatic X-ray tube to allow for dual-energy imaging will be presented.

8.2 Setup

In this section the different parts of the setup are presented together with the considerations behind their planning and realisation.

8.2.1 Hutch

As all experiments are done in a laboratory environment with supervisors present, all expected radiation has to be contained inside an experiment hutch to minimise the dose an operator or user experiences. The most important factor for all this considerations is the peak energy of the source in use and therefore of the expected radiation. Lead has a very high total absorption cross section of

$$\mu(\text{Lead}, 65\text{keV}) = \mu_\text{m}(\text{Lead}, 65\text{keV}) \cdot \rho_\text{Lead} = 46.35\,\text{cm}^{-1} \tag{8.1}$$

due to its high atomic number, where μ_m is the mass attenuation coefficient. The proposed thickness to shield medical X-ray tubes with a peak voltage of 70 kV is 1 mm [Petrantonaki et al., 1999]. The hutch designed during this work

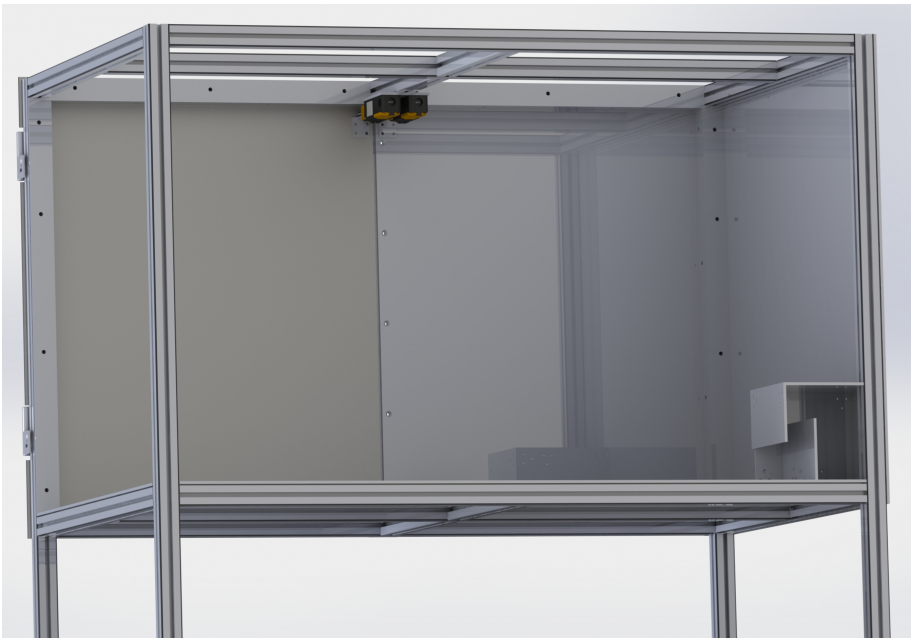

Figure 8.1: A 3D rendering of the X-ray hutch designed for this work, view from the back of the hutch, back-, side- and top-shielding are hidden for illustrative purposes. The chicane is on the bottom right, two door-switches from the interlock system are shown in yellow holding both of the doors shut on the top.

is expected to be reused in a variety of applications and therefore the shielding is dimensioned to allow for X-ray tubes of a peak voltage up to 125 kV. In direction of the primary radiation (beam direction) a lead thickness of 3 mm is chosen, everywhere else the chosen thickness is 2 mm. The walls are constructed

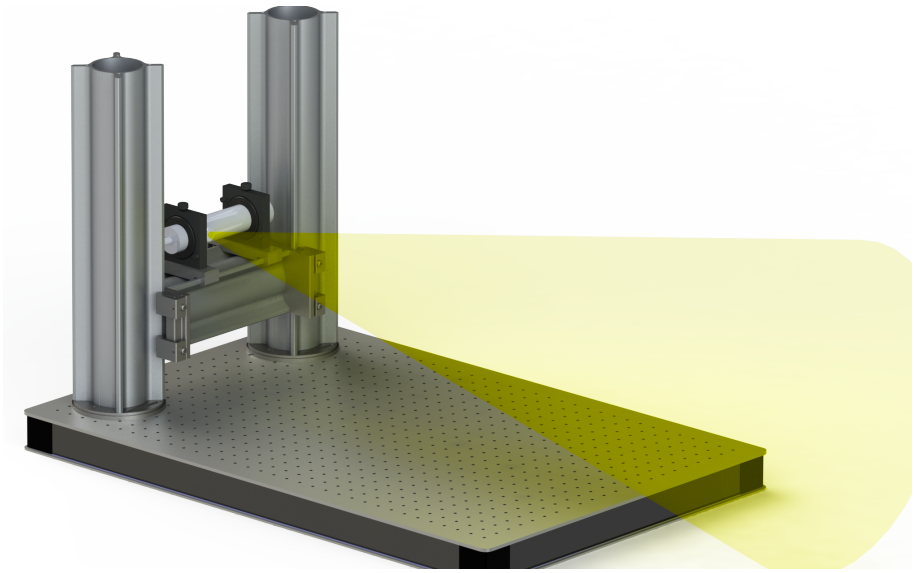

Figure 8.2: 3D rendering of the source assembly. The yellow area indicates the beam direction and opening angle.

as aluminium-lead-aluminium sandwich-plates in order to not expose any user to possibly toxic lead contaminations. To allow for connections to the outside, a zig-zag shaped chicane is constructed in a way that no direct pathways for radiation are present. The design was optimised with a Monte-Carlo simulation of the expected scattering pathways using **Geant4**. The hutch is equipped with doors that incorporate a security interlock system that only allows the X-ray source to be switched on when fully closed. A rendering of the hutch is shown in Figure 8.1.

8.2.2 X-ray source

The X-ray source used for the test measurements is the same source as mentioned in subsection 6.3.3, a **MCBM 65B-50 Mo** from **RTW** with a peak voltage of $U_{\mathrm{Peak}} = 65\,\mathrm{kVp}$ and a molybdenum target. However, after optimising the parameters in the scintillator stack, the source was changed to an X-ray tube with a tungsten target and a peak voltage of $U_{\mathrm{Peak}} = 160\,\mathrm{kVp}$ to demonstrate the full potential of the energy separation. The high-voltage generator, a **SpellmanHV** μ**X**, is connected to the interlock system to allow for secure operation and emergency shutdown. The X-ray source is mounted on a height-adjustable rail for flexibility of the beam position and fixed to an optical breadboard together with the optical system for enhanced stability of the whole setup. A rendering of the setup is shown in Figure 8.2.

8.2.3 Detector system

The detector system is the most complicated part of the setup and will be broken down into three components: the scintillator, the optical system and

the camera assembly.

Scintillator

As this setup is designed as a layered detector to enable dual energy measurements, two different scintillators are employed that absorb different portions of the broad polychromatic spectrum produced by the X-ray source. When X-rays traverse material, the photons with lower energy are more easily absorbed than those with higher energies and the remaining spectrum has a higher mean energy, an effect that is known under the term `beam hardening`. Therefore, when choosing two different scintillators that are to be positioned behind one another, the front/top scintillator should be optimised for the absorption of low energies and the back/bottom scintillator should be optimized for high energy absorption. By introducing a separation layer between the two scintillators,

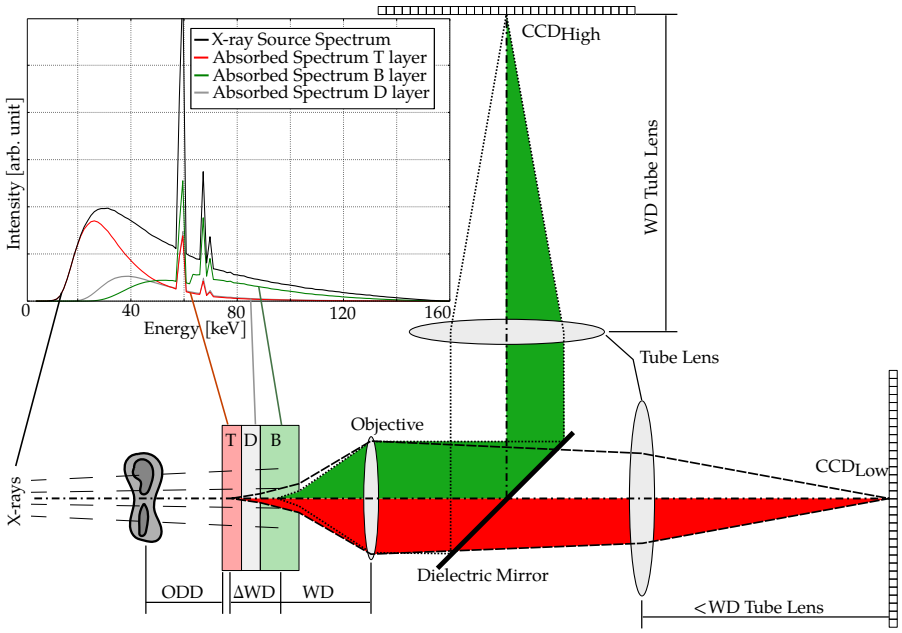

Figure 8.3: Conceptual drawing of the scintillator arrangement and the different beam paths behind the beamsplitter. The objective lens collects the emitted light from the two scintillators, where the red beam refers to light from the top scintillator (T) and the green beam path refers to the bottom scintillator (B), D marks the dividing layer. The beamsplitter reflects the high energy portion of the incoming spectrum and transmits the low energy portion. The inset shows the energy spectra absorbed by each layer in the scintillator stack. Image taken from [Maier et al., 2017].

the beam hardening effect can be used to further separate the recorded spectra. All three layers have to be transparent for the produced light in order to be able to record the emission behind the whole stack. Furthermore, the emission spectra of the two scintillation layers should not overlap in order to be distinguishable by the optical system. At last, the thickness of the layers

has to be chosen to compromise between light yield and achievable resolution. The chosen scintillator materials are ZnSe:Te for the low energy absorption and lutetium-yttrium oxy-orthosilicate (LYSO:Ce) for the high energy absorption. The dividing layer was chosen to be ZrO_2 due to its high `attenuation` in energy ranges of 19 – 80 keV.Further characteristics of the three layers in the stack are listed in Table 8.1.

Table 8.1: Characteristics of the three layers in the scintillator stack. The employed layer thickness is d, the mean absorption $\bar{E}$ is calculated with an input spectrum of a tungsten anode at 160 kVp and with a water target of 10 mm. The emission is given at the peak value.

Layer	Material	d (μm)	$\bar{E}$ (keV)	Emission (nm)
Front/Top	ZnSe:Te	200	35.08	640
Dividing	ZrO_2	200	51.03	–
Back/Bottom	LYSO:Ce	600	70.83	425

Optical setup

The optical setup is used to split the light coming from the scintillator stack into two distinct beam paths to allow for separate recording with two charge integrating detectors. The core piece of this assembly is a dichroic mirror. A dichroic mirror is an optical device that consists of layers of materials with different refractive indices. Incoming light gets diffracted differently dependent on the wavelength. Such a device can be tuned to reflect light below a certain wavelength and transmit light above this wavelength, referred to as `cut-off wavelength`. Such a dichroic mirror is also referred to as beam-splitter. If the cut-off wavelength is chosen to be in between the emission wavelengths of the two different scintillators, the beam is split by the dichroic mirror and light from each scintillator reaches only one detector. A principle drawing of this concept is shown in Figure 8.3. The other parts of the optical system form a modular microscope. The objective produces a parallel beam path in which the mirror can be placed without considerable aberrations. In each subsequent beam path, focussing optics are present in the form of a tube lens to project the image onto the detector plane of the camera.

Cameras

The main imaging sensors are the two identical **Finger Lakes Instrumentation (FLI) PL1001E** cameras with a FOV of 1024 × 1024 pixels with a pixel-size of 24 µm. They are connected to the tube lens of their corresponding individual beam path via a Precision Digital Focuser (PDF), which is a motorized device to adjust the distance between imaging plane and tube lens. This assembly is shown in Figure 8.4. If the middle of the scintillator stack is placed in the working distance of the objective and the focal depth comprises both scintillator layers, the PDF can be used to focus each camera on their

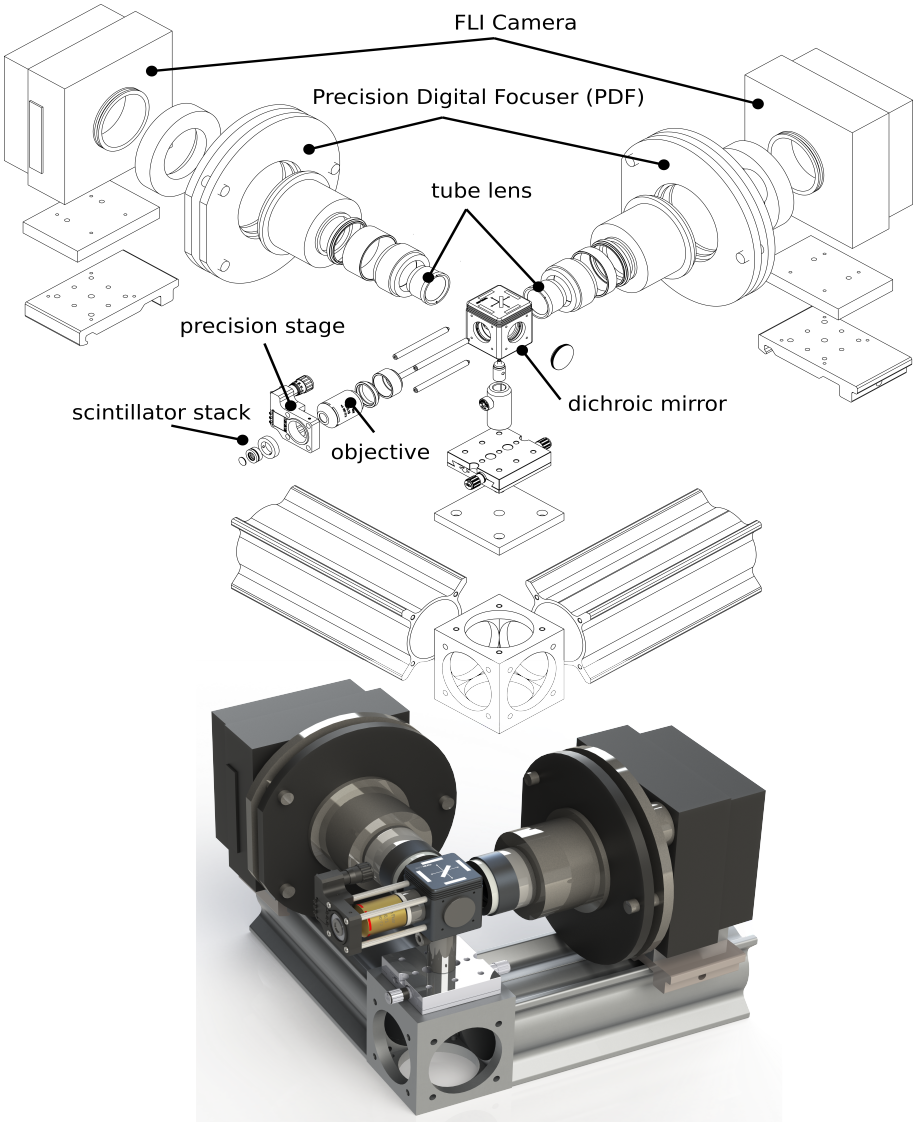

Figure 8.4: Explosion drawing and 3D rendering of the dual-detector assembly.

corresponding scintillator. To adjust the system for large differences in scintillator thicknesses, distance adjuster rings with different thicknesses can be introduced between tube lens and PDF.

8.2.4 Image registration

For dual energy imaging it is important, that one region in the sample is pictured by corresponding pixels in the two different beam paths. As the optical paths are different for the two scintillators and therefore for the two different energies, the resulting images are not identical in position. Small misalignments

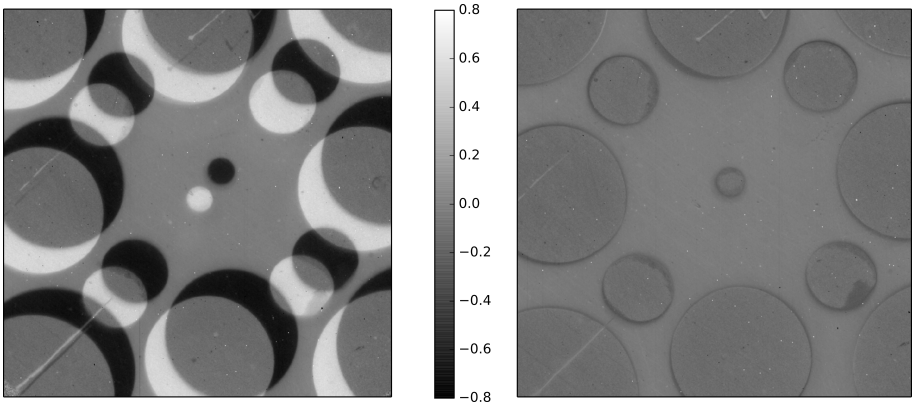

Figure 8.5: The difference between the high- and low-energy measurement before (left) and after alignment (right). The sample is a stainless-steel plate with drilled-in holes in different sizes.

in the beam paths lead to shifts or rotations from the image of one detector to the other. Furthermore the intrinsic different image distances lead to a different scaling of the images due to slightly different magnification. This image offset could be corrected in post processing via image registration. However, as the misalignments are constant between measurements once the setup is focussed, it is also possible to measure the image offset once and apply the corresponding correction to all images. For this correction measurement, a sample with very high contrast was produced and measured. The resulting images for each detector can then be registered with the algorithms mentioned in section 4.3 using the affine transformation model which allows for shift, rotation, scale and shear. The resulting affine transformation matrix holds the offset information of the setup and can be directly applied to the images for correction. The effect of image registration is shown in Figure 8.5, where the two images before and after registration are shown.

8.3 Results

Simple radiographies with one spectrum result in one value of `attenuation` per pixel. In spectral imaging, each used spectrum used results in one value of energy dependent `attenuation` per pixel and therefore adds one dimension in the result space. In the mono-spectral case, image segmentation can be done

on a histogram basis, where the occurrence of `attenuation` values is counted and sorted into bins. Another possibility to segment images is working on the `attenuation` values directly and e.g. setting thresholds. For dual-energy measurements this principles are transferable. If the `attenuation` values are plotted in a two-dimensional histogram, referred to as `energy map`, pixels that correspond to sample areas containing the same material show clusters of points in the energy map. Pixels that contain the same materials can be selected

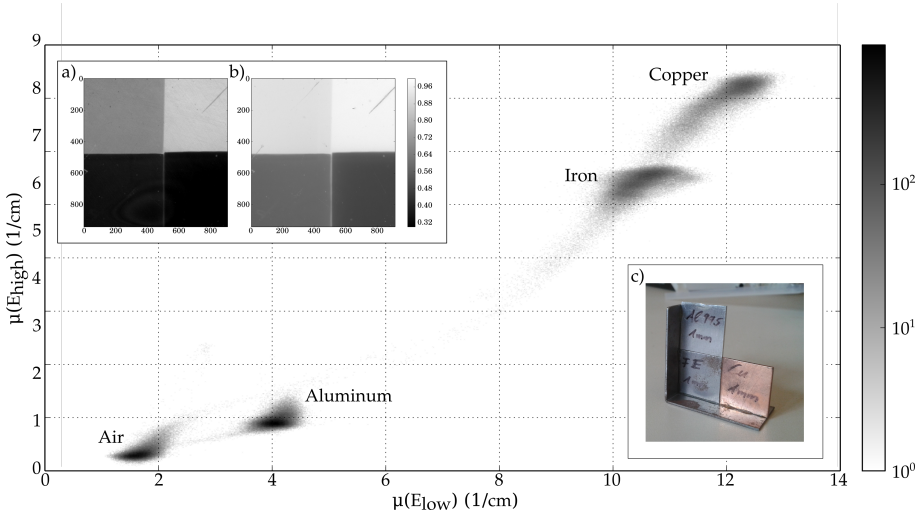

Figure 8.6: Dual energy radiography of three different metal plates visualised in an energy map. The inlet shows the low- (a) and high-energy (b) radiographies and a photography of the sample (c). Each metal plate is 1 mm thick. The radiographies are taken at 160 kVp with an exposure time of 30 s. Image taken from [Maier et al., 2017].

by identification and selection of these cluster in the energy map. An example is shown in Figure 8.6, where an aluminium- an iron- and a copper plate show distinct clusters in the energy map. The same principle can be applied to tomographies, where the energy map can be used to segment point clusters, that correspond to pixels within the same material in the sample. In Figure 8.7, an example is shown, where material segmentation is shown on the two mono-spectral measurements and on the combined dual-energy measurement. In the mono-spectral case, histogram thresholding is used to segment pixels corresponding to a high-absorption material. In both subfigures Figure 8.7 a) and b), the threshold is chosen to be as low as possible to include all of the selected material without getting a selection in the rest of the bulk material. It can already be seen from these two images, that the quality of the selection strongly depends on the employed spectrum. In Figure 8.7 c), the segmentation is done on the energy-map of the dual-energy acquisition. Two distinct materials can be separated and their effective atomic number can be estimated. Due to the statistic nature of the acquisition, the dual energy segmentation shows slightly smaller segmented volumes. However, this can be circumvented by using the information from the dual-energy segmentation to label the result gained by the segmentation on the mono-spectral measurements.

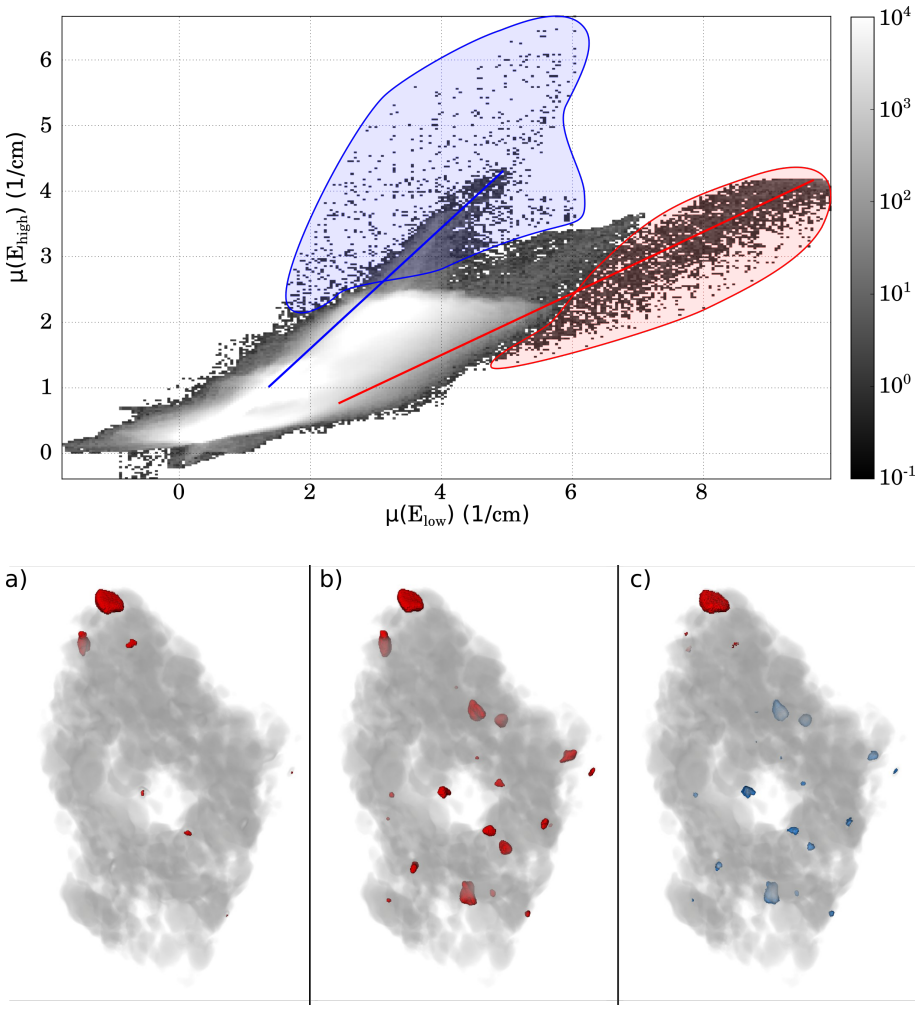

Figure 8.7: Top: Energy map of a tomographic scan of an ore sample. The selections are shown in red and blue and the line indicates the effective atomic number of the material. Bottom: 3D volume rendering of ore sample with segmentations. The result from thresholding on the mono-spectral low- (a) and high-energy (b) images show only one material. The result from the segmentation using the dual-energy scan and the energy map is shown in c), where different materials can be distinguished. Adapted from [Maier et al., 2017].

8.4 Conclusion and Outlook

With the use of a layered detector and after registration of the separate beam paths, it is possible to record dual-energy datasets with a lab based X-ray source in one single shot. This allows the use of this technique as a standard in non-destructive testing and research. The two biggest advantages of this approach are the dose and the exposure time, which are equal to those in a mono-spectral scan. Although the optimisation of such a setup is difficult due to the enormous range of variables such as scintillation materials and thicknesses, once the setup is assembled, it is usable for a big range of applications. The modular nature of the setup allows for fast changes and adaptions to different applications. The setup can be optimised in different directions, such as resolution, spectral sensitivity or light output and therefore imaging time. Future development could investigate the possibility to use more than two layers in the scintillator stack, allowing fluorescence imaging or using the second beam path to couple-in other light sources to enable e.g. STED imaging.

Glossary

Notation	Description	Page List
(F)PALM	(Fluorescence) PhotoActivated Localization Microscopy ((F)PALM) is a super resolution imaging technique with a full field approach.	65
attenuation	Attenuation describes the decrease of the amplitude of an electromagnetic wave or the decrease of the number of particles in a beam and therefore its intensity.	10, 103, 105, 106
background	Background or underground refers to a non-zero signal that is unwanted and therefore has to be corrected for e.g. by subtraction of a dark image.	43
band gap	The band gap is an energy range where no electron states are allowed to exist.	11
band structure	The band structure describes the position of the energy levels in a bulk solid.	11
beam hardening	Beam hardening is an effect where the mean energy of a polychromatic beam increases when travelling through material due to the higher absorption-probability of low energies.	102
bremsstrahlung	Bremsstrahlung is the continuous part of the X-ray spectrum, created by acceleration of charges in an electric field.	2, 3, 5
conduction band	The conduction band is the energy level above the valence band. Electrons in the conduction band can mostly move freely and therefore participate to conduction.	11
convolution	The convolution of two functions as described in Equation 3.19, describes the overlap of two functions.	15, 16, 33, 34
core	A core is a logical unit consisting of dedicated processor and memory management units.	51
CPU	The Central Processing Unit (CPU) of a PC is the main logical unit which does memory and resource management as well as computations.	51–54

Notation	Description	Page List
cut-off wavelength	The cut-off wavelength of optical elements, such as dichroic mirrors, is the wavelength at which an incident beam changes from being reflected to being transmitted.	103
depletion region	The depletion region is a region inside doped semi-conductor material, where the excess charges are moved away either by diffusion or the application of an external potential. The depletion region therefore acts as an insulator.	11
dispersion	Dispersion is the name of the effect, that light with different wavelengths can take different beam paths in optical media.	29
DMD	Direct Membrane Deposition (DMD) is a production technique comparable to inkjet printing in which the active layers are directly applied to the membrane of a fuel-cell.	84, 86–88
doping	Doping is a process where impurities with different electronic configuration are introduced into a semi-conductor material to alter its band structure.	11
dual-energy imaging	Dual-energy imaging refers to imaging applications with two distinct energy spectra.	10, 99
EMCCD	An Electron Multiplying Charge Coupled Device (EMCCD) is a solid state detector, where the readout electrons are multiplied inside a gain register and therefore have very low readout noise.	39
energy map	refers to the two-dimensional histogram from a dual-energy measurement where each axis corresponds to one spectrum.	106
FBP	Filtered Back Projection (FBP) is a reconstruction technique in computed tomograhpy where the influence of the PSF is minimised by the addition of a filter kernel.	16

Notation	Description	Page List
FEL	A Free Electron Laser (FEL) is a high brilliance X-ray source with highly monochromatic radiation due to microbunching of electrons in an undulator and their coherent emission.	4, 5
FREM	Fundamental REsolution Measure	65, 67
FWHM	The Full Width at Half Maximum (FWHM) describes the width of a function between the points where it has fallen to half its maximum.	6, 13, 65, 71, 79
Gaussian pyramid	The Gaussian pyramid describes an image stack, where each layer holds the same image in different sizes and therefore different pixel resolutions.	47
GMTF	General Material Transfer Function	63, 65
GPU	The Graphics Processing Unit (GPU) is a processing unit that is highly specialised for image processing tasks.	15, 53, 56
Hessian	The Hessian is a matrix holding all second partial derivatives of a multi-dimensional function and is equal to the transposed Jacobian of the gradient.	46
host	The host is the central managing device in OpenCL that sends commands to connected devices or other secondary systems.	54
image	In image registration, the *image* is referred to as the image that is transformed in order to match the template.	45
kernel	A kernel is one logical unit of an OpenCL program. One instance of a kernel can be run on many working elements at the same time, but only one kernel can be run at a time per working element.	56

Notation	Description	Page List
MCP	A Micro-Channel-Plate (MCP) is a structure with several parallel channels that are microfabricated. MCPs are used to create structured scintillators in neutron imaging to restrict the movement of secondary particles to the inside of one single micro-channel and therefore enhance resolution.	21
MEA	The Membrane Electrode Assembly (MEA) is the active stack inside a fuel cell consisting of the membrane and the contacting electrodes and if present the gas-diffusion layer.	84–86
OpenCL	The Open Computing Language (OpenCL) is a framework for unified programming on heterogeneous computing system with one universal language.	53–58
optical axis	The optical axis is defined as the path of a ray that traverses an optical element without being refracted. This often is the center of a lens.	24–28, 30, 31
PEMFC	A Proton Exchange Membrane Fuel Cell (PEMFC) is a device that converts chemical energy into electrical energy. PEMFCs usually have a polymer membrane.	83, 84
PREM	Practical REsolution Measure	66, 68
processor	The general term processor refers to any electronic circuit that consists of data input, output and processing elements.	51
PSF	The Point Spread Function (PSF) is a function that describes the diffraction pattern of one single light source when passing an optical system.	15, 16, 32–34, 65, 66, 71, 75, 77–80, 111

Notation	Description	Page List
reverse-bias	Reverse-bias is the direction of the voltage applied to a pn-junction that increases the depletion region.	11
semi-conductors	Semi-conductors are materials where conduction can occur due to electronic states in the conduction bands resulting from excitation from the valence band.	11
spectral imaging	Spectral imaging generally refers to all imaging modalities where more than one energy spectrum of incident radiation is used.	10
STED	STimulated Emission Depletion (STED) is a super resolution technique with a scanning approach.	63–65, 80
steepest descent image	The steepest descent image refers to the gradient of an image under a warp. The term includes the fact, that the steepest descent of a multi-variable and differentiable function decreases fastest in the direction of the gradient.	46
STORM	STochastic Optical Reconstruction Microscopy (STORM) is a super resolution imaging technique with a full field approach.	65, 78–80
super resolution	Super resolution is a term, comprising all imaging techniques in which the achieved resolution is higher than fundamental classical limits such as the diffraction limit.	63, 65–68, 71, 78–80
template	In image registration, the template is the version of an image to which another image is matched to as closely as possible.	45
valence band	The valence band is the highest occupied energy level in a bulk solid at 0 K.	11
warp	A warp refers to an image under a certain applied image transform.	46

Notation	Description	Page List

Bibliography

[Agner, 2017] Agner, F. (2017). Lists of instruction latencies, throughputs and micro-operation breakdowns for Intel, AMD and VIA CPUs. Technical report, Technical University of Denmark. Available from: `http://www.agner.org/optimize/instruction_tables.pdf`.

[Alekhin et al., 2017] Alekhin, M. S., Patton, G., Dujardin, C., Douissard, P. A., Lebugle, M., Novotny, L., and Stampanoni, M. (2017). Stimulated scintillation emission depletion X-ray imaging. *Optics Express*, 25(2):654.

[Als-Nielsen and McMorrow, 2011] Als-Nielsen, J. and McMorrow, D. (2011). *Elements of Modern X-Ray Physics.* John Wiley & Sons Ltd., West Sussex, 2 edition.

[Anderson et al., 2016] Anderson, I. S., Andreani, C., Carpenter, J. M., Festa, G., Gorini, G., Loong, C. K., and Senesi, R. (2016). Research opportunities with compact accelerator-driven neutron sources. *Physics Reports*, 654:1–58.

[Baker and Matthews, 2004] Baker, S. and Matthews, I. (2004). Lucas-Kanade 20 Years On : A Unifying Framework. *International Journal of Computer Vision*, 56(3):221–255.

[Basden et al., 2003] Basden, A. G., Haniff, C. A., and Mackay, C. D. (2003). Photon counting strategies with low-light-level CCDs. *Monthly Notices of the Royal Astronomical Society*, 345(3):985–991.

[Bearden, 1967] Bearden, J. A. (1967). X-ray wavelengths. *Reviews of Modern Physics*, 39(1):78.

[Bell, 2012] Bell, Z. W. (2012). Scintillation Counters. In Grupen, C. and Buvat, I., editors, *Handbook of Particle Detection and Imaging*, pages 350–374.

[Berger et al., 2010] Berger, M., Hubbell, J., Seltzer, S., Chang, J., Coursey, J., Sukumar, R., Zucker, D., and Olsen, K. (2010). XCOM: Photon Cross Sections Database. Available from: `https://www.nist.gov/pml/xcom-photon-cross-sections-database` [accessed on 2017-04-11].

[Betzig et al., 2006] Betzig, E., Patterson, G. H., Sougrat, R., Lindwasser, O. W., Olenych, S., Bonifacino, J. S., Davidson, M. W., Lippincott-schwartz, J., and Hess, H. F. (2006). Imaging Intracellular Fluorescent Proteins at Nanometer Resolution. *Science*, 313:1642–1646.

[Blasse and Grabmaier, 1994] Blasse, G. and Grabmaier, B. (1994). *Luminescent Materials*. Springer-Verlag, Berlin Heidelberg.

[Breitwieser et al., 2016] Breitwieser, M., Moroni, R., Schock, J., Schulz, M., Schillinger, B., Pfeiffer, F., Zengerle, R., and Thiele, S. (2016). Water management in novel direct membrane deposition fuel cells under low humidification. *International Journal of Hydrogen Energy*, 41(26).

[Buzug, 2008] Buzug, T. M. (2008). *Computed Tomography: From Photon Statistics to Modern Cone-Beam CT*. Springer-Verlag Berlin Heidelberg.

[Calzada et al., 2009] Calzada, E., Gruenauer, F., Mühlbauer, M., Schillinger, B., and Schulz, M. (2009). New design for the ANTARES-II facility for neutron imaging at FRM II. *Nuclear Instruments and Methods in Physics Research, Section A: Accelerators, Spectrometers, Detectors and Associated Equipment*, 605(1-2):50–53.

[Cartier et al., 2016] Cartier, S., Kagias, M., Bergamaschi, A., Wang, Z., Dinapoli, R., Mozzanica, A., Ramilli, M., Schmitt, B., Brückner, M., Fröjdh, E., Greiffenberg, D., Mayilyan, D., Mezza, D., Redford, S., Ruder, C., Schädler, L., Shi, X., Thattil, D., Tinti, G., Zhang, J., and Stampanoni, M. (2016). Micrometer-resolution imaging using MÖNCH: Towards G2-less grating interferometry. *Journal of Synchrotron Radiation*, 23(6):1462–1473.

[Chandrakasan et al., 1995] Chandrakasan, A. P., Potkonjak, M., Mehra, R., Rabaey, J., and Brodersen, R. W. (1995). Optimizing power using transformations. *IEEE Transactions on Computer-Aided Design of Integrated Circuits and Systems*, 14(1):12–31.

[Cherepy, 2011] Cherepy, N. J. (2011). Scintillator Materials. Technical report, Lawrence Livermore National Laboratory, CA 94550.

[Chewpraditkul et al., 2009] Chewpraditkul, W., Swiderski, L., Moszynski, M., Szczesniak, T., Syntfeld-Kazuch, A., Wanarak, C., and Limsuwan, P. (2009). Scintillation properties of LuAG:Ce, YAG:Ce and LYSO:Ce crystals for gamma-ray detection. *IEEE Transactions on Nuclear Science*, 56(6):3800–3805.

[Cooke-Yarborough, 1998] Cooke-Yarborough, E. (1998). Some early transistor applications in the UK. *Engineering Science and Education Journal*, 7(3):100–106.

[Curry et al., 1990] Curry, T. S., Dowdey, J. E., and Murry, R. C. (1990). *Christensen's Physics of Diagnostic Radiology*. M - Medicine Series. Lea & Febiger.

[Derenzo et al., 2017] Derenzo, S., Boswell, M., Weber, M., and Brennan, K. (2017). Scintillation Properties. Available from: `http://scintillator.lbl.gov/` [accessed on 2018-02-26].

[Dittus and Lämmerzahl, 2007] Dittus, H. and Lämmerzahl, C. (2007). Tests of the weak equivalence principle for charged particles in space. *Advances in Space Research*, 39(2):244–248.

[Elder et al., 1947] Elder, F., Gurewitsch, A., Langmuir, R., and Pollock, H. (1947). Radiation from Electrons in a Synchrotron. *Physical Review*, 71:829–830.

[Engels, 2011] Engels, R. (2011). *Entwicklung eines Prototypen für einen großflächigen Szintillationsdetektor zur Detektion thermischer Neutronen.* PhD thesis, Albert-Ludwigs-Universität Freiburg.

[Feynman et al., 1963] Feynman, R. P., Leighton, R. B., and Sands, M. (1963). The Feynman Lectures on Physics, Volume I. Available from: `http://www.feynmanlectures.caltech.edu/I_toc.html` [accessed on 2017-11-21].

[Flores et al., 2015] Flores, L., Vidal, V., and Verdú, G. (2015). System matrix analysis for computed tomography imaging. *PLoS ONE*, 10(11):1–12.

[FRM2, 2017] FRM2 (2017). Installations in the pool. Available from: `https://www.frm2.tum.de/en/the-neutron-source/reactor/installations-in-the-pool/` [accessed on 2017-04-13].

[Gao and Blumensath, 2017] Gao, Y. and Blumensath, T. (2017). Distributed Computation of Linear Inverse Problems with Application to Computed Tomography. pages 1–13.

[Gilmore, 2008] Gilmore, G. R. (2008). Practical Gamma-Ray Spectrometry. Number 1980, pages 25–38. John Wiley & Sons Ltd., 2nd edition.

[Gilmore, 1992] Gilmore, R. (1992). *Single Particle Detection and Measurement.* Taylor & Francis, London - Washington, DC.

[Glodo et al., 2008] Glodo, J., Van Loef, E. V. D., Higgins, W. M., and Shah, K. S. (2008). Mixed lutetium iodide compounds. *IEEE Transactions on Nuclear Science*, 55(3):1496–1500.

[Greb, 2016] Greb, C. (2016). From infinity optics to the infinity port. In *Optik&Photonik*, pages 34–37, Weinheim. Wiley-VCH Verlag GmbH & Co. KGaA.

[Hecht, 2001] Hecht, E. (2001). *Optik.* Oldenbourg Verlag München Wien, München, Wien, Oldenbourg.

[Hell, 2005] Hell, S. W. (2005). New law in light microscopy allows for unprecedented resolution. Technical report, Max-Planck Institut für biophysikalische Chemie. Available from: `http://www.mpibpc.mpg.de/327643/research_report_815357`.

[Hell and Wichmann, 1994] Hell, S. W. and Wichmann, J. (1994). Breaking the diffraction resolution limit by stimulated emission: Stimulated-Emission-Depletion Fluorescence Microscopy. *Optics Letters*, 19(11):780–782.

[Hoheisel et al., 2004] Hoheisel, M., Giersch, J., and Bernhardt, P. (2004). Intrinsic spatial resolution of semiconductor X-ray detectors: a simulation study. *Nuclear Instruments and Methods in Physics Research*, 531:75–81.

[Huang et al., 2012] Huang, B., Babcock, H., and Zhuang, X. (2012). Breaking the Diffraction Barrier: Super-Resolution Imaging of Cells. *Cell*, 143(7):1047–1058.

[Huang et al., 2008] Huang, B., Wang, W., Bates, M., and Zhuang, X. (2008). Three-Dimensional Super-Resolution Imaging by Stochastic Optical Reconstruction Microscopy. *Science*, 319:810–813.

[Hubbell et al., 2000] Hubbell, J. H., Briggs, E. A., Brown, R. T., Cromer, D. T., and Howerton, R. J. (2000). Atomic form factors, incoherent scattering functions, and photon scattering cross sections. 471(1975).

[Huston, 2008] Huston, P. J. (2008). Phy192 Lecture Notes. Available from: `http://www.pa.msu.edu/~huston/phy192_s08/` [accessed on 2017-01-01].

[Jain et al., 2010] Jain, A., Kuhls-Gilcrist, A. T., Gupta, S. K., Bednarek, D. R., and Rudin, S. (2010). Generalized two-dimensional (2D) linear system analysis metrics (GMTF, GDQE) for digital radiography systems including the effect of focal spot, magnification, scatter, and detector characteristics. *Proc. SPIE Medical Imaging*, 7622(76220K):1–10.

[Jakubek et al., 2009] Jakubek, J., Schmidt-Wellenburg, P., Geltenbort, P., Platkevic, M., Plonka-Spehr, C., Solc, J., and Soldner, T. (2009). A coated pixel device TimePix with micron spatial resolution for UCN detection. *Nuclear Instruments and Methods in Physics Research Section A: Accelerators, Spectrometers, Detectors and Associated Equipment*, 600(3):651–656. Available from: `http://linkinghub.elsevier.com/retrieve/pii/S0168900208019220`.

[Jones et al., 2001] Jones, E., Oliphant, T., Peterson, P., and Others (2001). SciPy: Open source scientific tools for Python. Available from: `http://www.scipy.org`.

[Kalender, 2005] Kalender, W. (2005). *Computed Tomography*. Publicis Publishing, Erlangen.

[Khronos Group, 2015] Khronos Group (2015). The OpenCL Specification. Technical report. Available from: `https://www.khronos.org/registry/OpenCL/specs/opencl-2.0.pdf`.

[Klingele et al., 2015] Klingele, M., Breitwieser, M., Zengerle, R., and Thiele, S. (2015). Direct deposition of proton exchange membranes enabling high performance hydrogen fuel cells. *J. Mater. Chem. A*, 3(21):11239–11245.

[Klöckner et al., 2012] Klöckner, A., Pinto, N., Lee, Y., Catanzaro, B., Ivanov, P., and Fasih, A. (2012). PyCUDA and PyOpenCL: A scripting-based approach to GPU run-time code generation. *Parallel Computing*, 38(3):157–174.

[Knorpp and Templin, 2009] Knorpp, T. and Templin, M. F. (2009). Method of the year 2008. *Nature Methods*, 6(1):1.

[Knuth, 1997] Knuth, D. E. (1997). *The Art of Computer Programming, Volume 2 (3rd Ed.): Seminumerical Algorithms*. Addison-Wesley Longman Publishing Co., Inc., Boston, MA, USA.

[Koch et al., 1998] Koch, A., Raven, C., Spanne, P., and Snigirev, A. (1998). X-ray imaging with submicrometer resolution employing transparent luminescent screens. *Journal of the Optical Society of America A*, 15(7):1940.

[Kühlke, 2011] Kühlke, D. (2011). *Optik*. Verlag Harri Deutsch, Frankfurt am Main.

[Levinthal, 2009] Levinthal, D. (2009). Performance Analysis Guide for Intel ® Core ™ i7 Processor and Intel ® Xeon ™ 5500 processors. Technical report. Available from: `https://software.intel.com/sites/products/collateral/hpc/vtune/performance_analysis_guide.pdf`.

[Li et al., 2006] Li, H., Schillinger, B., Calzada, E., Yinong, L., and Muehlbauer, M. (2006). An adaptive algorithm for gamma spots removal in CCD-based neutron radiography and tomography. *Nuclear Instruments and Methods in Physics Research*, 564(1):405–413.

[Lucas and Kanade, 1981] Lucas, B. D. and Kanade, T. (1981). An iterative image registration technique with an application to stereo vision. In *Proceedings of the 7th International Joint Conference on Artificial Intelligence (IJCAI)*, volume 2, pages 674–679.

[Maier et al., 2017] Maier, D., Schock, J., and Pfeiffer, F. (2017). Dual-energy micro-CT with a dual-layer, dual-color, single-crystal scintillator. *Optics Express*, 25(6).

[Mares et al., 2004] Mares, J. A., Beitlerova, A., Nikl, M., Solovieva, N., D'Ambrosio, C., Blazek, K., Maly, P., Nejezchleb, K., and de Notaristefani, F. (2004). Scintillation response of Ce-doped or intrinsic scintillating crystals in the range up to 1MeV. *Radiation Measurements*, 38(4-6):353–357.

[Martin and Koch, 2006] Martin, T. and Koch, A. (2006). Recent developments in X-ray imaging with micrometer spatial resolution. *Journal of Synchrotron Radiation*, 13(2):180–194.

[Matsui and Ono, 1985] Matsui, H. and Ono, K. (1985). A uniform focal spot X-ray tube with improved MTF and kW rating. *Radiology*, 156(1):227–30.

[Moore, 1965] Moore, G. E. (1965). Cramming more components onto integrated circuits. *Electronics*, 38(8).

[Moore, 1975] Moore, G. E. (1975). Progress In Digital Integrated Electronics. *IEDM Tech. Digest*, pages 11–13.

[Mühlbauer et al., 2017] Mühlbauer, M. J., Bücherl, T., Genreith, C., Knapp, M., Schulz, M., Söllradl, S., Wagner, F. M., and Ehrenberg, H. (2017). The Thermal Neutron Beam Option for NECTAR at MLZ. *Physics Procedia*, 88(September 2016):148–153.

[Munshi et al., 2012] Munshi, A., Gaster, B., Mattson, T. G., Fung, J., and Ginsburg, D. (2012). *OpenCL Programming Guide*. Addison-Wesley.

[Nikl, 2006] Nikl, M. (2006). Scintillation detectors for x-rays. *Measurement Science and Technology*, 17(4):R37–R54.

[Nvidia, 2011] Nvidia (2011). OpenCL Best Practices Guide. Technical report.

[ON Semiconductor, 2014] ON Semiconductor (2014). AND9192/D Estimating Dark Current from Operating Temperature. Technical report. Available from: `http://www.onsemi.com/pub/Collateral/AND9192-D.PDF`.

[Passon and Grebe-Ellis, 2016] Passon, O. and Grebe-Ellis, J. (2016). Note on the classification of super-resolution in far-field microscopy and information theory. *Journal of the Optical Society of America*, 33(7):B31.

[Pedrotti et al., 2008] Pedrotti, F., Pedrotti, L., Bausch, W., and Schmidt, H. (2008). *Optik für Ingenieure*. Springer-Verlag, Berlin Heidelberg.

[Petrantonaki et al., 1999] Petrantonaki, M., Kappas, C., Efstathopoulos, E. P., Theodorakos, Y., and Panayiotakis, G. (1999). Calculating shielding requirements in diagnostic X-ray departments. *British Journal of Radiology*, 72(FEB.):179–185.

[PicoQuant, 2018] PicoQuant (2018). Comparison of confocal and superresolution microscopy. Available from: `https://www.picoquant.com/images/uploads/application_images/7356/titelbild_sted1.jpg` [accessed on 2018-02-22].

[Prade, 2017] Prade, F. (2017). *Grating based X-ray dark field imaging*. Phd thesis, Technische Universität München.

[Prade et al., 2015] Prade, F., Yaroshenko, A., Herzen, J., and Pfeiffer, F. (2015). Short-range order in mesoscale systems probed by X-ray grating interferometry. *EPL*, 112(6).

[Quirin et al., 2012] Quirin, S., Pavani, S. R. P., and Piestun, R. (2012). Optimal 3D single-molecule localization for superresolution microscopy with aberrations and engineered point spread functions. *Proceedings of the National Academy of Sciences*, 109(3):675–679.

[Ram et al., 2007] Ram, S., Prabhat, P., Chao, J., Ward, E. S., and Ober, R. J. (2007). Resolution beyond Rayleigh's criterion: A modern resolution measure with applications to single molecule imaging. *2007 IEEE Dallas Engineering in Medicine and Biology Workshop, DEMBS*, pages 110–113.

[Ram et al., 2006] Ram, S., Ward, E. S., and Ober, R. J. (2006). Beyond Rayleigh's criterion: A resolution measure with application to single-molecule microscopy. *Proceedings of the National Academy of Sciences*, 103(12):4457–4462.

[Rangacharyulu, 2014] Rangacharyulu, C. (2014). *Physics of nuclear radiations*. Taylor & Francis, Boca Raton.

[Renker and Lorenz, 2009] Renker, D. and Lorenz, E. (2009). Advances in solid state photon detectors. *Journal of Instrumentation*, 4(4).

[Robbins and Hadwen, 2003] Robbins, M. S. and Hadwen, B. J. (2003). The noise performance of electron multiplying charge-coupled devices. *IEEE Transactions on Electron Devices*, 50(5):1227–1232.

[Rohrlich, 2001] Rohrlich, F. (2001). The correct equation of motion of a classical point charge. *Physics Letters A*, 283(5):276–278.

[Russell, 1990] Russell, G. J. (1990). Spallation Physics - An Overview. *International Collaboration on Advanced Neutron Sources KEK. Tsukuba*, pages 291–299.

[Rust et al., 2006] Rust, M. J., Bates, M., and Zhuang, X. W. (2006). Sub-diffraction-limit imaging by stochastic optical reconstruction microscopy (STORM). *Nat Methods*, 3(10):793–795.

[Schock and Schulz, 2018] Schock, J. and Schulz, M. (2018). GPU Accelerated Image Processing in CCD-Based Neutron Imaging. pages 1–11.

[Schoonjans et al., 2011] Schoonjans, T., Brunetti, A., Golosio, B., del Rio, M. S., Solé, V. A., Ferrero, C., and Vincze, L. (2011). The xraylib library for X-ray–matter interactions. Recent developments. *Spectrochimica Acta Part B: Atomic Spectroscopy*, 66(11–12):776–784.

[Schreyer, 2008] Schreyer, A. (2008). Physical Properties of Photons and Neutrons. In *Neutrons and Synchrotron Radiation in Engineering Materials Science*, chapter 4, pages 79–89. Wiley-VCH Verlag GmbH & Co. KGaA.

[Schulz and Schillinger, 2015] Schulz, M. and Schillinger, B. (2015). ANTARES: Cold neutron radiography and tomography facility. *Journal of large-scale research facilities JLSRF*, 1:A17.

[Sears, 1992] Sears, V. (1992). Neutron scattering lengths and cross sections. *Neutron News*, 3(3):26–37.

[Siegmund et al., 2007] Siegmund, O. H., Vallerga, J. V., Tremsin, A. S., Mcphate, J., and Feller, B. (2007). High spatial resolution neutron sensing microchannel plate detectors. 576:178–182.

[SiemensAG, 2017] SiemensAG (2017). Simulation of X-ray Spectra. Available from: `https://www.oem-xray-components.siemens.com/x-ray-spectra-simulation` [accessed on 2017-03-23].

[Silfies et al., 2017] Silfies, J. S., Schwartz, S. A., and Davidson, M. W. (2017). The Diffraction Barrier in Optical Microscopy. Technical report, MicroscopyU. Available from: `https://www.microscopyu.com/techniques/super-resolution/the-diffraction-barrier-in-optical-microscopy`.

[Soker and Harpaz, 2004] Soker, N. and Harpaz, A. (2004). Radiation from a charge supported in a gravitational field. *General Relativity and Gravitation*, 36(2):315–330.

[Sprawls, 1996] Sprawls, P. (1996). Physical Principles of Medical Imaging. 2nd ed. *Medical Physics Publishing*.

[Spring and Davidson, 2017] Spring, K. R. and Davidson, M. W. (2017). Depth of Field and Depth of Focus. Technical report, MicroscopyU. Available from: `https://www.microscopyu.com/microscopy-basics/depth-of-field-and-depth-of-focus`.

[Sridhar et al., 2001] Sridhar, P., Perumal, R., Rajalakshmi, N., Raja, M., and Dhathathreyan, K. S. (2001). Humidification studies on polymer electrolyte membrane fuel cell. *Journal of Power Sources*, 101(1):72–78.

[Stallinga and Rieger, 2010] Stallinga, S. and Rieger, B. (2010). Accuracy of the Gaussian Point Spread Function model in 2D localization microscopy. *Optics Express*, 18(24):24461.

[Stoud, 1971] Stoud, A. H. (1971). *Approximate Calculation of Multiple Integrals*. Prentice-Hall, Inc., New Jersey.

[Thompson et al., 2009] Thompson, A., Attwood, D., Gullikson, E., Howells, M., Kim, K.-J., Kirz, J., Kortright, J., Lindau, I., Liu, Y., Pianetta, P., Robinson, A., Scofield, J., Underwood, J., Williams, G., and Winick, H. (2009). *X-ray Data Booklet*. Lawrence Berkeley National Laboratory, University of California, Berkeley, California, third edition.

[Wagner, 2017] Wagner, V. (2017). Introduction to Nuclear Spectroscopy [lecture notes]. Available from: `http://hp.ujf.cas.cz/~wagner/prednasky/spektroskopie/osnovaen.html` [accessed on 2017-04-06].

[Widenhorn et al., 2002] Widenhorn, R., Blouke, M. M., Weber, A., Rest, A., and Bodegom, E. (2002). Temperature dependence of dark current in a CCD. *Proc. SPIE Vol. 4669*, 4669(April):193–201.

[Wikimedia Commons, 2015] Wikimedia Commons (2015). Kugel-kappe-s. Available from: `https://commons.wikimedia.org/wiki/File:Kugel-kappe-s.svg` [accessed on 2017-05-23].

[Wikimedia Commons, 2017] Wikimedia Commons (2017). Beugungsscheibchen. Available from: `https://commons.wikimedia.org/wiki/File:Beugungsscheibchen.k.720.jpg` [accessed on 2018-01-23].

List of Publications

[1] J. Schock and M. Schulz. GPU Accelerated Image Processing in CCD-Based Neutron Imaging. *Journal of Imaging*, pages 1–11, 2018.

[2] D.S. Maier, J. Schock, and F. Pfeiffer. Dual-energy micro-CT with a dual-layer, dual-color, single-crystal scintillator. *Optics Express*, 25(6), 2017.

[3] M. Breitwieser, R. Moroni, J. Schock, M. Schulz, B. Schillinger, F. Pfeiffer, R. Zengerle, and S. Thiele. Water management in novel direct membrane deposition fuel cells under low humidification. *International Journal of Hydrogen Energy*, 41(26), 2016.

[4] K. Willer, K. Scherer, E. Braig, S. Ehn, J. Schock, J. Wolf, L. Birnbacher, M. Chabior, D. Mayr, S. Grandl, A. Sztrókay-Gaul, K. Hellerhof, M. Reiser, F. Pfeiffer, and J. Herzen. Classification of the micromorphology of breast calcifications in x-ray dark-field mammography. In *Progress in Biomedical Optics and Imaging - Proceedings of SPIE*, volume 10132, 2017.

[5] K. Scherer, E. Braig, S. Ehn, J. Schock, J. Wolf, L. Birnbacher, M. Chabior, J. Herzen, D. Mayr, S. Grandl, A. Sztrókay-Gaul, K. Hellerhoff, and F. Pfeiffer. Improved Diagnostics by Assessing the Micromorphology of Breast Calcifications via X-Ray Dark-Field Radiography. *Scientific Reports*, 6, 2016.

[6] L. Rossetti, L. A. Kuntz, E. Kunold, J. Schock, K. W. Müller, H. Grabmayr, J. Stolberg-Stolberg, F. Pfeiffer, S. A. Sieber, R. Burgkart, and A. R. Bausch. The microstructure and micromechanics of the tendon-bone insertion. *Nature Materials*, 16(6):664–670, 2017.

[7] T. Kovačević, V. Wiedmeyer, J. Schock, A. Voigt, F. Pfeiffer, K. Sundmacher, and H. Briesen. Disorientation angle distribution of primary particles in potash alum aggregates. *Journal of Crystal Growth*, 467:93–106, 2017.

[8] M. Willner, G. Fior, M. Marschner, L. Birnbacher, J. Schock, C. Braun, A.A. Fingerle, P.B. Noël, E.J. Rummeny, F. Pfeiffer, and J. Herzen. Phase-contrast Hounsfield units of fixated and non-fixated soft-tissue samples. *PLoS ONE*, 10(8), 2015.

[9] T. Kovačević, J. Schock, F. Pfeiffer, and H. Briesen. Shape identification of primary particles in potash alum aggregates using three-dimensional tomography data. *Crystal Growth and Design*, 16(5):2685–2699, 2016.

Appendix

A.1 Constants for Stoud's integration scheme

This section is meant as a reference for the constants and weights used in the numerical integration scheme. All information in this section is adapted from [Stoud, 1971] and more information about the establishment of the used formulas as well as error calculations can be found there. A square in R_2 can be defined as

$$R_{\text{square}} = \{x_i | -1 \leq x_i \leq 1 \qquad i \in [1,2]\} \tag{2}$$

with the monomial integral

$$I_{\alpha_1,\alpha_2} = \iint\limits_{R_{\text{square}}} w(x_1,x_2) x_1^{\alpha_1} x_2^{\alpha_2} dx_1\, dx_2, \tag{3}$$

where w is the weight function, which is non-negative and can be evaluated to be

$$I_{0,0} = \iint\limits_{R_{\text{square}}} w(x_1,x_2) dx_1\, dx_2, = V = 2^n = 4. \tag{4}$$

For a square as defined in Equation 2, Equation 3 can be approximated in the form

$$I_{\alpha_1,\alpha_2} \simeq \sum_{i=1}^{N} B_i f(v_{i,1}, v_{i,2}), \tag{5}$$

where the v_i are the *nodes* of the formula, and B_i are the *coefficients*, which are not dependant on f. According to formula $C_2 : 7-3$ [Stoud, 1971, p.253 f.] the nodes of the formula are

$$v_i = [[0,0],[r,0]_{FS},[s,t]_{FS}], \tag{6}$$

where the subscript FS denotes a *fully symmetrical* set of points, where $[a,b]_{FS}$ includes all permutations of $[\pm a, \pm b]$ and the plus and minus sign is varied independently, leading to a node count of 13. The coefficients are constant per set, and in the same order as in the equation above:

$$B_i = \left(\frac{1}{81}V, \frac{49}{324}V, \frac{31}{649}V\right). \tag{7}$$

The values for r, s and t are defined as

$$r^2 = \frac{12}{35} \qquad s^2 = \frac{93+3\sqrt{186}}{155} \qquad t^2 = \frac{93-3\sqrt{186}}{155}. \tag{8}$$

The coefficients and nodes are visualised in Figure 8.

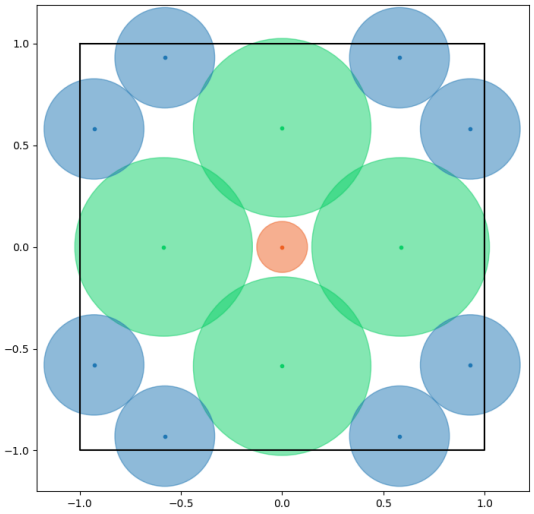

Figure 8: Schematic drawing of the nodes v_i and the coefficients B_i in the used Stroud scheme. The diameter of each circle corresponds to its weight. The red circle is the central point, the green circles correspond to $[r, 0]_{\mathrm{FS}}$ and the blue circles to $[s, t]_{\mathrm{FS}}$.

A.2 Reverse case

Table 2 gives the results for the calculation of the reverse case, meaning the scintillator-substrate complex being placed bottom up in the beam, so that the substrate layer faces the source and the scintillator layer faces the detector.

A.3 Mathematical functions

A.3.1 The Klein-Nishina equation

The Klein-Nishina equation can be used to calculate the differential cross-section of the photon-electron interaction in the Compton effect. The cross-section σ of a scattered photon with the incident energy E_0 inside the solid angle element $d\Omega$ is

$$\frac{\mathrm{d}\sigma}{\mathrm{d}\Omega} = \frac{\frac{1}{2{r_0}^2}\left[1+\cos(\theta)^2\right]}{1+2\epsilon\sin(\frac{\theta}{2})^2}\left(1+\frac{4\epsilon^2\sin(\frac{\theta}{2})^4}{\left[1+\cos(\theta)^2\right]\left[1+2\epsilon\sin(\frac{\theta}{2})^2\right]}\right), \tag{9}$$

where ϵ is the energy fraction $\epsilon = \frac{E_0}{m_e c^2}$. This equation can be integrated over all angles and leads to the energy dependant formula [Huston, 2008]

$$\sigma = 2\pi {r_0}^2\left(\frac{1+\epsilon}{\epsilon}\left[\frac{2+2\epsilon}{1+2\epsilon}-\frac{\ln(1+2\epsilon)}{\epsilon}\right]+\frac{\ln(1+2\epsilon)}{2\epsilon}-\frac{1+\epsilon}{(1+2\epsilon)^2}\right). \tag{10}$$

Table 2: Light collection efficiency for the different objectives in the reverse configuration. Listed are the values for the maximal capturing angle in air $\alpha_{\mathrm{max,air}}$, the corresponding opening angle in the scintillator material α_{scin}, the transmission T with Fresnel reflection and the total capture ratio for all effects combined. Together with the scintillator yield the number of photons, that can be captured per one 60 kV gamma is calculated.

ID	$\alpha_{\mathrm{max,air}}$ [°]	α_{scin}[°]	T[%]	Capture ratio [%]	N_{photons}
1	14.48	7.81	91.25	0.42	3
2	26.74	14.16	91.22	1.38	11
3	48.59	24.05	94.88	4.12	31 ± 1

A.3.2 Delta function

The Dirac delta function δ is not a real function in the mathematical sense, instead it is most often defined via its characteristics. The two most important characteristics are its behaviour around the origin and the normalization:

$$\delta(x) = \begin{cases} \infty & \text{for } x = 0 \\ 0 & \text{elsewhere} \end{cases} \tag{11}$$

and

$$\int_{-\infty}^{\infty} \delta(x)\mathrm{d}x = 1. \tag{12}$$

Another important characteristic is the sifting property

$$\int f(y)\delta(x-y)\mathrm{d}y = f(x). \tag{13}$$

A.4 Transform matrices

This section describes the transformation matrices used in the image registration. If possible, all matrices are chosen in such a way, that the zero vector of the same length as the vector $\vec{p}$ is the identity. The Jacobian is defined as

$$J = \begin{bmatrix} \frac{\partial X}{\partial p_0} & \frac{\partial X}{\partial p_1} & \frac{\partial X}{\partial p_2} \\ \\ \frac{\partial Y}{\partial p_0} & \frac{\partial Y}{\partial p_1} & \frac{\partial Y}{\partial p_2} \end{bmatrix}, \tag{14}$$

where X and Y are defined as in Equation 4.6. The subscripted values p_n are the entries of $\vec{p}$ (zero-indexed).

RotationCenter

The vector, defining the degrees of freedom is

$$\vec{p} = [\theta], \tag{15}$$

where θ is the angle of rotation around the image center, positive being in the counter-clockwise direction. The transformation matrix is given as

$$\begin{bmatrix} \cos(p_0) & -\sin(p_0) & -x_c\cos(p_0) + y_c\sin(p_0) + x_c \\ \sin(p_0) & \cos(p_0) & -x_c\sin(p_0) - y_c\cos(p_0) + y_c \\ 0 & 0 & 1 \end{bmatrix}, \tag{16}$$

where x_c and y_c are the coordinates of the image center. The Jacobian becomes

$$\begin{bmatrix} \sin(p_0)(x_c - x) + \cos(p_0)(y_c - y) \\ \sin(p_0)(y_c - y) - \cos(p_0)(x_c - x) \end{bmatrix}. \tag{17}$$

Shift

The vector, defining the degrees of freedom is

$$\vec{p} = [x_s, y_s], \tag{18}$$

where x_s and y_s are the shifts along each respective axis. The transformation matrix then becomes

$$\begin{bmatrix} 1 & 0 & p_0 \\ 0 & 1 & p_1 \\ 0 & 0 & 1 \end{bmatrix}. \tag{19}$$

The Jacobian becomes

$$\begin{bmatrix} 1 & 0 & 0 \\ 0 & 1 & 0 \end{bmatrix}. \tag{20}$$

IscoscaleShift

The vector, defining the degrees of freedom is

$$\vec{p} = [s, x_s, y_s], \tag{21}$$

where x_s and y_s are the shifts along each respective axis and s is the scale factor along both axes. The transformation matrix then becomes

$$\begin{bmatrix} 1 + p_0 & 0 & p_1 \\ 0 & 1 + p_0 & p_2 \\ 0 & 0 & 1 \end{bmatrix}. \tag{22}$$

The Jacobian becomes

$$\begin{bmatrix} x & 1 & 0 \\ y & 0 & 1 \end{bmatrix}. \tag{23}$$

Rotation

The vector, defining the degrees of freedom is

$$\vec{p} = [\theta, x_c, y_c], \tag{24}$$

where x_c and y_c are the coordinates of the center of rotation and θ is the rotation angle, which is measured positive as counter-clockwise. The transformation matrix then becomes

$$\begin{bmatrix} \cos(p_0) & -\sin(p_0) & -p_1\cos(p_0) + p_2\sin(p_0) + p_1 \\ \sin(p_0) & \cos(p_0) & -p_1\sin(p_0) - p_2\cos(p_0) + p_2 \\ 0 & 0 & 1 \end{bmatrix}. \tag{25}$$

The Jacobian becomes

$$\begin{bmatrix} \sin(p_0)(p_1 - x) + \cos(p_0)(p_2 - y) & 1 - \cos(p_0) & \sin(p_0) \\ \cos(p_0)(x - p_1) + \sin(p_0)(p_2 - y) & -\sin(p_0) & 1 - \cos(p_0) \end{bmatrix}. \tag{26}$$

As in this case, the inverse functions are not trivial, they will be mentioned. To get p out of the transformation matrix H, one can use:

$$\vec{p} = \begin{cases} [0, 0, 0] & \text{if } H_{[0,0]} = 1; \\ \begin{bmatrix} \arccos(H_{[0,0]}) \\ \frac{H_{[0,2]} - H_{[1,0]} \cdot p_2}{1 - H_{[0,0]}} \\ \frac{H_{[1,2]}\left(1 - H_{[0,0]}\right) + H_{[0,1]}H_{[1,0]}}{{H_{[1,0]}}^2 + \left(1 - H_{[0,0]}\right)^2} \end{bmatrix}^\intercal & \text{otherwise.} \end{cases} \tag{27}$$

The notation $H_{[m,n]}$ is the element in row m and column n starting at zero to be compliant with the implementation in code.

A.5 Source code

This section lists the OpenCL kernels developed in this work and used for benchmarking.

A.5.1 Laplacian of Gaussian

```
__kernel void LoG(__read_only image3d_t d_image,
                  __read_only image3d_t d_coefficients,
                  __write_only image3d_t d_out_image,
                  int size,
                  int offset_x,
                  int offset_y)
{
// Laplacian Gaussian Kernel is:
```

```
9  int x_i = get_global_id(0)+offset_x;
10 int y_i = get_global_id(1)+offset_y;
11 int z   = get_global_id(2);
12 float gauss_laplacian = 0.0;
13 float weight = 0.0;
14 int get_x = 0;
15 int get_y = 0;
16 int offset = (size-1)/2;
17 for( int y = y_i-offset; y <= y_i+offset; y++)
18 {
19     get_x = 0;
20     for( int x = x_i-offset; x <= x_i+offset; x++)
21     {
22         weight = read_imagef(
23                 d_coefficients,
24                 sampler,
25                 (int4)(get_x,get_y,0,0)).s0;
26         gauss_laplacian += (read_imagef(
27                 d_image,
28                 sampler,
29                 (int4)(x, y, z, 0)).s0 * weight);
30         get_x++;
31     }
32     get_y++;
33 }
34
35 //Write the output value to the result Matrix:
36     write_imagef(
37         d_out_image,
38         (int4)(x_i,y_i,z,0),
39         (float4)(gauss_laplacian));
40 }
```

Listing 1: OpenCL kernel used for convolution of an input image with a coefficient image.

A.5.2 Adaptive median

```
1  __kernel void a_median(__read_only image3d_t d_image,
2                         __read_only image3d_t d_mask,
3                         __write_only image3d_t d_out_image,
4                         int t_low,
5                         int t_middle,
6                         int t_high,
7                         int offset_x,
8                         int offset_y)
9  {
10     __private int x = get_global_id(0)+offset_x;
11     __private int y = get_global_id(1)+offset_y;
```

```
12      __private int z = get_global_id(2);
13      __private int get_x, get_y, i, j;
14      __private int pos = 0;
15      __private float mask_value = read_imagef(
16          d_mask,
17          sampler,
18          (int4)(x,y,z,0)).s0;
19      __private int size;
20      if (mask_value < t_low)
21      {
22          size = 1;
23      }
24      else if (t_low<=mask_value && mask_value<t_middle)
25      {
26          size = 3;
27      }
28      else if (t_middle<=mask_value && mask_value<t_high)
29      {
30          size=5;
31      }
32      else if (mask_value>=t_high)
33      {
34          size=7;
35      }
36      __private int offset = (size-1)/2;
37      __private int window_size = size*size;
38      __private float window[81] = {0};
39      __private float temp, median;
40      __private float win_value;
41      //Getting all values from the window
42      for (get_x=-1*offset; get_x<=offset; get_x++)
43      {
44          for (get_y=-1*offset; get_y<=offset; get_y++)
45          {
46              win_value = read_imagef(
47                  d_image,
48                  sampler,
49                  (int4)(x+get_x,y+get_y,z,0)).s0;
50              window[pos] = win_value;
51              pos++;
52          }
53      }
54
55      //Sorting the array in ascending order
56      for(i=0; i<window_size-1; i++) {
57          for(j=0; j<window_size-i-1; j++) {
58              if(window[j] > window[j+1]) {
59                  // swap elements
60                  temp = window[j];
```

```
61                      window[j] = window[j+1];
62                      window[j+1] = temp;
63                  }
64              }
65          }
66          median = window[((size*size)-1)/2];
67          write_imagef(
68              d_out_image,
69              (int4)(x,y,z,0),
70              (float4)(median));
71
72  }
```

Listing 2: OpenCL kernel used for an adaptive median with 3 different levels and three corresponding thresholds.

Acknowledgments

Diese Arbeit ist das Ergebnis eines langen Weges, auf dem mich viele Menschen begleitet haben, denen ich an dieser Stelle meinen Dank aussprechen möchte:

Meinem Betreuer Franz Pfeiffer, der mir ermöglicht hat eine wunderschöne Zeit am Lehrstuhl E17 zu verbringen. Vielen Dank Franz für deinen unermüdlichen Einsatz für sowohl gute Forschung als auch gute Lehre, für das Engagement in der Finanzbeschaffung und die richtigen Worte zur richtigen Zeit.

Klaus Achterhold für konstruktive Diskussionen und Spinnereien, Gedankenanstöße und -austausch.

Riko Moroni, Matthias Breitwieser und Simon Thiele am IMTEK in Freiburg für die produktive, konstruktive und immer freundliche Zusammenarbeit im Projekt NeuRoTom.

Michael Schulz und Stefan Söllradl für die Zusammenarbeit mit ANTARES und NECTAR.

Julia Herzen und Marian Willner, die mich bei meinen ersten Versuchen als Wissenschaftler am E17 unterstützt und begleitet haben.

Martin Dierolf, Wolfgang Noichl, Sebastian Allner, Dieter Hahn und Andreas Fehringer, die mir ausführlich auch dumme Fragen beantwortet und mir bei Problemen rund um meinen und andere Computer geholfen haben.

Nelly, für ihre Engelsgeduld auch nach dreimal der gleichen Frage und für das Regeln jeglichen Papierkrams.

Meine Masteranden Daniel, Vitali und Zeeshan, die mich an Grenzen und darüber hinaus gebracht haben.

Das beste Großraumbüro der Welt. Elena, Marie, Pidassa, Markus, Karin, Marco, Markus, Florian, Friedrich, Mark, Simone, Christoph, Fabio, Johannes, Jolanda, Maite, Manuela, Rhiannon, Kaye, die Gustschin Brothers, Lukas, Thorsten, Stephan, Lorenz, Regine, Manuel, Lisa, Eva und alle die ich vergessen hab: was wäre das Leben ohne euch gewesen. Tischkickermatches, Biergarten, Nerf-gun-fights, durchgemachte Nächte, Schreibwochenenden... Wir haben viel gemeinsam gelacht und uns geärgert über die Physik im allgemeinen und im

speziellen. Dumme Wortspiele und schlaue Sprüche. Danke für über 7 Jahre tolle Zeit.

Dem Medizinerchor für die tolle Zeit und den Ausgleich neben dem Studium. Vor allem dem Tenor.

Meine Studienkollegen und gute Freunde, die mit mir gelernt haben und auch nach dem Studium noch wichtige Menschen in meinem Leben sind: Joscha, Mirko, Felix, Benni, Max/Max, Schorsch, Andrej, Thomas, Mahmut.

Meiner Familie, die immer da war, wenn ich mal eine Auszeit gebraucht habe. Ihr habt mir Mut gemacht und mich auf dem Boden der Tatsachen gehalten. Danke Mama und Papa, Kaddi, Chris, Anna, Thesi für 31 Jahre Lebenschoaching, Privatbankier, Taxiservice, Dating-Agentur, Sparring-Partner und alles andere.

Last but not least: Ein riesengroßes Dankeschön an meine Susi Sonnenschein, meine kleine Familie in München. Danke für deine Unterstützung im Großen und im Kleinen und für all die schönen Momente mit dir. Subbere Wühlung.